Mechanobiological optimisation of large bone defect scaffolds

vorgelegt von
Dipl.-Ing.
Camille Sylvie Perier-Metz
ORCID: 0000-0002-4189-1706

an der Fakultät V - Verkehrs- und Maschinensysteme
der Technischen Universität Berlin
zur Erlangung des akademischen Grades

Doktor der Ingenieurwissenschaften
- Dr.-Ing. -

genehmigte Dissertation

Berlin 2022

Zusammenfassung

Knochen hat die bemerkenswerte Fähigkeit, sich nach einer Verletzung ohne Narbenbildung zu regenerieren. Allerdings kann diese inhärente Fähigkeit in bestimmten kritischen Fällen beeinträchtigt werden, zum Beispiel im Fall von großen Knochendefekten, bei denen ein großes Knochenstück fehlt. Die derzeitige Standardbehandlung für solche Defekte beinhaltet den Einsatz von autologem Knochenmaterial, wobei Knochenmaterial des Patienten aus einer defektfernen Stelle entnommen und in den Defekt implementiert wird, um ihn mechanisch und biologisch zu unterstützen. Diese Behandlungsmethode hat jedoch mehrere wesentliche Nachteile wie beispielsweise den zusätzlich erforderlichen chirurgischen Eingriff, der mit Morbidität an der Entnahmestelle verbunden ist, und die begrenzte Verfügbarkeit des Knochenmaterials. Eine alternative Behandlungsstrategie besteht darin, 3D-gedruckte Knochengerüste zu benutzen.

Solche Implantate, bestehend aus Metall, Polymer oder Keramik, werden synthetisch vor dem chirurgischen Eingriff hergestellt und finden Anwendung in unterschiedlichen Defekten, um deren Regeneration zu unterstützen. Bislang bleibt unklar, wie genau solche Gerüste den Knochenregenerationsprozess beeinflussen, was deren alltägliche klinische Anwendung für die Behandlung von großen Knochendefekten unterbunden hat. Zur Bewertung des klinischen Potenzials eines Gerüstes wurde vor allem die Versuch-und-Irrtum-Methode herangezogen, welche langwierige, teure und mitunter ethisch fragwürdige Experimente erfordert.

Dieses wichtige klinische Problem galt als Ausgangspunkt dieses Projekts. Ziel der Doktorarbeit war es also, eine *in silico* Methode zu entwickeln, um Gerüste für die Regeneration großer Knochendefekte zu konzipieren, die den endogenen Knochenheilungsprozess optimal unterstützen. Dazu wurden spezifische Mechanismen der gerüstgestützten Regeneration großer Knochendefekte anhand eines prädiktiven Computermodells für Knochenregeneration untersucht. Anschließend wurde der Effekt individueller Gerüstparameter studiert. Hierbei wurde die Dynamik des Knochenregenerationsprozesses erforscht, indem Heilungsvorhersagen nach bestimmten Heilungszeitpunkten miteinander verglichen wurden. Letztens wurde ein Computer-Framework für die Optimierung der Knochengerüste mit dem Ziel entwickelt, das Volumen regenerierten Knochens zu maximieren.

Die *in silico* Untersuchung der gerüstgestützten Regeneration großer Knochendefekte baute auf einer gekoppelten Finite-Elemente-Analyse und agentenbasierte Modellierung auf, um verschiedene Experimente zu simulieren. Der Vergleich zwischen den *in silico* Vorhersagen und den experimentellen Ergebnissen lieferte mechanistische Einblicke in den Regenerationsprozess: (1) der Mangel an biologischer Stimulation in großen Knochendefekten, der durch den Einsatz

Zusammenfassung

von Gerüstmaterial oder Knochenmaterial kompensiert werden kann, und (2) der Einfluss der Gerüstflächen auf die Prozesse von Zellmigration und Gewebeanlagerung.

Unterschiedliche Gerüste wurden simuliert, indem die Porengröße, die Stützengröße oder die Materialeigenschaften verändert wurden. Generell zeigte sich, dass poröse steife Gerüste oder voluminösere weichere Gerüste die Knochenregeneration am vorteilhaftesten unterstützen. Allerdings hingen die optimalen Poren- oder Stützengrößen größtenteils von der zugrunde liegenden Gerüstarchitektur ab, was darauf hinweist, dass eine allgemeingültige Empfehlung nicht angewendet werden kann, um optimale Gerüste zu konzipieren.

Darüber hinaus zeigte die Modellierung von verschiedenen Zeitintervallen (initiale Mechanik und Simulation der Knochenregeneration) die Dynamik des Knochenregenerationsprozesses. Ergebnisse aus verschiedenen Zeitintervallen standen nämlich im Widerspruch zueinander: mehrere Gerüste schienen initial sehr vorteilhaft aber der Modellvorhersagen zufolge wurde die Knochenregeneration dann nicht gut unterstützt. Diese Feststellung bestätigte den Bedarf eines dynamischen Optimierungsprozesses, der auch den Regenerationsprozess berücksichtigen würde.

Letztens wurde ein Computer-Framework für die Optimierung von Knochengerüsten entwickelt. Als Ziel wurde die Maximierung des Volumens des regenerierten Knochens nach dem mechanobiologischen Knochenregenerationsmodell gesetzt. Gerüste wurden anhand einiger Variablen (etwa Porengröße oder Materialeigenschaften) parametrisiert. Eine Surrogat-Optimierungsvorgehensweise wurde wegen der rechenintensiven Regenerationssimulationen gewählt: ein vereinfachtes Input-Output-Verhältnis wurde von einer Gruppe von initialen Simulationsläufen abgeleitet und für den Optimierungsprozess benutzt, um zu viele rechenintensive Simulationsläufe zu vermeiden. Die Ergebnisse dieser Doktorarbeit beweisen das Anwendungspotenzial dieser Methode für ein vereinfachtes kubisches Gerüst und ein realistischeres zylindrisches Gerüst. Diese Ergebnisse zeigen, dass das initiale Design des Gerüsts und dessen Parametrierung bedacht ausgesucht werden sollten, um den Optimierungsausgang zu verbessern.

Zukünftige Forschungsarbeit sollte die Validierung des Computermodells für die gerüstgestützte Regeneration großer Knochendefekte fortsetzen. Insbesondere ist darauf zu achten, die rechnerische Effizienz dieser Modelle für deren Anwendung für Optimierungszwecke zu verbessern. Zusätzlich sollten realistischere, klinisch-basierte Gerüste für das Optimierungsverfahren mit komplementären Experimenten benutzt werden. Auf dieser Weise kann ein grundlegendes Verständnis für das Heilungspotenzial des Gerüstes geschaffen und ein fundiertes Design von experimentellen Gerüsten iterativ verbessert werden.

Abstract

Bone has the remarkable capability to regenerate without forming any scar tissue upon a given injury. However, this intrinsic healing capacity can be impaired in some critical cases, such as large bone defects where a large piece of bone is missing. The current gold standard treatment for such defects is autologous bone grafting, where bone material is taken from another location in the patient and put into the defect to support it mechanically and biologically. Nevertheless, this treatment has several drawbacks, in particular the need for an additional surgery associated with donor site morbidities and a limited availability of bone material. An alternative treatment strategy is the use of 3D-printed bone scaffolds.

Such implants are produced synthetically before the chirurgical intervention, can be made of metal, polymer or ceramic, and implanted into various defects to support their regeneration. However, how such scaffolds interact with the bone regeneration process has remained poorly understood so far, preventing scaffolds to become clinical routine practice in large bone defect treatment. In addition, scaffold design has mainly relied on trial-and-error approaches, requiring long, costly and ethically questionable experiments to assess the scaffold healing potential.

This critical clinical issue was the starting point of this project. The aim of the thesis was therefore to propose an *in silico* methodology to design scaffolds for large bone defect regeneration that would be optimised for their ability to support the endogenous bone healing process. To do so, specific mechanisms of scaffold-supported large bone defect regeneration were investigated by means of a predictive computer model for bone regeneration. Next, the effect of individual scaffold design parameters were studied. In addition, the dynamics of the bone healing process was investigated by comparing healing outcome predictions at different healing time points. Lastly, a computational framework for bone scaffold optimisation was developed with the objective of maximising the amount of regenerated bone.

The *in silico* investigation of scaffold-supported large bone defect regeneration used a coupled finite element analysis and agent-based model to simulate various experimental studies. The comparison between *in silico* predictions and experimental results revealed specific features of the regeneration process: (1) the lack of biological stimulation in large bone defects, that can be compensated by specific scaffold material or the addition of bone graft and (2) guidance provided by the scaffold surfaces on the cellular migration and tissue deposition processes.

Specific scaffold designs were varied by changing the pore size, strut size or material properties. Overall, porous stiff scaffolds or more bulky softer scaffolds were found to be most beneficial for bone regeneration. However, precise pore or strut size recommendations

Abstract

depended largely on the underlying scaffold architecture, suggesting that a "one-fits-them-all" approach cannot be used to design optimal scaffolds.

In addition, the modelling of different time horizons (initial mechanics and bone regeneration simulation) highlighted the dynamics of the bone regeneration process. Conclusions based on different time horizons contradicted each other: several scaffold designs seemed very favourable initially but were actually not predicted to support bone regeneration well. These observations emphasised the need for a dynamic optimisation process that would take the regeneration process into account.

Lastly, a computational framework for bone scaffold design optimisation was developed. Its objective was defined as to maximise regenerated bone volume according to the mechanobiological bone regeneration model; scaffold designs were parametrised with a few variables (e.g. pore sizes or material properties). A surrogate optimisation approach was chosen to deal with the computationally demanding regeneration simulations: a simplified input-output relationship was derived from a set of initial simulations and used for the optimisation process to avoid too many demanding simulation runs. The results presented in the thesis proved the feasibility of the approach on a simplified cubic scaffold and a more realistic cylindrical scaffold. These results suggested that the initial design and its parametrisation should be carefully chosen to improve the optimisation outcome.

Future work should further validate the computer model for scaffold-supported bone regeneration. A particular emphasis should be put on improving the computational efficiency of such models for their use in optimisation purposes. Next, more realistic, clinically-based scaffold designs should be employed in the optimisation framework, in combination with experiments. In that way, knowledge on scaffold healing potential and informed scaffold design for experiments could be improved iteratively.

Résumé

Les os ont la capacité remarquable de pouvoir se régénérer sans former de cicatrice après une lésion. Cependant, cette capacité de guérison intrinsèque peut être dégradée dans certains cas critiques, comme les grands défauts osseux, des lésions où un grand morceau d'os manque. Le traitement de référence actuel pour ces défauts est l'usage de greffe osseuse autologue : de l'os est prélevé d'un autre emplacement dans le patient et est inséré dans le défaut pour lui conférer un soutien mécanique et biologique. Néanmoins, ce traitement a de nombreux inconvénients, en particulier la nécessité d'une chirurgie supplémentaire, associée à des morbidités du site donneur, et une quantité limitée de tissu osseux disponible. Une stratégie thérapeutique alternative consiste à utiliser des implants osseux obtenus par impression 3D.

Ces implants, qui peuvent être faits de métal, polymère ou céramique, sont produits de façon synthétique avant l'intervention chirurgicale et sont implantés dans un défaut spécifique pour en soutenir la régénération. Cependant, on ne sait pas encore comment ces implants interagissent avec le processus de régénération osseuse, empêchant les implants de devenir une pratique clinique routinière pour le traitement des grands défauts osseux. De plus, la conception des implants découle essentiellement d'approches par tâtonnements qui nécessitent des expériences longues, coûteuses et de justification éthique discutable pour évaluer le potentiel d'un implant à traiter de grands défauts osseux.

Ce problème clinique important a servi de point de départ à ce projet. L'objectif de la thèse était donc de proposer une méthodologie *in silico* pour concevoir des implants pour la régénération de grands défauts osseux qui seraient optimisés pour leur capacité à soutenir le processus de guérison osseuse endogène. Pour ce faire, les mécanismes spécifiques de la régénération de grands défauts osseux en présence d'implants ont été examinés à l'aide d'un modèle computationnel prédictif pour la régénération osseuse. Ensuite, l'effet de paramètres individuels décrivant l'implant a été étudié. De plus, la dynamique du processus de guérison osseuse a été analysée en comparant les prédictions de guérison à différents moments. Enfin, un modèle computationnel d'optimisation d'implant osseux a été développé, avec l'objectif de maximiser la quantité d'os régénéré.

L'étude *in silico* de la régénération de grands défauts osseux en présence d'implants utilise une analyse par éléments finis couplée à un modèle multi-agents pour simuler différentes études expérimentales. La comparaison entre les prédictions *in silico* et les résultats expérimentaux a révélé certaines caractéristiques spécifiques du processus de régénération : (1) l'absence de stimulation biologique dans les grands défauts osseux, qui peut être compensée par le matériau de l'implant ou par l'addition de greffe osseuse et (2) le guidage assuré par les surfaces de l'implant pour les processus de migration cellulaire et de dépôt de nouveaux tissus.

Résumé

Différents implants ont été simulés en modifiant la taille des pores, la taille des traverses ou les propriétés du matériau utilisé. Globalement, les implants rigides très poreux ou les implants plus souples et plus volumineux se sont révélés être les plus bénéfiques pour la régénération osseuse. Cependant, les recommandations précises de tailles de pores ou de traverses dépendent largement de l'architecture sous-jacente de l'implant, suggérant qu'une approche standardisée ne peut être utilisée pour concevoir des implants optimaux.

En outre, la modélisation de différents horizons de temps (mécanique initiale et simulation de la régénération osseuse) a mis en lumière la dynamique du processus de régénération osseuse. Les conclusions basées sur différents horizons de temps se contredisent : de nombreuses géométries d'implants semblaient très favorables initialement mais ne supportaient pas bien la régénération osseuse d'après les prédictions. Ces observations soulignent le besoin de faire appel à un processus d'optimisation dynamique qui prend le processus de régénération en compte.

En dernier lieu, un modèle computationnel pour l'optimisation d'implants osseux a été développé. Son objectif a été défini comme la maximisation du volume d'os régénéré prédit par le modèle mécanobiologique de régénération osseuse. Les implants ont été paramétrés avec quelques variables (par exemple la taille des pores, les propriétés mécaniques du matériau). Une approche d'optimisation par modèle de substitution a été choisie à cause des simulations de régénération très exigeantes du point de vue computationnel : une relation simplifiée d'entrée-sortie a été dérivée d'un ensemble de simulations initiales et utilisée pour le processus d'optimisation pour éviter un trop grand nombre de simulations coûteuses. Les résultats présentées dans cette thèse prouvent la faisabilité de l'approche sur un implant cubique simplifié et un implant cylindrique plus réaliste. Ces résultats suggèrent que l'architecture initiale et sa paramétrisation doivent être choisies avec soin pour améliorer le résultat de l'optimisation.

Des travaux de recherche futurs devraient valider davantage le modèle computationnel de régénération osseuse en présence d'un implant. En particulier, ils devraient se concentrer sur l'amélioration de l'efficacité computationnelle de ces modèles pour leur usage à des fins d'optimisation. Ensuite, des implants plus réalistes et basés sur des besoins cliniques devraient être utilisés dans le modèle d'optimisation, en combinaison avec des expériences. De cette façon, les connaissances sur le potentiel thérapeutique des implants et la conception mieux informée d'implants expérimentaux pourraient être améliorées de façon itérative.

In nature, there is no separation between design, engineering, and fabrication;
the bone does it all.

Neri Oxman, designer

Acknowledgements

My main and deepest gratitude goes to Prof. Sara Checa who constantly guided me throughout my PhD journey, providing suggestions wherever I was stuck and spending hours of reviewing my writings.

I am very grateful to Prof. Georg Duda, Prof. Manfred Zehn and Prof. Laurent Corté for their guidance during the PhD and in particular during my mentoring meetings. Thanks to Prof. Rachele Allena as well with whom an interesting collaboration led to additional understandings of the topic.

My gratitude also goes to the Corps des Mines and MINES ParisTech – PSL Research University for having given me the opportunity to do this PhD in the first place and funded my 3 years of work; and to the Julius Wolff Institute for having hosted me during that time.

My work would not have been possible without the dedication of Thomas Sips, the JWI IT manager, who was always there for all IT issues encountered during that journey (and there were many!); and the JWI administrative team who were very helpful with all administrative questions.

I would like to thank all my colleagues from the Computational Mechanobiology group (Edoardo, Martina, Vincenzo, Clemens, Ehsan, Bahar, Özgür, Chiara, Mahdi...) for their technical help, scientific discussions and great times out of the office; my former office mates Aline and Janina and other colleagues from the JWI and the BSRT for nice scientific and non-scientific discussions and a good experience in organising the BSRT symposium 2019. A special thank goes to Aline and Kymbat for their great improvements to the German abstract!

I acknowledge Holger Nahrstaedt for the Latex template used for this thesis (`https://github.com/holgern/TUB_PhDThesisTemplate`).

Lastly, I would like to thank my parents and brothers who largely made me who I am over the years and gave me the interest to science; my husband who supported me throughout the PhD, mostly to raise my motivation whenever low but also technically for all my coding issues; and my child who taught me how to deal with prioritisation...

Table of Contents

List of Figures

LIST OF FIGURES

List of Tables

Abbreviations

ABG autologous bone graft. 1

ABM agent-based model. 5

BMP bone morphogenetic protein. 7

BW body weight. 20

DOE design of experiments. 30

ECM extracellular matrix. 18

FE finite element. 13

FEA finite element analysis. 5

GA genetic algorithm. 40

LHS Latin hypercube sampling. 34

MARS multivariate adaptive regression splines. 39

MBBR mechanobiological bone regeneration. 31

MSC mesenchymal stromal cell. 2

PCL polycaprolactone. 6

PSO particle swarm optimisation. 40

RMSE root mean square error. 113

ROI region of interest. 26

SA/V surface-area-to-volume ratio. 30

TCP tricalcium phosphate. 6

μCT micro-computed tomography. 14

1

Introduction

1.1 Clinical motivation

Bone is a key organ in the human body, having a mechanical role as support structure and protection for internal organs and a physiological role with blood cell production in the bone marrow and calcium homeostasis control. It has, under normal circumstances, the remarkable ability to regenerate and come back to its original shape after a given trauma (e.g. a fracture). However, this healing capacity can be impaired, for instance when a too large piece of bone is missing (Figure 1.1). This situation is known as a large bone defect and the resulting non-healing (for at least 9 months) is called a non-union [1]. Non-unions are estimated to occur in 5-10% of all fractures in the United States of America [2].

The current gold standard treatment for large bone defects is the use of autologous bone graft (ABG) [3, 4]: bone is taken from another location in the patient (the iliac crest, for long bone applications) and ground and the resulting powder is put into the defect. This method, although very effective, is associated with several limitations such as donor site co-morbidities, the need for a second surgery and limited bone availability [3, 5, 6]. Therefore, there is a clinical need for alternative treatment strategies; a promising one consists in using synthetic, mechanically optimised scaffolds that can serve as a support structure in the defect with the aim of enhancing the endogenous healing process [7–15].

Different scaffolds have yielded various outcome in pre-clinical studies [9, 12–18], where bone regeneration has been shown to be influenced by the scaffold geometry (pore size, porosity, architecture...) and material properties. However, there is still a lack of understanding how the multiple scaffold design parameters interact with the regeneration process to ensure a good healing outcome (Figure 1.1). Only a few scaffold design parameters have been individually studied, such as pore size [19–21] or material choice [22–25]. Thus, bone scaffold design and development rely mostly on trial-and-error approaches, thereby slowing the development process and requiring more ethically questionable animal studies.
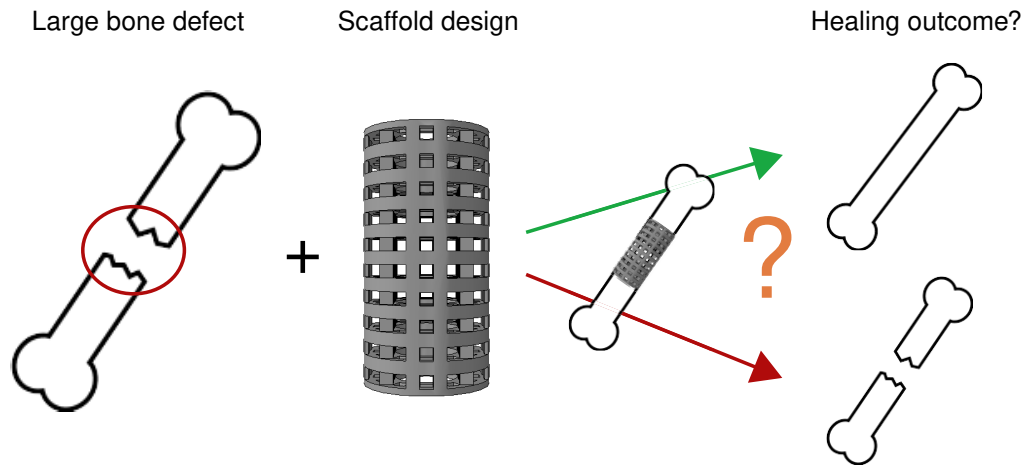
Figure 1.1 – **Scaffold-treated large bone defect outcome**: healing outcome is unknown so far and depends on the scaffold architecture (pore size, porosity, pore or strut shape...) and material properties.

1.2 Biological and mechanobiological background

1.2.1 Bone healing

Bone is one of the few organs in the human body that has a healing capacity leading to complete recovery of its original shape, without forming any scar tissue. The bone healing process is defined as primary when intact bone pieces are aligned and pressed against each other, without any gap; or secondary if there is a gap, then involving a callus formation [26].

The secondary bone healing process can be divided into the four main phases depicted in Figure 1.2: inflammatory, soft callus, hard callus and remodelling phases [26–28]. First, inflammatory cells are recruited to the defect and produce inflammatory signals that are crucial for the subsequent bone healing process; a haematoma can be observed. After ca. seven days, mesenchymal stromal cells (MSCs) are recruited to the healing region and cartilaginous differentiation leads to the formation of a cartilaginous and periosteal bony callus (soft callus phase). This process is known as endochondral ossification (cartilage is formed before bone), while some direct intramembranous ossification (direct bone deposition) can be seen adjacent to the distal and proximal ends. The fracture site is further re-vascularised and new blood vessels start sprouting. The hard callus phase describes the mineralisation and resorption of the cartilaginous callus with the formation of woven bone (randomly arranged bone). Lastly, the hard callus is resorbed, woven bone is remodelled into cortical bone (showing a much higher degree of organisation) and the bone comes back to its original shape. This last phase is a slow process, taking months to years to be completed.

1.2.2 Influence of mechanics on bone healing

Bone is a highly mechanosensitive tissue, as was already described in 1892 by the anatomist and surgeon Julius Wolff in his Law of Bone Remodelling (Gesetz der Transformation der Knochen) [29]: a healthy bone continuously adapts to the loading it experiences by forming
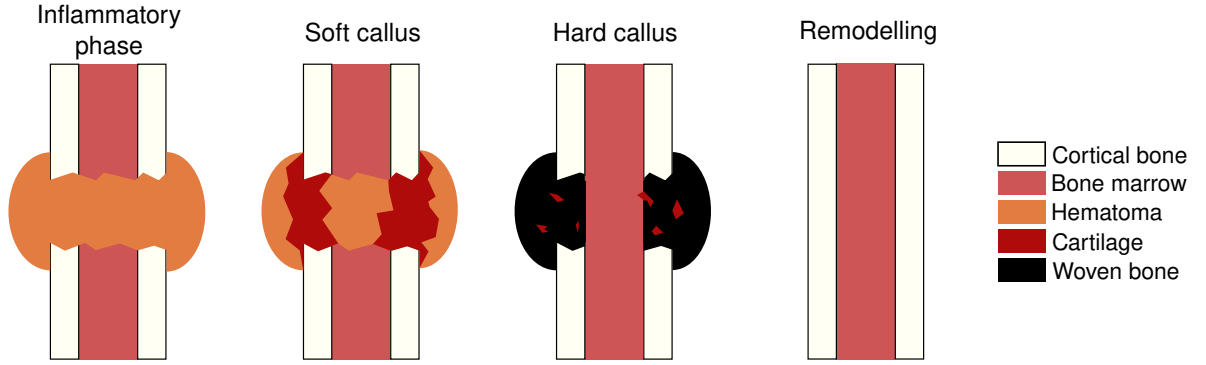
Figure 1.2 – Bone healing phases – adapted from [26]

more bone when and where the loading is increased and resorbing bone when and where it is reduced. This phenomenological law holds true for bone healing situations, where several coupled *in vivo* and *in silico* studies revealed a correlation between the formation of specific tissue types with the computed local levels of stress, strain and/or relative fluid velocity [30–33], following so-called mechanoregulation theories (Figure 1.3). Briefly, higher stimulus values (e.g. the minimal principal strain absolute value or the octahedral shear strain) were found to correlate with fibrous tissue formation, intermediate ones with cartilage formation and lower values with bone formation. Very low stimulation was correlated with bone resorption.
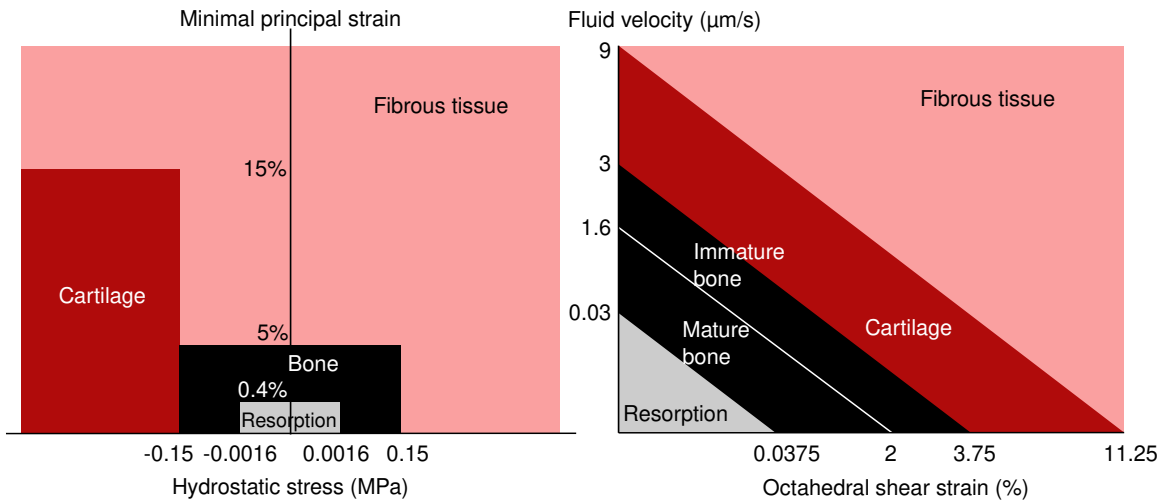
Figure 1.3 – Mechanoregulation theories – developed by Claes & Heigele [32] on the left and by Lacroix & Prendergast [34] on the right. The hydrostatic stress is defined by $-\frac{1}{3}(SP_1 + SP_2 + SP_3)$ with SP_i the principal stress component i; and the octahedral shear strain by $\frac{2}{3}\sqrt{(EP_1 - EP_2)^2 + (EP_2 - EP_3)^2 + (EP_1 - EP_3)^2}$ with EP_i the principal strain component i

1.2.3 Large bone defects

Large bone defects, also known as critical-sized bone defects, do not have a unique definition. However, in a long bone, a defect where twice the dimension of the bone diameter is missing will generally be considered a large bone defect and result in a non-union [6]. Most large bone defects are seen in the lower limb long bones, i.e. tibia and femur (accounting for 68% and 22% of all fractures with bone loss, respectively, in Edinburgh [35]). Such defects are associated

with mobility impairment and infections risks for the patient, and high healthcare and society costs due to repeated surgical interventions and a limited ability to work.

Current most common and successful treatment approaches include [1, 6, 36]:

Autologous bone grafting Bone is taken from another location (often the iliac crest) in the patient to be inserted into the defect.

Masquelet or induced membrane technique A few weeks prior to the autologous bone grafting, a cement spacer is put into the defect to ensure the formation of a biological membrane. The cement spacer is then carefully removed and the ABG is placed instead.

Distraction osteogenesis Another fracture is surgically created and the bone ends are moved step-by-step to ensure a continuous healing until both gaps are healed.

Although highly effective (more than 90% success for fractures in the studies reviewed by Bezstaros and colleagues [36]), those approaches have limitations and associated risks: additional surgeries, limited available amount of bone, infection risks, donor site co-morbidities, need for high patient compliance [6].

More recent and innovative therapeutic approaches include the use of cells (MSCs) or proteins (specific bone growth factors) to enhance bone regeneration [1, 6], low-intensity pulsed ultrasound to stimulate the endogenous regeneration process [1], or the use of structured or unstructured synthetic implants [9, 13, 37]. In addition, the use of cells and proteins have shown promising results in some pre-clinical and clinical studies [1, 9], but their effect on the healing cascade is highly complex to control, what has often resulted in no positive effect [9] or even in adverse effects [1, 38]. The use of a single structure alone has therefore attracted a lot of attention in the last years, since they are expected to provide a more controlled environment to foster the regeneration process [9, 37]. The remaining of this work will therefore focus on structured implants and refer to them as "scaffolds".

1.2.4 Bone scaffolds

Bone scaffolds are structured implants that can be made from different materials (e.g. metals, polymers, ceramics) and are implanted into the bone defect to enhance its regeneration capacity, usually in combination with a fixation plate to support the mechanical loading. Different scaffold types have been tested in pre-clinical studies, ranging from e.g. titanium honeycomb-like structures [13] to composite (polymer-ceramic) strut-based designs [9].

Long bone scaffolds should have the following properties to best support the endogenous regeneration process [3, 39, 40]:

Biocompatibility The material used to fabricate the scaffold should not endanger cell viability and proper functioning.

Biodegradability Optionally, the scaffold material can be biodegradable to disappear over time, thus not remaining in the defect region permanently. In that case, the degradation products should not be toxic for the body.

Osteoconductivity The scaffold is supporting the in-growth of new bone.

Osteoinductivity The addition of biological substances such as growth factors can foster MSC differentiation into bone cells.

Angiogenic potential The scaffold architecture should foster the defect re-vascularisation, a pre-requisite for adequate bone regeneration.

When designing a scaffold, different parameters have to be considered and optimised: scaffold material [22]; porosity, pore size and pore inter-connectivity [20]; scaffold geometry and architecture; and the scaffold interaction with the host tissue via mechanotransduction mechanisms [41]. In particular, O'Keefe and Mao named four critical consideration points in scaffold design: form, function (mechanical properties), fixation (integration with remaining bone) and formation (osteoconductive properties of the scaffold) [41]. Experimentally, it has also been observed that scaffolds guide the regeneration process [13, 42, 43] by acting as a template for migration and bone deposition processes [42, 44–46]. However, how exactly this guidance is happening remains to be elucidated.

1.3 State of the art

1.3.1 *In silico* models for scaffold-supported large bone defect regeneration

1.3.1.1 *In silico* models for fracture healing

Since first studies revealed the impact of mechanics on bone healing and remodelling [29–32], several *in silico* models of fracture healing mechanoregulation have been developed, as compared by Isaksson *et al.* [47] or reviewed by Borgiani *et al.* [48]; an example of the prediction made for the bone healing process in a sheep osteotomy model is given in Figure 1.4 [33]. These models have used multi-scale approaches, with mechanics being studied with a finite element analysis (FEA) at the macroscopic scale, and cellular processes or tissue deposition implemented at the microscopic scale. These processes have been described in discrete models such as agent-based models (ABMs) accounting for cellular behaviours [33, 49]; or in continuous diffusion-reaction equations describing tissue deposition and resorption [50, 51]. In both cases, cells or tissues to be favoured have been determined by a mechanoregulation theory linking the tissue type (granulation tissue, fibrous tissue, cartilage, bone) or cell phenotype (MSCs, fibroblasts, chondrocytes, osteoblasts) to a mechanical stimulus computed in the FEA. The two mechanoregulation theories used in this PhD thesis have been developed by Lacroix and Prendergast [34] based on a poro-elastic analysis of the tissues; and by Claes and Heigele [32], based on a purely elastic description of the tissues (Figure 1.3).

In addition to this mechanobiological approach, some computer models for bone regeneration have included chemical or biological gradients to describe e.g. the effect of growth factors [52–55]. Additional processes such as vascularisation have also been described [56–58], as re-vascularisation of large bone defects is known to be a limiting factor of scaffold-based therapeutic approaches [20, 59–61].

Lastly, *in silico* bone remodelling models have been used to reveal longer-term effects related to bone healing. This has been done to study e.g. hip implant integration [62–65] and femur fracture treatment fixation [64, 65].
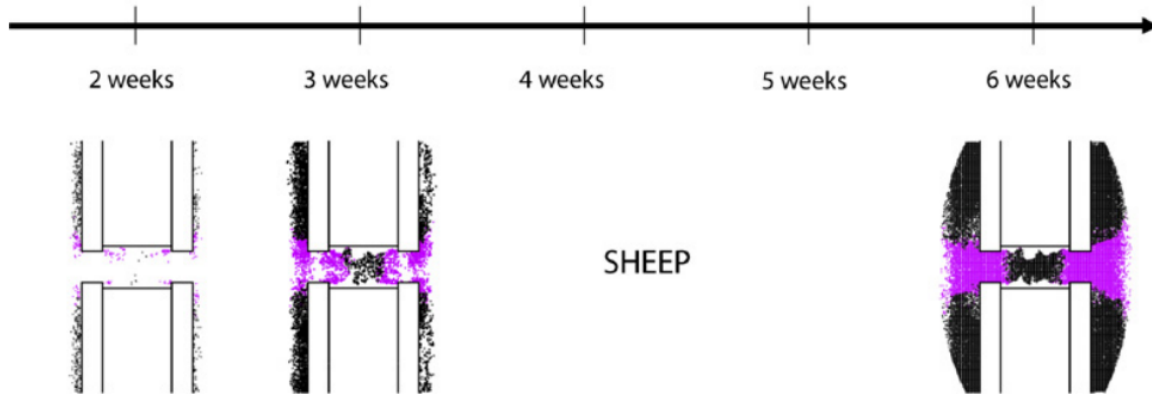
Figure 1.4 – **Bone fracture healing simulation in sheep**: bone is depicted in black and fibrocartilage in purple – reproduced with permission from [33], Copyright ©2011 Elsevier Ltd.

1.3.1.2 *In silico* models for scaffold-supported bone regeneration

Fracture healing models have already been used to investigate scaffold-supported bone regeneration in several studies [51, 52, 66–68]. In some cases, the effect of scaffold design parameters on the local mechanics and resulting bone regeneration extent has been evaluated for optimisation purposes [69, 70]. However, most of these models are direct applications of the models used for successful bone healing and do not take into account the interaction of the scaffold itself with the regeneration process. More importantly, most of those models have not been validated against experimental data to ensure their validity in the context of large bone defects and scaffold presence.

In fact, only a few computer models for bone healing within scaffolds have been developed and validated with experimental data. For instance, Schmitt *et al.* developed a 2D diffusion-based model with mechanoregulation of bone formation within a titanium scaffold used in a segmental mandibular defect. They were able to show a good agreement with the experimental data by assuming that the differentiation of MSCs towards osteoblasts was driven by the local principal stresses [71]; however, they did not include the actual scaffold geometry in their model nor did they study the actual cell invasion into the defect. A study by Paris and colleagues focused on the effect of scaffold curvature on collagen and mineralised tissue patterning in a composite (polycaprolactone (PCL)-tricalcium phosphate (TCP)) scaffold [72]; however, their study did not include any mechanical or material-specific effects on the regeneration process, so that a scaffold with the same structure but different material properties would be predicted to yield the same outcome. Cheong *et al.* simulated bone in-growth into femoral condyle scaffolds by assuming that new bone could be deposited only onto existing bone (property coined as "osteoconnectivity") or the coated scaffold surface, depending on a strain energy density-based stimulus [73]. Their results compared relatively well with one experimental time point, but they did not consider the contribution of other tissue types, and their model was applied to femoral condyles and not to long bone segmental defects (Figure 1.5).

In addition to the scaffold presence, the large bone defect context is in itself different from uneventful fracture healing. It was for instance shown that assuming the same biological activity in a large bone defect as in a small fracture did not reproduce experimental observations [54]. The implementation of a latency period after which cells would have a reduced potential for
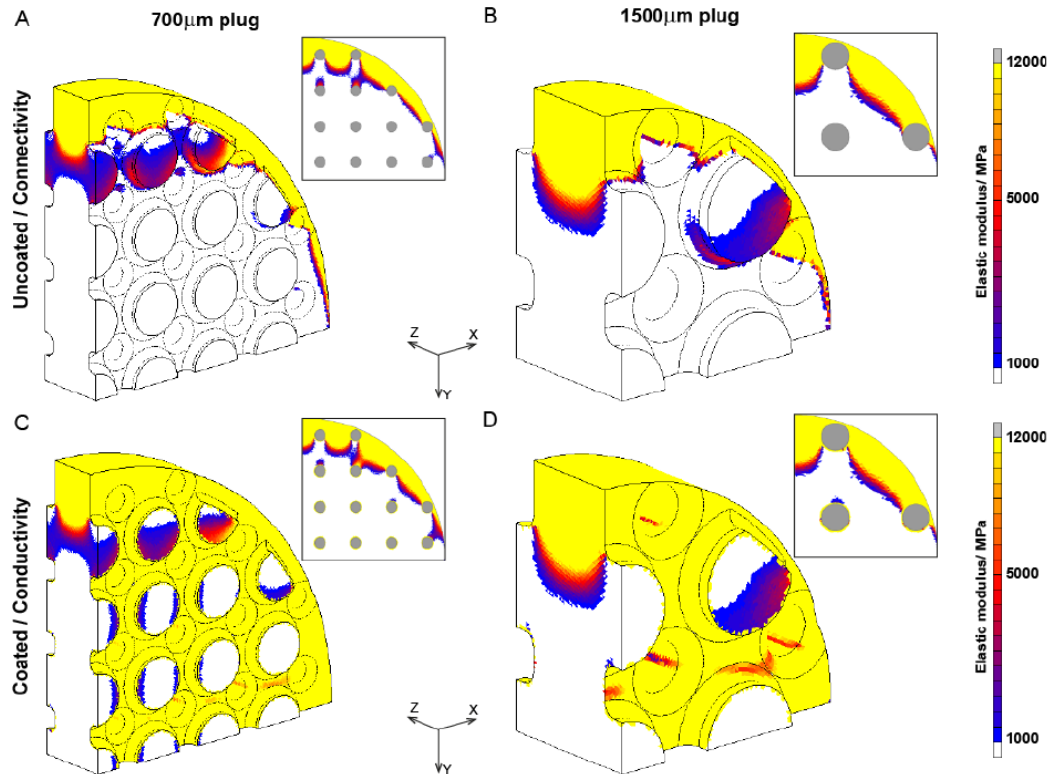
Figure 1.5 – Bone regeneration simulation in a femoral condyle scaffold: regenerated tissue Young's modulus distribution, with high values representing high bone densities – reproduced with permission from [73], Copyright ©2018 Elsevier Ltd.

migration, proliferation and/or tissue deposition accounted for the lack of biological stimulation in large gaps and predicted the experimentally observed non-union and bone marrow capping [1, 74].

In some cases, bone scaffolds can be used in combination with biological stimulation (graft [13, 75], proteins or cells [9, 76]). To our knowledge, there was only one study modelling the effect of graft in large bone defects, where an enhanced osteoconduction was simulated by a higher cell adhesion efficiency in a rabbit femur condyle defect supported by a scaffold [51]. Their regenerated bone volume predictions were in good agreement with the experimental data; however, they did not include the actual scaffold architecture but averaged its mechanical contribution using homogenisation theory. Regarding the effect of proteins (e.g. bone morphogenetic proteins (BMPs)), Zhang and colleagues included their chemical effect on cell differentiation and migration and applied their model to scaffold-supported bone regeneration. They validated the predicted MSC activity rates in presence of BMP2, but not the predicted regenerated bone volumes [77]. Further studies investigated the effect of different initial cell seeding strategies in bone scaffolds [67, 78]; however, these *in silico* studies were not validated against experimental data.

1.3.2   Computer-aided scaffold design and optimisation

Computer-aided design and optimisation has been widely used for product development in many engineering fields (e.g. car or aircraft development) since the 1990s, taking advantage

of mathematical algorithms and computer power that allowed for optimal design search in a reasonable amount of time [79]. The use of computer tools in bone scaffold design is more recent but shows a growing research effort [80–83]. In 2019, we reviewed 28 studies presenting computer-based bone scaffold optimisation approaches [84].

In general, a design optimisation framework aims at minimising or maximising a given design objective under a set of constraints, the design update being guided by a mathematical algorithm. Most of the optimisation performed on scaffold design so far has been structural optimisation, i.e. scaffold architecture optimisation, where two main principles have been followed: topology or shape optimisation (Figure 1.6). Topology optimisation is a technique to optimise material distribution in a given design volume to maximise a quantity of interest (typically the stiffness) while minimising the mass. Material is gradually removed from a bulk volume where it is least needed (e.g. lower stress values) [85]. Holes can be added to the structure, hence changing the resulting topology. On the contrary, shape optimisation starts from a predefined topology, where boundaries are moved to achieve the objective (e.g. maximum stiffness) under given constraints (e.g. on mass or porosity). Parametric optimisation can be seen as one type of shape optimisation where the initial design is parameterised by variables such as strut widths or pore sizes which are varied in the optimisation process. Parametric optimisation also allows further variable definition such as material properties.
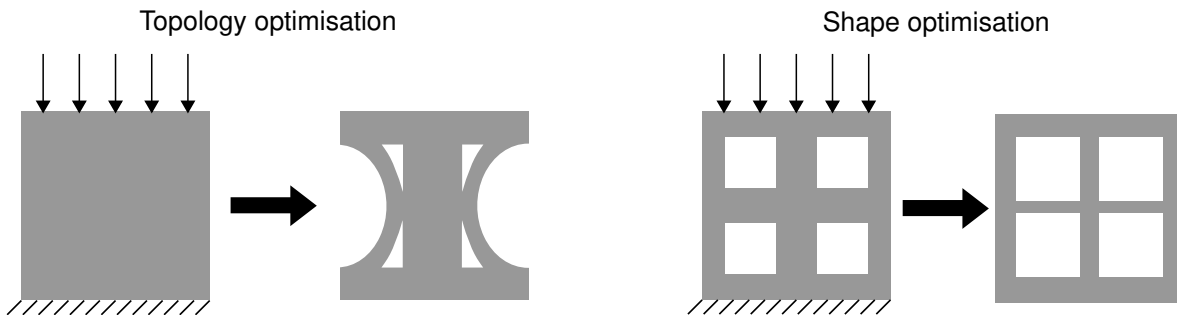
Figure 1.6 – Topology and shape optimisation principles

An optimisation framework follows the steps depicted in Figure 1.7: the problem is defined, namely the objective function and the constraints restricting the design space. An initial geometry is given as an input for which the objective value is computed; this geometry is then updated using mathematical algorithms. This process is repeated as long as convergence is not achieved – or other stopping criteria such as a maximum number of iterations.

There are two general approaches in bone scaffold design optimisation [84]: (1) **mechanics-based optimisation**, where the objective is based on scaffold mechanical properties and (2) **mechanobiology-based optimisation** that implements the interaction between mechanics and the biology of tissue regeneration, with the objective linked to bone regeneration predictions. The latter approach typically makes use of mechanoregulation theories to assess the mechanobiological potential of a given scaffold.
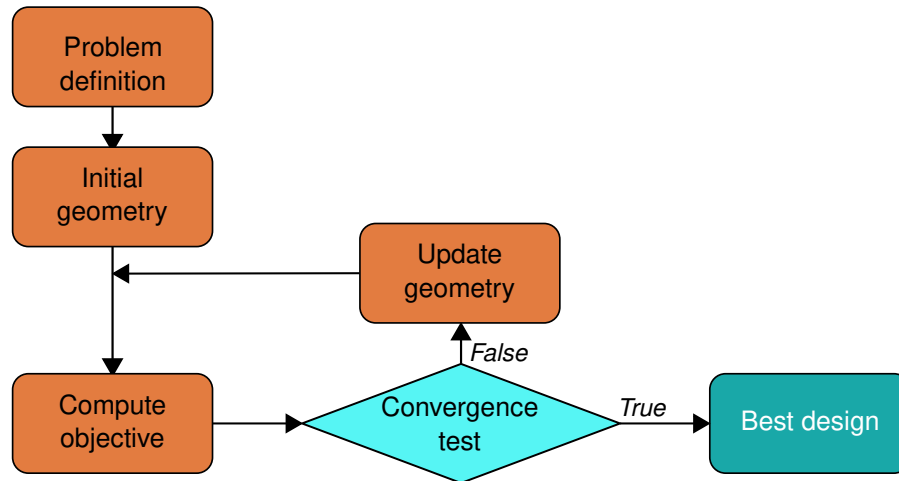
Figure 1.7 – **Optimisation framework example**

1.3.2.1 Mechanics-based scaffold optimisation

So far, mechanics-based bone scaffold optimisation has been mostly performed, since methods similar to other engineering fields can be applied. Objectives have been set to maximise compressive modulus [86] or stiffness [87–90] or equivalently to minimise compliance [91, 92] or strain energy [93]. These objectives have been coupled to constraints on a maximum scaffold volume or mass or a minimum porosity. In addition, in most cases only a unit cell has been optimised, assuming a periodic design where this cell would be repeated to fill a defect [87, 90, 92, 93]. These studies aimed at ensuring a proper load resistance of the implanted scaffold (under physiological loading conditions) with as little scaffold material as possible.

However, such mechanical objective favours rather bulky designs where pore interconnectivity and especially blood and nutrient supply can be impaired. For that reason, some studies focused on permeability [94] or performed multi-objective optimisation involving stiffness or bulk modulus on the one hand and permeability or diffusivity on the other [83, 95–98]. Such multi-objective optimisation processes lead to Pareto fronts, namely the set of geometries achieving the best global objective value with a different repartition between each individual objective; a compromise needs then to be made between e.g. stiffness and permeability.

Lastly, there have been a few studies that did not aim at maximising or minimising given mechanical properties but at mimicking the replaced tissue properties. Thus, the objective was defined as to come as close as possible to a given stiffness [80, 81, 99, 100], both stiffness and diffusivity [101, 102] or tissue strains [103]. Although targeting the bone tissue mechanical properties does not ensure the most appropriate environment for endogenous tissue regeneration, these examples departed from a purely mechanical approach by including knowledge on the tissue mechanical properties.

1.3.2.2 Mechanobiology-based scaffold optimisation

There were only a few examples of mechanobiological scaffold optimisation thus far, coming mainly from Boccaccio's team [70, 82, 104, 105], where the objective was set to maximise the

bone-favouring mechanical stimulus right after scaffold implantation for a variety of scaffold designs, relying on Lacroix and Prendergast's mechanoregulation theory [50]. Similar work was performed in the field of cartilage regeneration to optimise scaffold mechanical properties [106, 107]. However, these attempts did not include the actual, highly dynamic bone regeneration process, where a scaffold achieving best regeneration results right after implantation might not be the one yielding actual best bone regeneration at the end of the healing process (Figure 1.8). Indeed, Bashkuev *et al.* showed, on the example of a spine fusion cage device, that the time-point taken into account for the optimisation is critical: in a first step, they optimised the device material properties to obtain maximal predicted bone stimulus right after surgery; in a second step, they optimised the material properties throughout the regeneration process to ensure maximal bone formation. They obtained different optimal material properties, with the dynamic optimisation leading to material properties changing over time (that could be the consequence of a material degradation) [69].
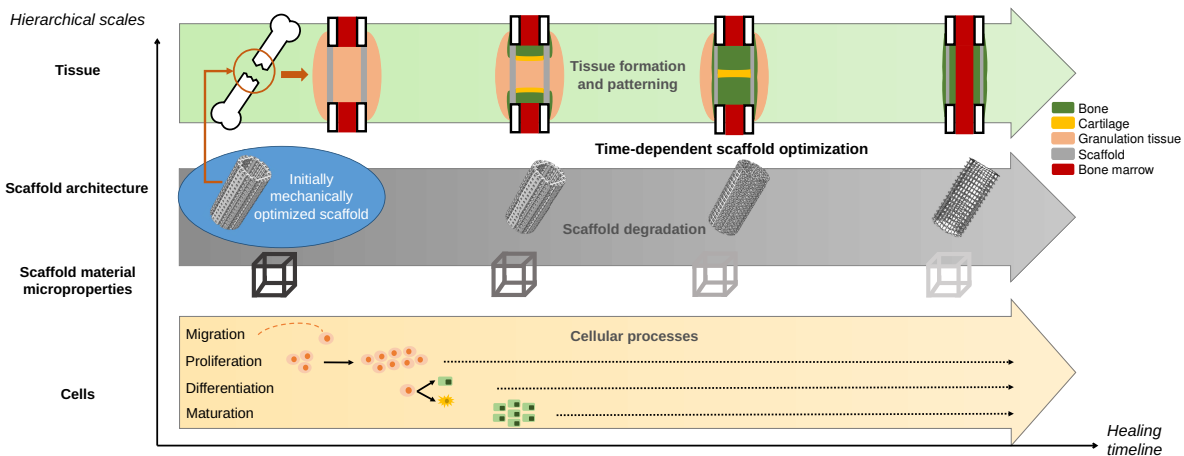
Figure 1.8 – **Scaffold-tissue interactions at multiple length and time scales during the bone healing process**; first published in [84]

Byrne and colleagues performed a parametric study taking the full regeneration process into account and investigated the influence of some of the scaffold design parameters (material properties and dissolution rate, porosity) [66]. They were able to predict strong effects of scaffold porosity on the regeneration outcome; however, their regeneration model was not validated in the context of scaffold-supported bone healing. In addition, their study was limited to a few specific parameter values, thus preventing from performing a true optimisation. Sanz-Herrera and colleagues also performed a parametric study of scaffold design parameters on healing outcome [78]. Using a computer model to predict bone regeneration in a scaffold, they investigated the influence of porosity, pore size, bulk biomaterial stiffness, resorption kinetics and the effect of scaffold pre-seeding with cells. They also showed strong effects of the investigated parameters; however, they did not perform a design optimisation and the effect of the different scaffold design parameters was evaluated individually (by changing one parameter at a time).

Only very few examples of time-dependent scaffold optimisation were performed in the bone regeneration field so far. Poh and colleagues optimised scaffold porosity distribution to best foster bone regeneration [108]; however, their framework was limited to 1D and did thus not

describe the scaffold micro-structure. Wu and colleagues performed a topology optimisation for bone scaffold design, both for a large, segmental defect in 2D and for a smaller defect in 3D; they used a bone remodelling algorithm to ensure the scaffold would not lead to stress shielding but on the contrary enhance bone regeneration in the defect [109]. However, their large defect scaffold optimisation study was restricted to 2D and their remodelling algorithm has not been assessed for its predictive capability of scaffold-supported bone regeneration.

Thus, there is no example so far of a 3D time-dependent mechanobiological optimisation of large bone defect scaffolds that would include the interaction between mechanical signals and biological processes and their evolution over time, as the defect gets filled with regenerated tissue.

1.4 Thesis objectives and hypotheses

The main goal of this PhD thesis was to develop an *in silico* framework for large bone defect scaffold design optimisation based on the *in silico* prediction of the scaffold-supported bone regeneration process.

This goal was subdivided into the following objectives:

1. To investigate the mechanobiological regulation of scaffold-supported bone regeneration and in particular the interaction between scaffold design and the bone regeneration process. To achieve this, an *in silico* model of bone regeneration within scaffolds was developed and validated against different experimental set-ups.

2. To investigate the effect of specific scaffold properties on scaffold-supported bone regeneration, such as scaffold surface-area-to-volume ratio, pore size or material properties.

3. To develop a mechanobiological bone scaffold design optimisation framework with the objective of maximising the predicted bone regeneration outcome in various defect configurations.

Key hypotheses guided this work:

1. Scaffold-supported large bone defect regeneration follows specific rules compared to fracture healing, related to the size of the defect (too large to heal spontaneously), the presence of the scaffold and its surfaces acting as templates for the regeneration process, and – potentially – the presence of biological stimuli (cells, proteins) further enhancing the bone healing capacity.

2. The mechanical environment evolves in the defect (due to the regeneration process), so that an initially favourable scaffold design for bone regeneration would not be the one yielding the actual best bone regeneration at the end of the healing process.

3. A one-fits-them-all approach is doomed to failure: scaffold design needs to be adapted to the bone defect, and its geometry is not necessarily homogeneous throughout the scaffold

1.5   Thesis outline

After presenting the background, state of the art and focus of this work in the Introduction (Chapter 1), methods and algorithms used and developed during the thesis are described in Chapter 2. Then, the results obtained for the different thesis objectives are presented and discussed in three different chapters concerning the *in silico* modelling of scaffold-supported bone regeneration (Chapter 3), the scaffold design parametric studies (Chapter 4) and the scaffold design optimisation (Chapter 5). Chapter 6 highlights the conclusions and perspectives derived from this work. An overview of the thesis structure is depicted in Figure 1.9.
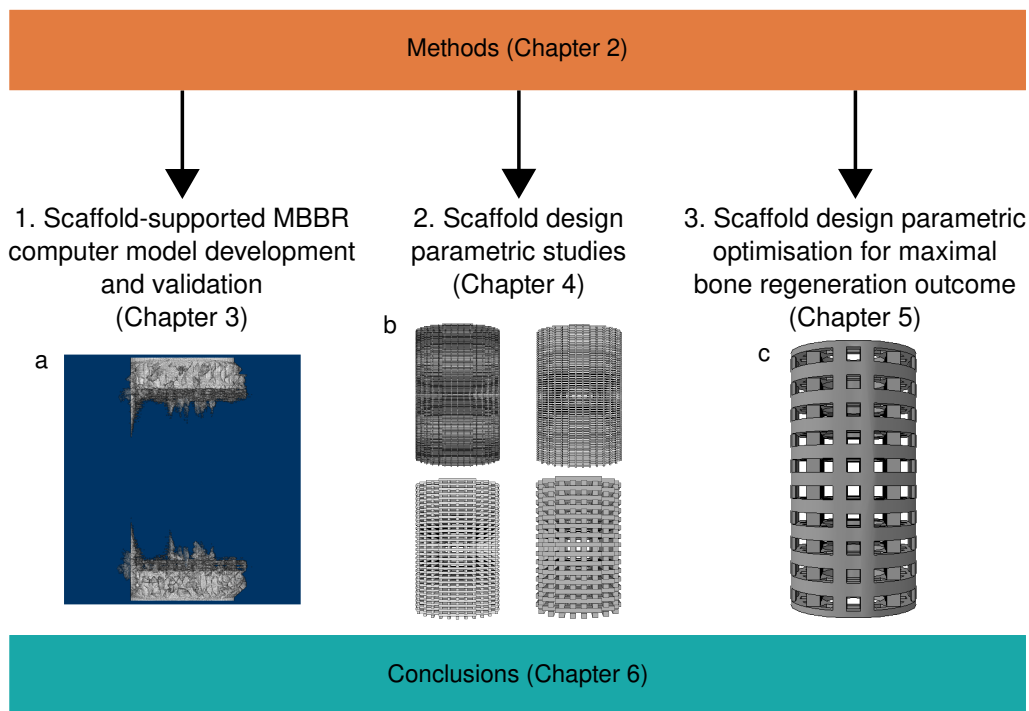
Figure 1.9 – Thesis outline and objectives: (a) bone regeneration prediction (in grey); (b) comparison of different scaffold designs (varying strut size); (c) scaffold design definition for optimisation. MBBR stands for mechano-biological bone regeneration.

2

Methods

This chapter will describe the methods used in the various studies of the thesis (Figure 1.9). First, the developed *in silico* model for scaffold-supported bone regeneration and its application to three experimental cases will be detailed (Section 2.1). Focus of the next section will be the parametric studies performed on predefined scaffold geometries to study the predicted impact of certain design parameters on the healing potential, and the evolution of the mechanical environment and subsequent tissue regeneration predictions over the course of healing (Section 2.2). Lastly, the developed bone scaffold design optimisation framework and its application to two scaffold geometries will be described (Section 2.3).

2.1 *In silico* model of scaffold-supported bone regeneration

A previously developed and validated multi-scale computer model for bone healing was complemented to account for scaffold-supported large bone defect regeneration [33, 49]. This model coupled a finite element (FE) model at the macroscopic scale to investigate the mechanical environment in the defect (Section 2.1.2) and a stochastic ABM at the microscopic scale to describe cellular activity (Section 2.1.3). Figure 2.1 depicts the flow chart of this coupled computer model: after FE model and ABM initialisation, a first FEA is conducted; the mechanical stimulus is derived from local mechanical values; cell differentiation, apoptosis, proliferation and migration are then simulated; the new cell distribution is output to a raw file for further analysis; the FE model material properties are updated depending on this new distribution; and ageing of the cells is implemented. The whole loop is run iteratively for an appropriate time (6 or 12 months), with one iteration corresponding to one healing day.

Different rules were tested to account for the effect of the defect size, the scaffold presence and the addition of biologically stimulating material (e.g. autologous bone graft). Only one simulation was run for each simulation case, as a preliminary study showed that this was enough to draw reliable conclusions from the stochastic model (cf. Appendix A.1). The model predictions were compared to previously conducted and published experimental studies described in Section 2.1.1.
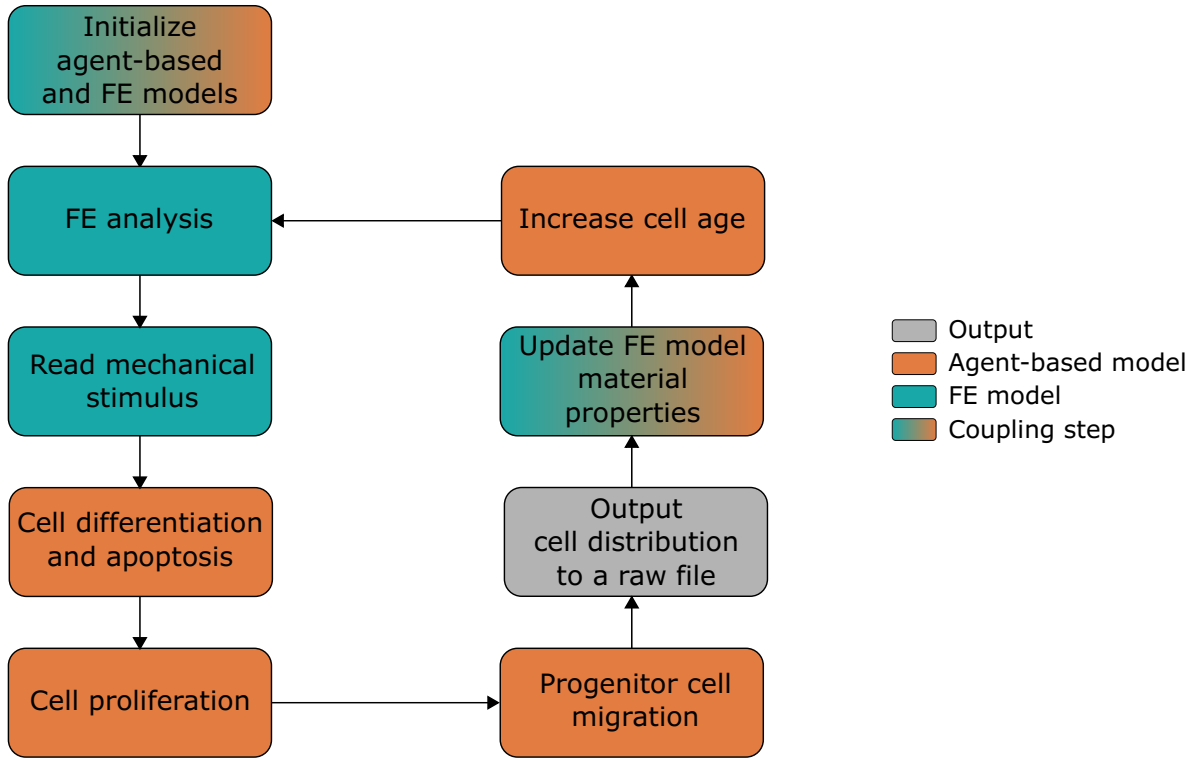
Figure 2.1 – **Computer model framework for bone regeneration**: Coupled agent-based model and finite element analysis.

2.1.1 Simulated *in vivo* experiments

2.1.1.1 Honeycomb titanium scaffolds

The first study aimed at investigating the mechanisms behind bone regeneration within a honeycomb titanium scaffold inserted in a large bone defect in the sheep tibia [13]. Briefly, a 4-cm bone defect was created in the right tibia of 12 sheep and filled with one of two possible scaffold designs, "soft" (strut size 1.2 mm, effective Young's modulus 0.84 GPa) or "stiff" (strut size 1.6 mm, effective Young's modulus 2.88 GPa) (Figure 2.2 c, d). The bone defect was stabilised using a steel locking compression plate. Autologous bone graft was harvested from each animal's iliac crest and filled into the scaffold pores before implantation. Outputs of this study were (1) X-ray images taken every 4 weeks, from surgery time until 24 weeks post-surgery and (2) histomorphometrical analysis performed on the mid-sagittal cut of all tibiae at 24 weeks post-surgery to visualise and quantify bone and cartilage formation within the defect. The remaining of the thesis will focus mainly on the softer titanium scaffold design and the expression "**titanium scaffold**" will refer to the softer titanium scaffold.

2.1.1.2 Lattice-based composite scaffold and empty defect

The second study consisted in investigating the mechanisms behind bone regeneration in sheep tibia large defects left either empty or complemented with a lattice-based, composite scaffold made of 20% TCP (ceramic) and 80% PCL (polymer) [9]. 3-cm osteotomies were performed in the sheep tibia and fixed with a steel internal dynamic compression plate (Synthes). Outputs of this study were (1) histological analyses of the mid-sagittal cut; (2) micro-computed

tomography (µCT) imaging of the defect; and (3) bone volume quantification. All analyses were performed 3 and 12 months post-surgery for the defect complemented with a scaffold, and only 3 months post-surgery for the empty defect. In the remaining of the thesis, these studies will be referred to as "**PCL scaffold**" for the defect complemented with the composite scaffold and "**Empty**" defect.
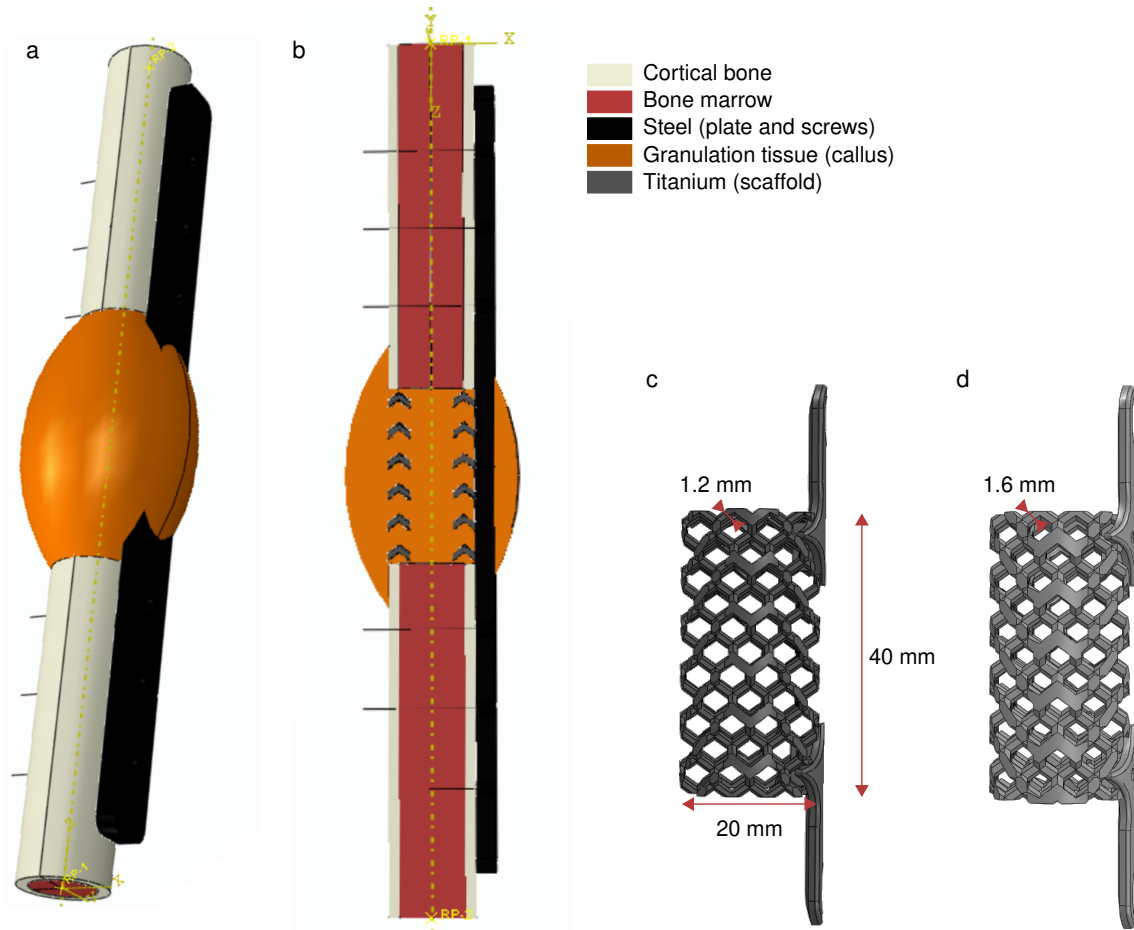
Figure 2.2 – **Titanium scaffolds set-up**: (a-b) Finite element model set-up including intact bone extremities, callus, scaffold, fixation plate and screws: (a) 3D external view; (b) longitudinal cross-section; colour code is given on the right; (c) "soft" scaffold (strut size = 1.2 mm); (d) "stiff" scaffold (strut size = 1.6 mm).

2.1.2 Finite element model (macroscopic scale)

2.1.2.1 Geometry

Titanium scaffolds and large bone defect model: A biphasic poro-elastic FE model of the experimental large bone defect and titanium scaffold was developed in the FE software Abaqus v. 6.12 (Simulia, Rhode Island) based on the experimental settings (Figure 2.2 a, b). Intact bone extremities were approximated as cylinders of diameter 20 mm containing the bone marrow cavity (diameter 15 mm). The soft and stiff scaffold geometries were imported from the experimental CAD files (Figure 2.2 c, d); they were fixed to the intact bone extremities by two screws modelled with beam elements. The callus was defined by rotating a circle arc of maximum width 10 mm at mid-height and overlapping the intact bone extremities over 10 mm;

the obtained volume was then cut by the scaffold geometry using Abaqus Boolean cut operation. A preliminary study suggested no effect of the callus size definition on the predicted tissue regeneration in its centre (between the intact bone extremities) (Appendix A.4); therefore, a rather small callus derived from the experimental data was used. Lastly, the plate was defined according to its experimental geometry and six screws modelled as beams attached the plate to the bone extremities (Figure 2.2 a, b).

PCL scaffold and large bone defect model: An elastic FE model of the experimental osteotomy and PCL scaffold was developed in the FE software Abaqus v. 6.18 (Simulia, Rhode Island) based on the experimental settings (Figure 2.3 a). Intact bone extremities were approximated as oval cylinders of long and short axes of 17 and 15 mm, respectively, containing the bone marrow cavity defined by axes of 13 and 11 mm. The plate was defined according to its experimental geometry and six screws modelled as beams attached the plate to the bone extremities.

The scaffold geometry was built based on its description (Figure 2.3 b-d): an individual cylindrical strut of diameter 0.3 mm was defined and repeated with a spacing of 1.2 mm to generate one row of struts; this row was repeated and rotated by an angle of 90°. Both rows were merged and cut to reproduce two rows of the hollow cylinder geometry of the scaffold with inner diameter 8 mm and outer diameter 20 mm. They were then meshed, repeated vertically to cover the full scaffold height, and the meshes were merged. This procedure was used as a direct meshing of the full scaffold structure was not possible on a standard work-station due to its numerous small geometrical components.

The external callus geometry was defined by rotating a circle arc of maximum width 10.5 mm at mid-height and overlapping the intact bone extremities over 5 mm. To obtain the internal callus geometry cut by the scaffold, a similar procedure was performed as to build the scaffold itself: first, a height corresponding to two scaffold strut layers was defined and cut by the scaffold layers. This callus layer was meshed and the meshes were then duplicated and merged together and with the external callus part.

Empty large bone defect model: A similar osteotomy model was developed without a scaffold for the empty defect set-up. Because there was no scaffold, the callus did not need to be cut and obtained by successive merges as for the PCL scaffold set-up. Apart from that, the geometry was exactly the same.
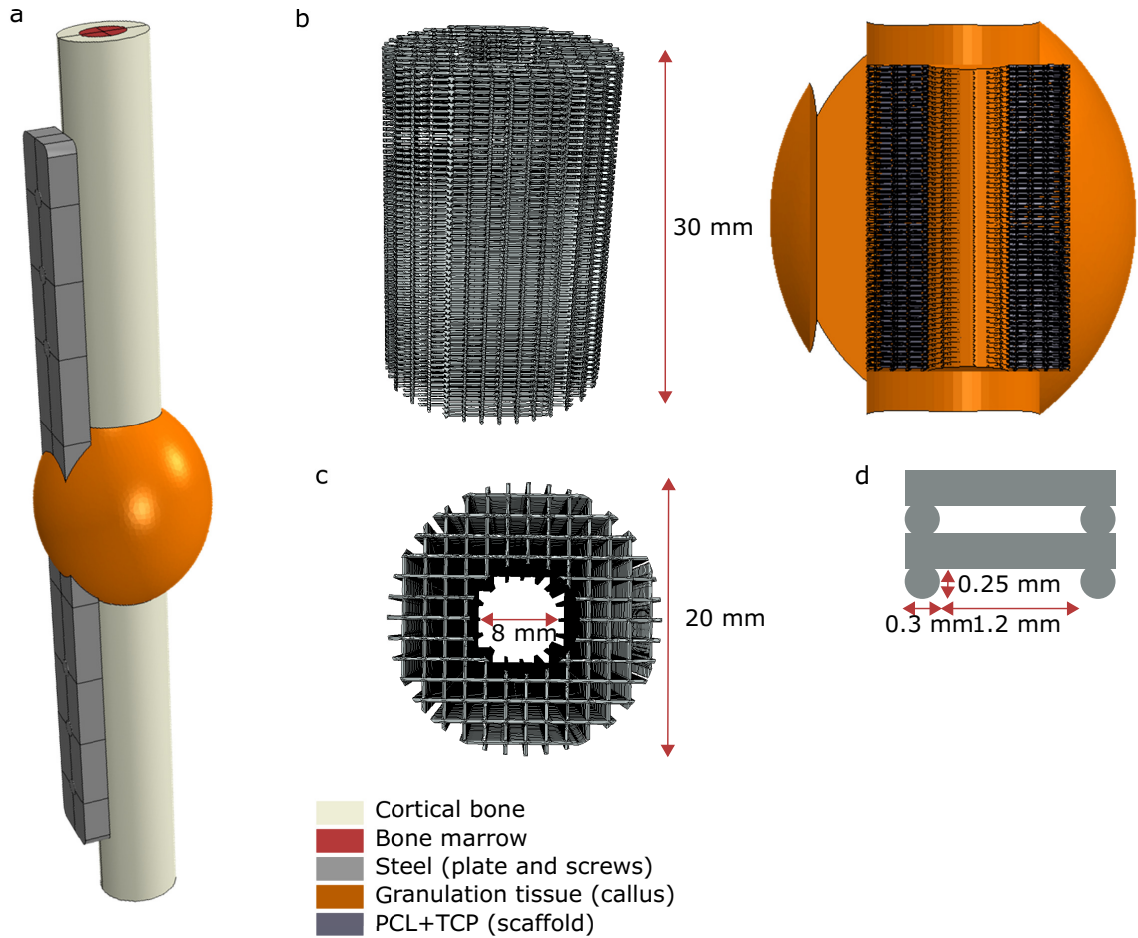
Figure 2.3 – **PCL scaffold set-up**: (a) Finite element model set-up including intact bone extremities, callus, scaffold, fixation plate and screws (colour code is given on the bottom); (b) scaffold seen from the side and longitudinal cross-section of the callus and the scaffold; (c) scaffold seen from the top; (d) details on strut dimensions and spacing.

2.1.2.2 Material properties

All biological tissues in the titanium scaffold FE model were considered biphasic poro-elastic materials with properties defined in Table 2.1. Scaffold titanium, plate and screw steel and all materials in the PCL scaffold FE model were considered linear elastic materials with properties defined in Tables 2.1 and 2.2. At the initial healing time-point, the callus was considered to be filled with granulation tissue.

In addition to the intact cortical bone, the bone marrow and the initial granulation tissue, tissue properties were defined for the regenerating tissues – fibrous tissue, cartilage, immature bone, mature bone (Tables 2.1, 2.2). Over the simulation time, the material properties of each callus FE were defined based on a rule of mixture [50] as an average of the material properties of its cellular components (see Section 2.1.3); they were further averaged over the last ten iterations to account for the delay in actual extracellular matrix (ECM) deposition [34].

In the PCL scaffold study, due to a very high number of callus FE, their material properties were not described individually as above, but they were grouped in material sections corresponding to material property "pools" with average values and ranges given in Table 2.2. These pools were defined in a preliminary study (Appendix A.6).

Material	Young's modulus (MPa)	Poisson's ratio	Permeability (10^{-14} s.m^4.N^{-1})	Bulk modulus grain (MPa)	Bulk modulus fluid (MPa)
Steel	210000	0.3	-	-	-
Titanium	104000	0.3	-	-	-
Granulation tissue	0.2	0.167	1	2300	2300
Fibrous tissue	2	0.167	1	2300	2300
Cartilage	10	0.3	0.5	3700	2300
Immature bone	1000	0.3	10	13940	2300
Mature bone	17000	0.3	37	13940	2300
Cortical bone	17000	0.3	0.001	13920	2300
Marrow	2	0.167	1	2300	2300

Table 2.1 – Material properties for titanium scaffold simulations [33]

2.1.2.3 Mesh

The FE models for the titanium scaffold defect configurations were meshed with elements of following types and sizes: quadratic hexahedral elements of size 2.5 mm for the cortical bone, the bone marrow (type C3D20RP) and the fixation plate (type C3D20R); quadratic 1-mm beam elements for the screws (type B32); quadratic tetrahedral elements of size 0.7 mm for the titanium scaffold (type C3D10) and its callus (type C3D10MP). Because the biological tissue parts were considered poro-elastic, the corresponding elements were of a type allowing pore fluid and stress analysis. A mesh convergence analysis for the scaffold and the callus was performed for the titanium scaffold set-up (Appendix A.2).

The FE models for the PCL scaffold defect configurations were meshed with linear hexahedral elements of size 1 mm for the cortical bone and 0.8 mm for the bone marrow (type C3D8R); quadratic hexahedral elements of size 4 mm for the fixation plate (type C3D20R); linear 1-mm beam elements for the screws (type B31); linear tetrahedral elements of size 0.3 mm for the PCL scaffold and of size 0.8 mm for its complementary callus (type C3D4); or quadratic tetrahedral elements of size 1.8 mm for the empty defect callus (without a scaffold) (type C3D10).

2.1.2.4 Loading and boundary conditions

All 3 osteotomy models were subjected to a combined compression and bending load corresponding to the peak loads in normal walking condition in sheep [110] and applied on the intact bone proximal end: a 2 body weights (BWs) proximal-distal compression and an anterior-posterior moment of 0.025 BWm at the fixed end of a 20-cm intact bone. Given the average weights of the sheep in each experimental study (70 and 42 kg), these translated to 1372 N compression and 17.125 Nm bending for the titanium scaffold study; and 823 N and 9.777 Nm for the PCL scaffold and empty defect studies.

The bone distal extremity was constrained in rotation and translation (encastre). The intact bone extremities were tied to the callus, and the screws were tied to the intact bone

Material name	Young's modulus range (MPa)	Young's modulus (MPa)	Poisson's ratio
Steel	-	210000	0.3
mPCL-TCP[a]	-	400	0.3
Granulation tissue[b]	-	0.2	0.167
Fibrous tissue[b]	-	2	0.167
Cartilage[b]	-	10	0.3
Regenerated and cortical bone[b]	-	17000	0.3
Marrow[b]	-	2	0.167
Material pool no.1	0.2	0.2	0.167
Material pool no.2	0.2-0.36	0.28	0.167
Material pool no.3	0.36-0.5	0.43	0.167
Material pool no.4	0.5-0.7	0.6	0.167
Material pool no.5	0.7-1	0.85	0.167
Material pool no.6	1-1.5	1.25	0.167
Material pool no.7	1.5-2	1.75	0.167
Material pool no.8	2-4	3	0.167
Material pool no.9	4-6	5	0.167
Material pool no.10	6-10	8	0.167
Material pool no.11	10-30	20	0.167
Material pool no.12	30-50	40	0.167
Material pool no.13	50-80	65	0.167
Material pool no.14	80-150	115	0.17
Material pool no.15	150-250	200	0.17
Material pool no.16	250-400	325	0.17
Material pool no.17	400-600	500	0.17
Material pool no.18	600-1000	800	0.17
Material pool no.19	1000-1500	1250	0.18
Material pool no.20	1500-2000	1750	0.18
Material pool no.21	2000-3000	2500	0.19
Material pool no.22	3000-4000	3500	0.19
Material pool no.23	4000-5000	4500	0.20
Material pool no.24	5000-6000	5500	0.21
Material pool no.25	6000-7000	6500	0.22
Material pool no.26	7000-8000	7500	0.23
Material pool no.27	8000-9000	8500	0.23
Material pool no.28	9000-10000	9500	0.24
Material pool no.29	10000-11000	10500	0.25
Material pool no.30	11000-12000	11500	0.26
Material pool no.31	12000-13000	12500	0.26
Material pool no.32	13000-14000	13500	0.27
Material pool no.33	14000-15000	14500	0.28
Material pool no.34	15000-16000	15500	0.29
Material pool no.35	16000-17000	16500	0.30

[a] [72]; [b] [33]

Table 2.2 – Material properties for PCL scaffold simulations
– the Young's modulus range indicates what material properties were included in each material pool.

extremities. In addition, multi-point constraints of type beam were defined between the plate holes and the screws' heads.

In the titanium scaffold set-up, the callus was tied to the scaffold. For the poro-elastic analysis, pore pressure was additionally constrained to be zero on the poro-elastic parts' outer surface (callus, cortical bone, bone marrow).

In the PCL scaffold set-up, the scaffold and the callus meshes were merged to avoid a very costly tie procedure due to the high number of elements involved.

2.1.3 Agent-based model (microscopic scale)

An ABM (turquoise boxes in Figure 2.1) was implemented in C++ [111] to describe cellular activities within the callus (differentiation, apoptosis, proliferation and migration). It was coupled with FEA runs every 3 iterations (3 simulated days) (see Appendix A.3 for the choice of frequency) to update the regenerating tissue material properties (Section 2.1.2.2) and get the local mechanical signals in the defect needed to predict further cellular activity based on the mechanoregulation theory (Section 2.1.3.2). The C++ implementation is available on Github under Apache 2.0 license [1].

2.1.3.1 Cell phenotypes

The ABM consisted in a 3D, regular point matrix with spacing $100\,\mu m$ and spanning over the callus space. Each matrix point could be occupied by one agent (i.e. cell) of one of the following phenotypes: fibroblast, chondrocyte, osteoblast or MSC. In the titanium scaffold set-up, a further differentiation was made between mature and immature osteoblasts. Each matrix point was matched to the regenerating tissue FE at the same location to ensure the coupling between ABM and FEA.

In reality, these cell types have diameters ranging from 10 to $25\,\mu m$ [112], so one matrix point in the ABM would correspond to many cells and their corresponding surrounding tissue – fibrous tissue, cartilage, (mature or immature) bone or granulation tissue. In the rest of the thesis, one point will refer to either the tissue or the cell, neglecting the fact that there are many cells present in each point. It should be noted that the choice of this matrix point size impacted the speed of the simulated healing process, but not its overall final tissue distribution (see Appendix A.5), what was the key interest.

At the initial time step, only MSCs were assumed to be present, and they were placed in the bone marrow volume closest to the defect and in the periosteum (region surrounding the intact bone extremities) with a 30% occupancy rate (MSCs were placed randomly in 30% of the available volume of these regions), unless specified differently.

2.1.3.2 Cellular activity implementation

The implementation described below corresponds to the baseline model derived from fracture healing computer simulations [33]. Baseline activity rate levels are summarised in

---

1. `github.com/camille-PM/mechanobio_bone`, `github.com/camille-PM/mechanobio_bone_2`

Cell type	Proliferation rate (day^{-1})	Apoptosis rate (day^{-1})	Differentiation rate (day^{-1})	Migration speed (µm.h^{-1})
MSCs	0.6[a]	0.05[a]	0.3[a]	30[b]
Fibroblasts	0.55[a]	0.05[a]	-	-
Chondrocytes	0.2[a]	0.1[a]	-	-
Osteoblasts	0.3[a]	0.16[a]	-	-

[a] [112]; [b] [113]

Table 2.3 – **Cell activity levels** [33]

Table 2.3. Next sub-sections will present variations that were implemented to account for scaffold or graft presence in a large bone defect.

Cell migration   The only cells allowed to migrate were the MSCs. In the baseline model, they were implemented to follow a random walk process. At each iteration, for each MSC, a new cell position was randomly picked among its six adjacent neighbour positions. If the position was free, the cell was moved there. This process was repeated seven times in one iteration (one simulated day) to account for the maximum distance that MSCs can migrate in one day given their average speed of 30 µm.h^{-1} [113].

Cell differentiation   MSCs were implemented to differentiate with a rate of 0.3 per day. In each FE of the callus, the amount of MSCs were counted and the number of cells to differentiate was computed. Points were then randomly picked in the FE, and if occupied by a MSC, this cell was implemented to differentiate and a cell counter was incremented. This step was repeated until the cell counter reached the number of cells to differentiate. To define what cell phenotype the differentiated cell should have, mechanoregulation theories were used, with a stimulus based on octahedral shear strain and relative fluid velocity for the titanium scaffold set-up [34] and on minimal principal strain and hydrostatic stress for the PCL scaffold set-up [32, 114] (Figure 1.3). In addition to the regions corresponding to fibroblast, chondrocyte and (mature or immature) osteoblast, those mechanoregulation theories also predicted a resorption zone, where no tissue would be favoured.

Cell proliferation and apoptosis   All cell phenotypes were implemented to proliferate or die due to apoptosis according to the rates given in Table 2.3. The principle was similar to the cell differentiation algorithm, counting the number of cells of each phenotype in each FE and computing the number of cells to proliferate, when the FE was in the stimulus favouring this phenotype, or that would undergo apoptosis, when the FE was in a different stimulus. Cells that would undergo apoptosis or proliferate were then randomly picked until the number was reached. When undergoing apoptosis, the cell was removed from the 3D matrix, i.e. its position was released. When proliferating, two new positions were chosen for the daughter cells among the adjacent and current cell positions (what made a total of 21 possible configurations) and checked for being free.

Cell ageing   Cells were given an age, starting at 1 at the initialisation step or when cells were obtained from proliferation. This age was used to define which cells could differentiate, as only "mature" MSCs aged at least 6 days could differentiate. At the end of each iteration (one healing day), the age of all cells present in the ABM was increased.

2.1.3.3   Alterations in biological activity within large bone defects

Latency period implementation   Experimentally, large bone defects are known to show only limited bone formation [1, 74]. This observation was accounted for by implementing a latency period of 15 days after which MSC migration and proliferation would stop, lacking the necessary biological stimulation [54]. This feature was implemented in the titanium scaffold set-up to serve as a hypothetical non-stimulated case for further model feature evaluation.

In the PCL scaffold and empty defect set-ups, the cell activity levels were reduced after the 15-day latency period: all cell types' proliferation rates and MSC differentiation rate were divided by 5 for the empty defect, and by 2 for the defect complemented with the PCL scaffold (Table 2.4). This difference was due to the TCP presence in the PCL scaffold that has been reported to stimulate cell proliferation [115, 116] and differentiation [117, 118].

Case	Proliferation rates (day^{-1})				MSC differentiation rate (day^{-1})
	MSC	**FB**	**CC**	**OB**	
Empty defect	0.12	0.11	0.04	0.06	0.06
TCP-PCL scaffold	0.3	0.275	0.1	0.15	0.15

Table 2.4 – Cell activity levels after the latency period – FB: fibroblast, CC: chondrocyte, OB: osteoblast

Systematic cell activity analysis (PCL scaffold)   In the PCL scaffold study where no graft was present, thus allowing a better cell activity evaluation, a preliminary systematic analysis of the cell activity rates was performed. The migration speed was tested at baseline level ($30\ \mu\text{m.h}^{-1}$) and twice faster ($60\ \mu\text{m.h}^{-1}$); the proliferation rates were tested at their baseline levels (Table 2.3) and divided by two for all cell types; and the differentiation rate was tested at its baseline level (0.3) and divided by two (0.15). All different level combinations were run to investigate both individual and combined effects and are summarised in Table 2.5. They were simulated in combination with surface-guided ECM deposition (Section 2.1.3.4).

Graft stimulating effects (titanium scaffold)   In the experiments, the titanium scaffolds were filled with ABG [13]. The exact composition and effect of ABG remains to be elucidated, but it is generally assumed that it has very good osteoconductive (guiding new bone in-growth) and osteoinductive properties (enhancing bone deposition) and that it might contain MSCs contributing to the healing [3]. Those different effects were modelled independently and in combination, together with the latency period implementation, as follows:

1. **Osteoconductive effects** after the latency period previously described, only the MSCs present in the regions containing ABG (within the scaffold pores) continued migrating and proliferating. In the titanium scaffold set-up, this meant that MSC migration

Case	Proliferation rates (day^{-1})				MSC differentiation rate (day^{-1})	MSC migration speed (µm.h^{-1})
	MSC	FB	CC	OB		
1	0.6	0.55	0.2	0.3	0.3	30
2	0.6	0.55	0.2	0.3	0.3	60
3	0.6	0.55	0.2	0.3	0.15	30
4	0.3	0.275	0.1	0.15	0.3	30
5	0.6	0.55	0.2	0.3	0.15	60
6	0.3	0.275	0.1	0.15	0.3	60
7	0.3	0.275	0.1	0.15	0.15	30
8	0.3	0.275	0.1	0.15	0.15	60

Table 2.5 – Cell activity level sensitivity analysis – FB: fibroblast, CC: chondrocyte, OB: osteoblast

and/or proliferation were limited to the scaffold pores after 15 days (see Algorithms 1 and 2 for implementation details).

2. **Osteoinductive effects** after the latency period previously described, the MSCs present in the regions containing ABG had an enhanced differentiation capacity: the MSC differentiation rate was increased to 0.5 in the scaffold pores after 15 days.

3. **MSC presence** in addition to the bone marrow and periosteum, MSCs were initially seeded in 0.1% of the scaffold pore volume.

Algorithm 1 Pseudo-code for graft osteoconductive effect on migration, adapted from [119]: *cell* is an agent in the 3D array of the ABM, with 0 indicating a free position and 1 a location occupied by a MSC; the function *neighbours*() returns the six adjacent neighbours of a given position *pos*; the Boolean function *graft*() returns true if graft is present at the position (i.e. in the scaffold pores).

---

for $element \in [1, total\_number\_of\_elements]$ **do**
    for $pos \in elem$ **do**
        if $cell(pos) = 1$ **then**
            $counter \leftarrow 0$
            while $counter < 7$ **do**
                $new\_pos \leftarrow rand(neighbours(pos))$
                if $cell(new\_pos) = 0$ **and** $graft(new\_pos)$ **then**
                    $cell(new\_pos) \leftarrow cell(pos)$
                    $cell(pos) \leftarrow 0$
                    $counter \leftarrow counter + 1$
                end if
            end while
        end if
    end for
end for

2.1.3.4 Scaffold surface guidance

According to experimental observations, scaffold surfaces act as guiding templates for the cell migration and/or new ECM deposition [13, 42, 45, 46]. Two new features were therefore implemented, as detailed in the pseudo-codes given in Algorithms 3 and 4:

Algorithm 2 Pseudo-code for graft osteoconductive effect on MSC proliferation, adapted from [119]: *cell* is an agent in the 3D array of the ABM, with 1 indicating a location occupied by a MSC; the function *neighbours*() returns the six adjacent neighbours of a given position *pos*; the Boolean function *graft*() returns true if graft is present at the position (i.e. in the scaffold pores); the function *proliferate*() creates two daughter cells from the current cell.

---

for $elem \in [1, total\_number\_of\_elements]$ **do**
    $counter \leftarrow 0$
    for $pos \in elem$ **do**
        if $cell(pos) = 1$ **then**
            $counter \leftarrow counter + 1$
        end if
    end for
    $cells\_to\_proliferate \leftarrow counter * proliferation\_rate$
    $counter \leftarrow 0$
    while $counter < cells\_to\_proliferate$ **do**
        $pos \leftarrow rand(positions \in elem)$
        if $cell(pos) = 1$ **and** $graft(pos)$ **then**
            $proliferate(cell(pos))$
            $counter \leftarrow counter + 1$
        end if
    end while
end for

---

1. **Surface-guided cell migration** In the migration process, the random choice of a new position for the migrating cell was further conditioned by the presence of an adjacent surface, i.e. a position occupied by either previously deposited tissue (bone, cartilage, fibrous tissue) or scaffold. This meant that MSCs would be able to migrate following existing surfaces but not anywhere else in the granulation tissue.

2. **Surface-guided ECM deposition** As ECM deposition is not modelled as such in the computer model, this effect was implemented in the differentiation process, where a new cell type is created that will further deposit its corresponding ECM. MSCs were therefore allowed to differentiate into a new cell phenotype only when at least one of the adjacent neighbour cells was a previously deposited tissue (bone, cartilage, fibrous tissue) or scaffold. This meant that new ECM deposition would need a pre-existing substrate to attach to and would not happen *ex nihilo*.

Based on the experimental observations, the fixation plate surface was hypothesised to give surface guidance cues in the PCL scaffold set-up (bone growth was seen onto the plate [9]) but not in the titanium scaffold set-up (no bone growth observed onto the plate [13]). Surface-guided migration and ECM deposition were implemented independently for the titanium scaffold to study their individual effect, and together for the PCL scaffold and empty defect.

Algorithm 3 Pseudo-code for surface-guided migration implementation, adapted from [119]: *cell* is the 3D array of the ABM, with 0 indicating a free position, 1 a MSC and other integer numbers the other cell phenotypes; the function *neighbours*() returns the six adjacent neighbours of a given position *pos*

---

for $elem \in [1, total\_number\_of\_elements]$ **do**

    for $pos \in elem$ **do**

        if $cell(pos) = 1$ **then**

            $counter \leftarrow 0$

            while $counter < 7$ **do**

                $new\_pos \leftarrow rand(neighbours(pos))$

                if $cell(new\_pos) = 0$ **and** $tissue \in neighbours(new\_pos)$ **then**

                    $cell(new\_pos) \leftarrow cell(pos)$

                    $cell(pos) \leftarrow 0$

                    $counter \leftarrow counter + 1$

                end if

            end while

        end if

    end for

end for

Algorithm 4 Pseudo-code for surface-guided ECM deposition implementation, adapted from [119]: *cell* is the 3D array of the ABM, with 1 indicating a MSC; the function *neighbours*() returns the six adjacent neighbours of a given position *pos*; the function *cell_code*() returns the code of the cell phenotype depending on the mechanoregulation stimulus

---

for $elem \in [1, total\_number\_of\_elements]$ **do**

    $counter \leftarrow 0$

    for $pos \in elem$ **do**

        if $cell(pos) = 1$ **then**

            $counter \leftarrow counter + 1$

        end if

    end for

    $cells\_to\_differentiate \leftarrow counter * differentiation\_rate$

    $counter \leftarrow 0$

    while $counter < cells\_to\_differentiate$ **do**

        $pos \leftarrow rand(positions \in elem)$

        if $cell(pos) = 1$ **then**

            if $tissue \in neighbours(pos)$ **then**

                $cell(pos) \leftarrow cell\_code(stimulus)$

                $counter \leftarrow counter + 1$

            end if

        end if

    end while

end for

2.1.3.5   Influence of MSC seeding on regeneration outcome and patterning

The computer model for scaffold-supported bone regeneration comparing best to the experiments was then used to investigate the mechanisms behind healing under initial seeding of MSCs in the implanted scaffold [9]. Specifically, the effect on the regenerated bone volume and patterning of initially seeding different numbers of MSCs randomly distributed in the PCL scaffold pores was studied. To do so, the same set-up was used as for the PCL scaffold, with latency period implementation, stimulation by TCP and surface-guided migration and tissue deposition. At the initial time-point of the simulations, MSCs were seeded randomly in the scaffold pores: 100, 10 000 and 1 million lattice points were initialised with MSCs.

2.1.4   Outcome analysis and visualisation

The computer simulation results were analysed and output comparable to the experimental data was generated: histology images (stained longitudinal cross-section of the bone defect), X-ray images for the titanium scaffold, μCT images for the PCL scaffold and bone surface or volume quantification in given regions of interest (ROIs).

2.1.4.1   Histology-like images

In the titanium and PCL scaffold experiments, histology of the mid-sagittal plane was performed with a Safranin Orange/von Kossa staining, 24 weeks post-surgery for the titanium scaffold and 3 and 12 months post-surgery for the PCL scaffold. This staining reveals bone in black, cartilage in dark red and fibrous tissue in light red. The simulation-predicted tissue distributions in the same plane and at the same time points were represented with 100-μm pixels in similar colours using the Python programming language (Python Software Foundation [2]) and its plotting library Matplotlib [120]. In addition, zones without any regenerated tissue were left white, and intact bone, scaffold and plate were depicted in grey nuances.

2.1.4.2   X-ray-like images

In the titanium scaffold experiment, monthly X-ray pictures were performed in the medial-lateral plane at 4, 8, 12, 16, 20 and 24 weeks post-surgery. Similar pictures were generated from the computer model predictions by using the Beer-Lambert law and neglecting soft tissue contribution and scattering, following the equation $I = I_0 e^{-kx}$ with I the observed intensity, I_0 an arbitrary initial density value set to 1, k the material attenuation coefficient and x the material thickness [121]. With x identified with the matrix point size (100 μm) and attenuation coefficients defined by the NIST [3], the attenuation on each ray direction was obtained by summing the individual point contribution. The corresponding X-ray image was deduced using the above formula in Python and Matplotlib and its contrast was adapted to compare best with the experimental X-ray images.

---

2. `https://www.python.org/`

3. `https://www.nist.gov/pml/x-ray-mass-attenuation-coefficients`

2.1.4.3   Micro-CT-like images

In the PCL scaffold experiments, µCT imaging of the defect zone was performed 3 and 12 months post-surgery. Similar images were generated from the simulation output: first, the files describing the tissue distribution were converted with a C++ routine in a binary format with 1 indicating – intact and regenerated – bone presence and 0 indicating all other material or void points. The obtained files were then visualised in the antero-posterior direction in ImageJ module VolumeViewer [4] [122]. The generated image depicts bone in grey shades (the lighter the grey tone, the thicker the bone) and the background in dark blue.

2.1.4.4   Quantification in regions of interest

Regenerated tissues were quantified in ROIs defined in Figure 2.4 using Matlab R2018b.

For the titanium scaffold, the bone proportion in the mid-sagittal plane in the lateral (1-cm wide), medial (1-cm wide) and central (1-cm high and 2-cm wide) ROIs (Figure 2.4 a) was deduced from the tissue distribution predictions by multiplying the number of bone tissue elements in the mid-sagittal plane by the point surface area ($0.01\,\mathrm{mm}^2$) and dividing the result by the ROI surface area. Cartilage was quantified in the same way but in the total ROI (union of lateral and medial ROIs). To ensure more comparable results between the *in silico* and *in vivo* quantification, the histological pictures were segmented after filling the pores seen in the regenerated bone; the *in silico* model does indeed not predict the bone porous micro-structure. Bone was then quantified using ImageJ [122].

For the PCL scaffold, bone volume was quantified by multiplying the amount of bone tissue elements by the point volume ($0.001\,\mathrm{mm}^3$). Quantification was performed in the inner duct and scaffold ROIs (Figure 2.4 b) and in the total ROI containing inner duct, scaffold and periphery regions. *In silico* quantification was compared to the µCT quantification obtained experimentally.

For the empty defect, only the total bone volume was quantified following the same process as for the PCL scaffold.
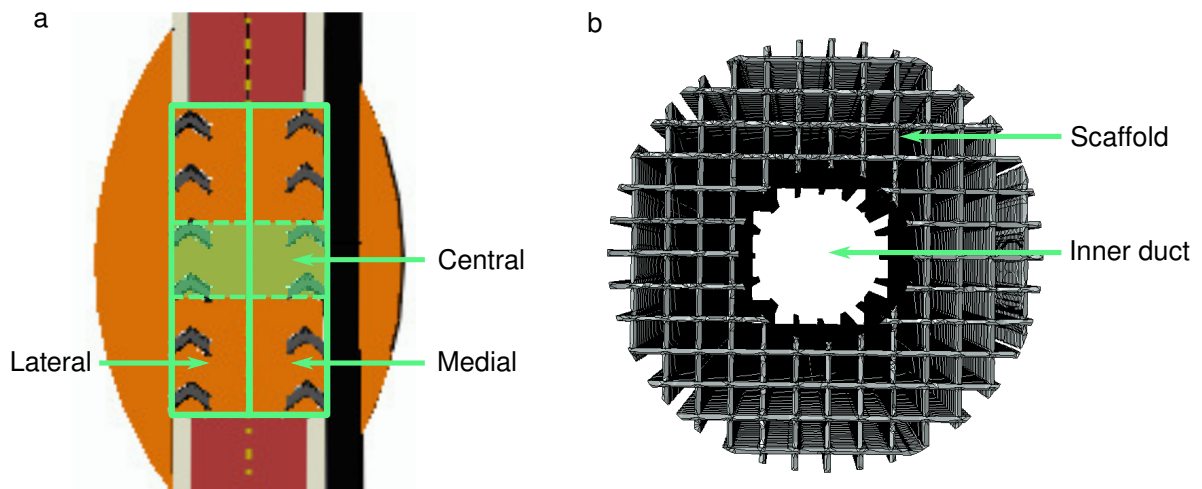
Figure 2.4 – ROI definition for bone quantification: (a) titanium scaffold: lateral, medial and central surface ROI definition; (b) PCL scaffold: inner duct and scaffold volume ROI definition.

---

4. `https://imagej.nih.gov/ij/plugins/volume-viewer.html`

2.1.5   Summary of bone regeneration simulation set-ups

Simulation set-ups for the titanium soft and stiff scaffolds whose results will be presented in Chapter 3 are summarised in Table 2.6. All simulation variations were tested with the soft titanium set-up; only the baseline simulation and the set-up obtaining best results (surface-guided ECM deposition with graft osteoconduction) were tested for the stiff titanium set-up (cases 13 and 14, respectively).

Simulation set-ups for the PCL scaffold whose results will be presented in Chapter 3 consisted in the 8 simulations for the cell activity sensitivity analysis described in Table 2.5; the baseline simulation; and the simulation with latency period (reduced proliferation and differentiation) and surface guidance (for MSC migration and ECM deposition) implementation.

For the empty defect, the baseline simulation and the simulation with latency period and surface guidance implementation were investigated.

	Simulation name	Scaffold	Latency period	Graft stimulation	Surface guidance
1	Baseline	Soft	No	-	-
2	Non-stimulated regeneration	Soft	Yes	-	-
3	Graft stimulation on cell migration	Soft	Yes	Osteoconduction	-
4	Graft stimulation on cell proliferation	Soft	Yes	Osteoconduction	-
5	Graft stimulation on cell differentiation	Soft	Yes	Osteoinduction	-
6	Combined osteoconduction and osteoinduction	Soft	Yes	Osteoconduction & -induction	-
7	Bone graft-contained MSCs	Soft	Yes	Initial MSC presence	-
8	Combined bone graft-contained MSCs with osteoconduction and osteoinduction	Soft	Yes	Initial MSC presence, osteoconduction & -induction	-
9	Surface-guided migration	Soft	Yes	-	Migration
10	Surface-guided migration with bone graft osteoconduction	Soft	Yes	Osteoconduction	Migration
11	Surface-guided ECM deposition	Soft	Yes	-	ECM deposition
12	Surface-guided ECM deposition with bone graft osteoconduction	Soft	Yes	Osteoconduction	ECM deposition
13	Baseline	Stiff	No	-	-
14	Surface-guided ECM deposition with bone graft osteoconduction	Stiff	Yes	Osteoconduction	ECM deposition

Table 2.6 − **Titanium scaffold simulations**: list of simulation set-ups with coding numbers, names and implementation details, adapted from [119]

2.2 Scaffold design parametric studies

In silico parametric studies were performed on different scaffold designs. First, the PCL scaffold design was altered (geometry and material properties) to investigate the effect of scaffold surface-area-to-volume ratio, strut size, pore size, inner radius and material properties on the healing potential (Section 2.2.1). Second, a parametric study was performed on a simplified cubic scaffold design to investigate the dynamics of the regeneration process and compare how biological tissues would be initially stimulated by the mechanics immediately post-surgery, with their actual regeneration predictions (Section 2.2.2).

2.2.1 PCL scaffold design effect on healing outcome

2.2.1.1 Surface-area-to-volume ratio

Four different scaffold architectures were investigated to study the effect of surface-area-to-volume ratio (SA/V) on the predicted regenerated bone. To do so, a strut-based scaffold was designed with rectangle-section struts and similar overall arrangement and material properties as the PCL scaffold (Section 2.1.2). To vary the SA/V, the strut size was varied: 125*150 µm, 250*300 µm (comparable to the circular struts of the PCL scaffold), 500*600 µm and 1000*1200 µm; while the pore size was kept constant (1200 µm). The resulting designs D1-D4, respectively, showed different porosities and strong variations in SA/V (Table 2.7). To further decouple SA/V from mechanical effects, a fifth design was investigated with the same architecture as D4 but a softer material (Young's modulus 70 MPa instead of 400 MPa) to generate strains within the scaffold pores comparable to the design D1; this last design was named D4_soft.

Design case	Strut width (µm)	Strut height (µm)	Scaffold porosity	SA/V ratio (mm^{-1})
D1	150	125	91%	278.21
D2	300	250	84%	137.81
D3	600	500	73%	65.57
D4	1200	1000	60%	31.79

Table 2.7 – **SA/V scaffold designs**. The scaffold porosity is defined as the porosity of the hollow cylinder (inner radius 8 mm, outer radius 20 mm) containing scaffold material.

2.2.1.2 Geometrical and material parameters

Sensitivity analysis of the PCL scaffold performance to three geometrical (strut size, inner cylinder radius, inter-strut distance) and one material (Young's modulus) parameters was investigated by means of a Taguchi array design of experiments (DOE) [123]. A similar scaffold design was used as for the SA/V study, with the following four design parameters: Young's modulus of the scaffold material, strut width (the strut height being obtained proportionally), inner cylinder radius (empty channel in the middle) and inter-strut distance (defining the pore size) (Figure 2.5). Three levels were defined for each parameter: Young's modulus at 400, 4000

and 40000 MPa, strut dimensions at 150*125, 300*250 and 600*500 µm, inner radius at 2, 4 and 6 mm and inter-strut distance at 600, 1200 and 2400 µm. A 3-level, 4-input parameters Taguchi array was used to define 9 designs denoted T1-T9 (Table 2.8). Due to a too complex and fine geometry, the design T1 could not be generated on available work-stations and will be discarded from the analysis.
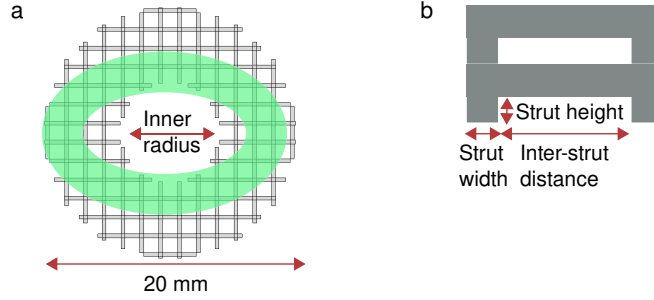
Figure 2.5 – **Geometrical and material property effects**: (a) radial view with ROI cross-section definition in light green and inner radius definition; (b) side view of scaffold struts and other geometrical parameter definitions

Design case	Young's modulus (MPa)	Strut width (µm)	Strut height (µm)	Inner radius (mm)	Inter-strut distance (µm)
T1	400	150	125	2	600
T2	400	300	250	4	1200
T3	400	600	500	6	2400
T4	4000	150	125	6	2400
T5	4000	300	250	4	600
T6	4000	600	500	2	1200
T7	40000	150	125	6	1200
T8	40000	300	250	2	2400
T9	40000	600	500	4	600

Table 2.8 – **Taguchi array scaffold designs**.

2.2.1.3   Bone regeneration prediction and outcome analysis

The mechanobiological bone regeneration (MBBR) computer model having best prediction capacity for the PCL scaffold (latency period, TCP stimulation and surface guidance) was used to predict bone regeneration in these PCL scaffold-derived designs. Visualisation of the outcome by means of µCT-like images 12 months post-surgery was performed and bone volume proportion was quantified in the inter-cortical ROI, the elliptical cylinder following the intact bone extremities (Figure 2.5 a).

In addition, for the SA/V study, the MSC activity was studied in detail:

Migration The distance between initial and last positions was computed for each MSC migrating at each iteration; next, the average distance migrated by the MSCs at each

iteration was computed. Although a migration speed of $30\,\mu\mathrm{m.h}^{-1}$ was assumed, it is expected that not all cells migrate the maximal distance allowed by this speed, either because neighbouring positions are already occupied or because they are not following existing surfaces (surface-guided migration).

Proliferation The number of MSCs actually proliferating at each iteration was divided by the total number of MSCs to compute the actual MSC proliferation rate. Although an MSC proliferation rate of 30% is implemented, it is expected that not all cells proliferate due to a lack of available neighbouring positions.

Differentiation The number of MSCs actually differentiating at each iteration was divided by the total number of MSCs to compute the actual MSC differentiation rate. Although an MSC differentiation rate of 15% is implemented, it is expected that not all cells differentiate due to the lack of pre-existing tissue, scaffold or plate adjacent neighbours (surface-guided ECM deposition).

2.2.2 Dynamics of the bone regeneration process: initial mechanics and regeneration predictions

The aim of this study was to investigate the healing potential of scaffolds optimised for their initial (post-surgery) stimulatory mechanical environment for bone regeneration. Therefore, the initial mechanical signals distribution (and corresponding favoured tissues) and the predicted tissue distribution after 60 days were assessed in various cubic scaffold designs.

In detail, cubic scaffolds of side $3\,\mathrm{mm}$ with varying square pore sizes were designed (Figure 2.6). Two independent variables were defined: the pore dimension in horizontal extruding directions x_1 and the pore dimension in vertical extruding direction x_2 (loading and cell source direction), both set to vary from 0.1 to $0.9\,\mathrm{mm}$ with 0.05-mm steps. Consecutive pore centres were placed at $1\,\mathrm{mm}$ from one another and there were 3*3 pores per scaffold face. All cases with at least 50% porosity were simulated, resulting in 181 simulation cases. This cube was subjected to a compression load of $15\,\mathrm{N}$ applied on its top face, while the bottom face was constrained in displacement and rotation (encastre).
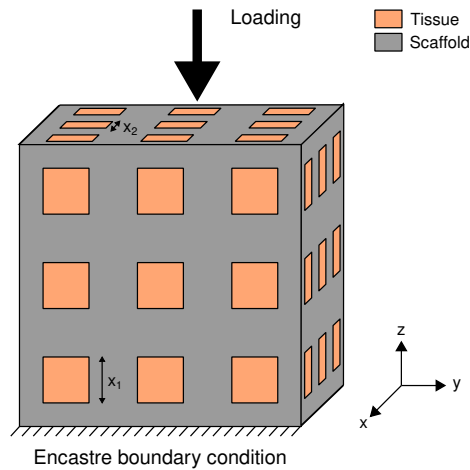
Figure 2.6 – **Non-graded cubic scaffold set-up**: variable definition, constraint and loading conditions

2.2.2.1 Outcome definition and mechanobiological models

The initial mechanical signals were based on the stress-strain stimulus defined for the PCL scaffold [32, 114]. The tissue present in the scaffold pores was modelled as granulation tissue (Table 2.2). In particular, the tissue volume fraction under bone-favouring initial mechanical signals was investigated.

The full regeneration set-up used the baseline model (fracture healing model) as defined for the PCL scaffold (Section 2.1), with smaller lattice points (20 µm) to ensure a good resolution in the smaller geometry. MSCs were initially seeded right above and below the cube (in the vertical direction) with a 30% occupancy rate. The tissue present in the scaffold pores was initialised as granulation tissue with properties updated over time as tissue was formed. In particular, the regenerated bone volume fraction after 60 days was investigated.

2.2.2.2 Geometry automatic update and meshing

For the initial signals and regeneration outcome, the scaffold and complementary tissue were defined parametrically using a Python script for Abaqus CAE. They were meshed with tetrahedra of average size 0.1-0.2 mm. A MATLAB script was used to modify the Python script, run the Python script in Abaqus CAE, and then run the Abaqus-C++ mechanobiological model with initial stimulus and final tissue distribution outcome after 60 days. The time of 60 days was chosen as it allowed to achieve a near-stationary state in scaffolds with intermediate-size pores. The detailed implementation is available on a Github repository [5].

2.2.2.3 Outcome analysis and visualisation

To evaluate the influence of pore sizes on predicted initial stimulus, regeneration outcome or remodelling outcome, heat-maps were designed on the (x_1, x_2) space. Colours ranged from red for worst designs (0.0 bone volume fraction or bone-favouring stimulus) to green for best designs (1.0 bone volume fraction or bone-favouring stimulus). To compare specific design outcome, histology-like images were generated, as described in Section 2.1.4.1.

2.3 Scaffold design optimisation

A computer framework was developed for large bone defect scaffold design optimisation. The following sections will describe the framework implementation and its application for two scaffold designs (cubic and cylindrical) with different geometrical (pore sizes) and material (Young's modulus) variable definitions. The objective of the optimisation was to maximise the amount of regenerated bone as predicted by an MBBR computer model. Indeed, the work presented in Chapter 4 hinted towards the need to include the complete regeneration process in the optimisation and not only the initial mechanics.

---

5. `https://github.com/camille-PM/cube_parametric_study`

2.3.1 Combined surrogate modelling and optimisation

Due to the computationally demanding MBBR simulations, direct scaffold design optimisation could not be performed. Instead, a surrogate optimisation framework was used (Figure 2.7). This framework took advantage of a surrogate model (a simplified input-output relationship between scaffold design variables and objective value) built on a first set of data to perform optimisation. Only the optimal design was then simulated using the bone regeneration computer model, and this process was repeated iteratively to ensure surrogate model accuracy (loop 1) and actual optimality of the computed optimum (loop 2). The following steps were performed:

1. Run MBBR simulation for a set of input parameters obtained by uniform sampling or Latin hypercube sampling (LHS)

2. Construct a surrogate model based on those sampled data

3. Perform optimisation using the surrogate model

4. Run MBBR simulation for the optimum and compare real value to surrogate prediction (loop 1) or current optimal value (loop 2)

5. Repeat steps 2-4 to ensure surrogate model accuracy and optimality of the result
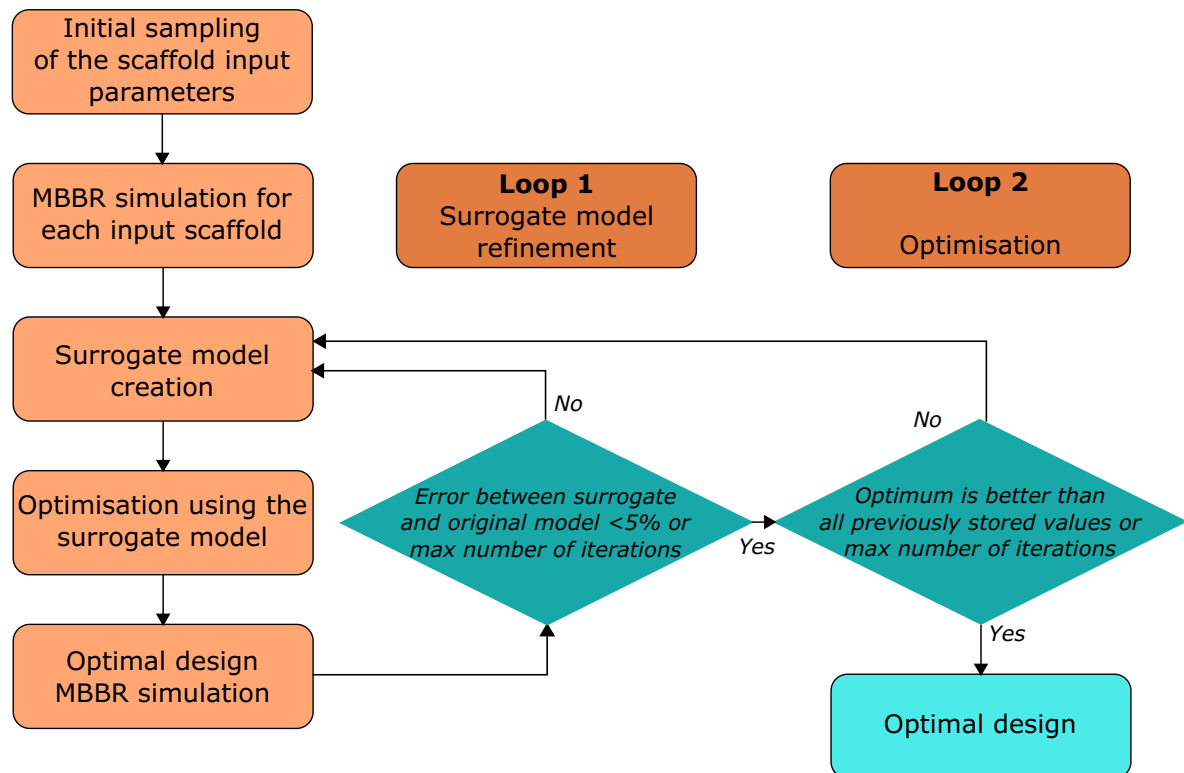
Figure 2.7 – **Flow chart of the surrogate optimisation framework**

2.3.2 Objective definition

The objective for all optimisation cases was set as to maximise regenerated bone volume at the end of the assumed healing time, after 60 days according to the baseline fracture healing model for the cubic scaffold (similar to Section 2.2.2); and after 24 weeks according to the

scaffold-supported bone regeneration computer model complemented with surface-guided ECM deposition and graft osteoconduction effects (stimulation of MSC migration and proliferation) for the cylindrical scaffold. The latter model was the one showing best results for the titanium scaffold (Chapter 3). As optimisation algorithms require a function to be minimised, the objective function was defined as follows:

$$f(\boldsymbol{x}) = 1 - \frac{V_{bone}}{V_{tissue}}(t_{end}) \tag{2.1}$$

with $\boldsymbol{x}$ the vector of optimisation variables, V_{bone} the volume of regenerated bone, V_{tissue} the available tissue volume in the scaffold pores and t_{end} the time defined in days: 60 for the cubic scaffold (2 months) and 168 for the cylindrical scaffold (24 weeks).

2.3.3 Scaffold geometries and constraint definitions

2.3.3.1 Cubic scaffold

A cubic scaffold of side 3 mm with 3*3 square-section pores in each face was defined, similar to the geometry used in the parametric study (Section 2.2.2). The lower face of the scaffold-tissue construct was constrained in displacement and rotation, while a distributed compression loading of 15 N was defined on the upper face (axis -z). In some of the optimisation cases (Table 2.9), a bending moment of 0.02 Nm around the y axis was added. The scaffold and complementary callus were meshed with tetrahedral quadratic elements (type C3D10) of average size 0.15 mm. Two different set-ups were defined, for the geometrical optimisation and for the material property optimisation.

For the **geometrical optimisation**, the variables were defined to describe the pore sizes in each horizontal row and along the z direction (Figure 2.8). A similar automated geometry and mesh update strategy was used as the one described in Section 2.2.2.2. The pore sizes were constrained between a lower bound (0.1 mm) and an upper bound (0.9 mm). When the chosen optimisation algorithm allowed for non-linear constraint definition, the resulting porosity of the scaffold was constrained to be at least 50%.

More precisely, 3 different cubic scaffold design geometries were optimised:

— a non-graded design with 2 variables, similar to the one used in the parametric study (Section 2.2.2, Figure 2.6)

— a graded design with 4 variables: x_1 to x_3 for the horizontal row pore sizes (taken equal in the x and y extruding directions) and x_4 for the pore sizes (all equal) in the z direction (Figure 2.8 a)

— a graded design with 7 variables: x_1 to x_3 (x direction) and x_4 to x_6 (y direction) for the horizontal row pore sizes and x_7 in the z direction (Figure 2.8 b)
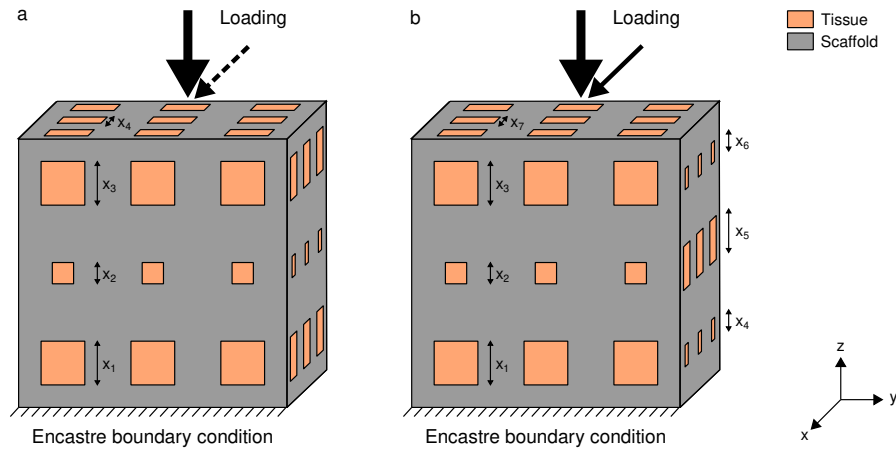
Figure 2.8 – **Graded pore cubic scaffold set-ups**: variable definition, constraint and loading conditions for (a) same pore sizes in x and y directions (4 variables); (b) different pore sizes in x and y directions (7 variables). The dotted arrow (a) indicates the bending load added in some cases only.

A similar cubic scaffold set-up was used for the **material optimisation** study, with pores of sizes 0.6 mm in all horizontal rows and 0.7 mm in the vertical direction. 7 material sections were defined in horizontal slices of the scaffold, following lines defined by upper and lower edges of the pores (Figure 2.9). Due to the symmetry of the loading and boundary conditions, symmetry in the material distribution was assumed above and below the middle plane. The remaining 4 independent sections were assigned a specific Young's modulus (variables E1-E4, Figure 2.9) that could vary from 10 MPa to 100 GPa, while the Poisson ratio was kept identical for all hypothetical scaffold materials (0.3).
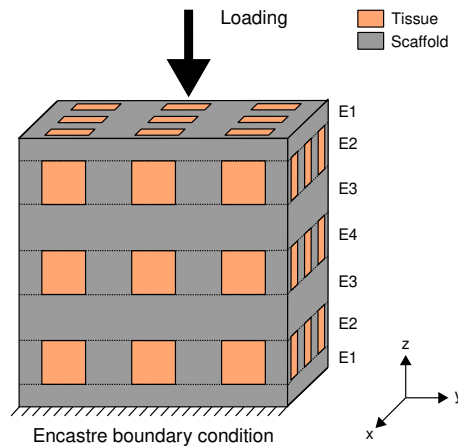
Figure 2.9 – **Cubic scaffold set-up for material optimisation**: variable definition (E1-E4), constraint and loading conditions.

2.3.3.2 Cylindrical scaffold

To perform geometrical optimisation of a more realistic scaffold design, a cylindrical scaffold was used in a set-up similar to the titanium scaffold set-up (Figure 2.10 a). The aim of the study was to optimise the scaffold design to yield highest amount of regenerated bone after 24 weeks and to compare the outcome to the honeycomb titanium scaffold predictions. Therefore,

the same MBBR computer model was used to predict regenerated bone volume, assuming graft osteoconduction and surface-guided ECM deposition in the defect. In addition, the same defect geometry (4-cm segmental defect) and loading conditions were defined as for the titanium scaffold study, and the scaffold was hypothesised to be made of titanium.
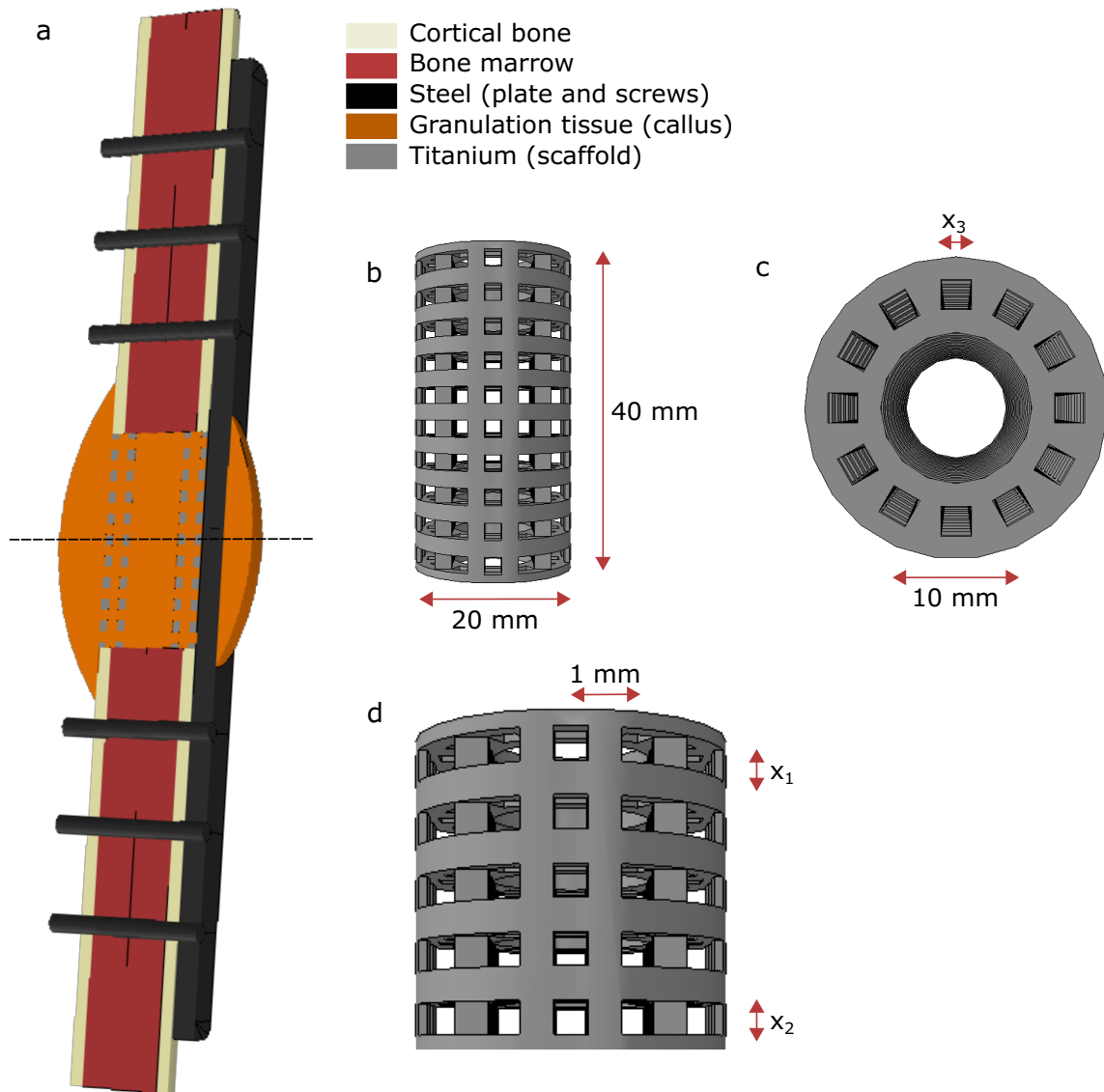
Figure 2.10 – **Cylindrical scaffold set-up for geometrical optimisation**: (a) full geometry set-up with symmetry plane (dotted line); (b) scaffold external dimensions (side view); (c) scaffold dimension and variable definition (x_3, top view); (d) variable definition (x_1-x_2, side view).

The scaffold was designed as a hollow cylinder of outer radius 10 mm and inner radius 5 mm with square-section pores implanted in a 4-cm defect in a sheep tibia (Figure 2.10 b, c). The osteotomy was stabilised with an internal fixation plate and screws made of steel. Due to the symmetry of the set-up, only the upper half was modelled and simulated in the FEA and ABM (Appendix B.2); a symmetry boundary condition was applied on the section about the xy-plane (condition "ZSYMM" in Abaqus). The pores were defined as graded from top to middle slice (bottom of the half model), so that only the bottom and top row pore sizes

were defined as variables (x_1 and x_2, Figure 2.10 d). These pores were obtained by cutting the scaffold geometry in the x and y directions (parallel and orthogonal to the plate) by a repetition of the pores with 4-mm distance. In the vertical direction, 12 pores were defined in a regular circular pattern with a size defined by the variable x_3 (Figure 2.10 c). x_1 and x_2 values were constrained 0.3 and 3.8 mm, and x_3 between 0.3 and 3 mm.

A further optimisation was performed on the exact same geometry but with a much softer material (Young's modulus 0.2 MPa, similar to granulation tissue material properties) to compare the outcome in terms of regenerated bone volume, patterning and optimal scaffold geometry.

Due to the use of poroelastic material properties for the biological tissue parts, the automatic geometry update and meshing led to cases for which the FEA would not run (too small elements). Therefore, a more robust algorithm was implemented to handle such errors and not stop the loop as soon as one design would not run: when an error happened in the FEA, the bone regeneration simulation was stopped and an objective value of 1 (the worst value) was attributed to the tested design. The optimisation loop was then continued to suggest a new design to be tested. In addition, if the optimisation algorithm suggested a new design identical to a previously tested design, the pore size values were slightly perturbed (random values picked within 3 μm from the suggested values) to avoid repeating an already performed simulation.

2.3.4 Initial sampling strategies

2.3.4.1 Uniform sampling

The sampling realised for the cubic scaffold parametric study (Section 2.2.2) was used as an initial sampling set to perform optimisation of the non-graded cubic scaffold with 2 variables. The data-set of 181 points served as a reference to evaluate sampling strategies from the DOE field.

2.3.4.2 Latin hypercube sampling

To limit the amount of initial simulation runs, a smarter sampling strategy called Latin hypercube sampling (LHS) [124] was investigated, based on its implementation in the Matlab kriging toolbox DACE (Design and Analysis of Computer Experiments) [125]. This common sampling method in the DOE field, especially for computer experiments, generates a set of parameter values in a multidimensional space. For a size N, the design space is divided into sub-spaces obtained by dividing each side of the parameter space by N; in 2D, this would be similar to a chess board. Points are then placed (randomly) in various sub-spaces so as to have exactly one point in each row and column (extended to further dimensions). This allows a sampling representing well the variability of the design space.

For the non-graded cubic geometry with 2 variables, different sizes of LHS designs were tested: $N = 10, 20, 40$. The results obtained in the subsequent optimisation process were compared with results obtained based on the uniform sampling. The generic rule of having

$N = 20 * nvars$ was derived from these first results, with $nvars$ the number of variables, and used for other optimisation cases.

2.3.4.3 Material initial sampling

Due to the large variation in orders of magnitude of the tested material properties (from 10 to 10^5 MPa), the LHS technique was applied for values between 0 and 1 that were transformed logarithmically to be translated to the Young's modulus values following the relation $E = 10^{1+4x}$ with E the Young's modulus value in MPa and x the normalised variable used in the sampling step.

2.3.5 Surrogate models

Different surrogate modelling techniques were tested, all implemented in Matlab R2018b (The MathWorks Inc., Massachusetts): neural networks (functions *fitnet* and *train*), radial basis functions (using a specific toolbox for scattered data interpolation and approximation [126]), Gaussian process regression (function *fitrgp*), support vector machines (function *fitrsvm*), multivariate adaptive regression splines (MARS) (ARESLab [127]) and Kriging (Matlab kriging toolbox DACE [125]). Those various surrogate modelling techniques were tested in a preliminary study by assessing the root mean squared error of the predictions made on one data-set by the model built on an independent data-set (Appendix B.1).

As MARS and Kriging obtained the best accuracy results, both techniques were used in the surrogate optimisation. **MARS** is a non-parametric regression technique. In its simplest form, it is the product of hinge functions (functions of the form max(0,x-b) or max(0,b-x)), namely piece-wise linear functions, what makes the resulting surrogate formula easily interpretable. The MARS implementation used here employed piece-wise cubic functions. A MARS model is built through adding terms to reduce the mean squared error the most until a certain tolerance level is reached; and then removing the terms that are least value-adding in the model to avoid over-fitting.

Kriging is a type of Gaussian process regression that was first developed for gold mining in South Africa. The underlying idea is to compute a weighted average of known points around the point of interest. The definition of those weights is based on assumptions made on the co-variances. Originally, this regression method was intended to predict realisations of a random field; nowadays, it is also more and more used as a black-box model to interpolate data from computer simulations [128]. Different types of auto-correlation can be defined when applying Kriging to a data-set; most accurate predictions were obtained assuming an exponential auto-correlation. Other model parameters were left as default as they seemed to be performing best.

2.3.6 Optimisation algorithms

Based on preliminary studies (Bahar Rahmani's master thesis [129]) and due to the fact that the objective function was derived from stochastic simulations and had several local optima, gradient-free global optimisation approaches were employed rather than gradient-based optimisation approaches. The following algorithms implemented in Matlab Global

Optimisation Toolbox were tested: direct search (function *patternsearch*), genetic algorithm (function *ga*) and particle swarm optimisation (function *pso*) [130]. Such algorithms have a higher computational cost than gradient-based algorithms; however, they were applied to the surrogate function, much faster to evaluate than the bone regeneration simulation. Each algorithm will be briefly described in the next paragraphs.

The **direct search** algorithm tests at each iteration a set of points (the *mesh*) around the current best point, obtained by adding a scalar value multiplying a set of vectors (the *pattern*). The new best point in the neighbourhood becomes the next starting point. This algorithm can accommodate non-linear and linear constraints and needs an initial point to start the search process. Its convergence to a local optimum is proved but it may get stuck in one basin of attraction and thus miss the global optimum.

The genetic algorithm (GA) and the particle swarm optimisation (PSO) are both stochastic optimisation processes, whose convergence is therefore not proved in the general case and whose performance may vary at each run. The **genetic algorithm** is based on the natural selection processes observed in nature. It has a population of points for which the objective is evaluated. This population is improved generation after generation thanks to *selection* (best individuals will contribute to the next generation), *crossover* (child points obtained from parent points) and *mutation* (random changes) rules. The population evolves and converges towards a (generally global) optimum over time.

Particle swarm optimisation is also a population-based algorithm inspired by bird flocks or swarming insects, where a collection of particles moves through the variable space. The objective function is evaluated for the whole population; based on the results, velocity vectors are defined for each particle that is then moved towards a new position. The population usually converges around one or a few optimal positions over time.

2.3.7 Summary of optimisation cases

A summary of all optimisation cases with objective, constraint and variable definitions and surrogate model and optimisation algorithm choices is given in Tables 2.9 (cube geometrical optimisation), 2.10 (cube material optimisation) and 2.11 (cylinder optimisation). Lower and upper bounds for the pore sizes or the material properties are not given in the tables as they were applied in all cases as described in the problem definitions (Section 2.3.3). The initial sampling is described with the technique name (uniform or LHS) and the number of points in parentheses.

For the cubic scaffold geometrical optimisation, cases 1-4 served as evaluation of the initial sampling technique; cases 5-7 and 8-10 (performed with two different initial data-sets) served to assess optimisation algorithm, surrogate models and influence of the initial data-set. Cases 11-12 and 16 evaluated the use of another surrogate model (MARS instead of Kriging) in the surrogate optimisation process. When the direct search optimisation algorithm was employed, the starting point was defined arbitrarily with all horizontal pores of size 0.5 mm and the vertical pores of size 0.7 mm.

Case	Number of variables	Constraint	Initial sampling	Surrogate model	Optimisation algorithm	Loading
1	2	$P > 50\%$	Uniform (181)	Kriging	GA	Compression
2	2	$P > 50\%$	LHS (10)	Kriging	GA	Compression
3	2	$P > 50\%$	LHS (20)	Kriging	GA	Compression
4	2	$P > 50\%$	LHS (40)	Kriging	GA	Compression
5	4	$P > 50\%$	LHS (80)	Kriging	GA	Compression
6	4	-	LHS (80)	Kriging	PSO	Compression
7	4	$P > 50\%$	LHS (80)	Kriging	direct search	Compression
8	4	$P > 50\%$	LHS (80)	Kriging	GA	Compression + bending
9	4	-	LHS (80)	Kriging	PSO	Compression + bending
10	4	$P > 50\%$	LHS (80)	Kriging	direct search	Compression + bending
11	4	-	LHS (80)	MARS	PSO	Compression + bending
12	4	$P > 50\%$	LHS (80)	MARS	direct search	Compression + bending
13	7	$P > 50\%$	LHS (140)	Kriging	GA	Compression + bending
14	7	-	LHS (140)	Kriging	PSO	Compression + bending
15	7	$P > 50\%$	LHS (140)	Kriging	direct search	Compression + bending
16	7	-	LHS (140)	MARS	PSO	Compression + bending

Table 2.9 – Cube geometrical optimisation cases – P denotes the porosity

For the cubic material optimisation, a comparison was only made between the 3 optimisation algorithms (direct search, GA, PSO) (Table 2.10). For the direct search, the starting point of the algorithm was defined as $[100, 10000, 100, 10000]$ MPa.

Case	Surrogate model	Optimisation algorithm	Loading
17	Kriging	direct search	Compression
18	Kriging	GA	Compression
19	Kriging	PSO	Compression

Table 2.10 – Cube material optimisation cases
– all cases used an initial sampling defined by LHS with 80 samples.

For the cylinder optimisation, two different material properties were assumed for the scaffold: titanium with Young's modulus 104 GPa and a very soft, granulation-tissue-like material with Young's modulus 0.2 MPa. The 3 optimisation algorithms (direct search, GA, PSO) were compared for their performance in finding the optimum design (Table 2.11). For the direct search optimisation, the starting point was defined arbitrarily with horizontal pores of size 2.05 mm and the vertical pores of size 1.65 mm.

Case	Scaffold material	Surrogate model	Optimisation algorithm
1	Titanium	Kriging	Direct search
2	Titanium	Kriging	GA
3	Titanium	Kriging	PSO
4	Soft	Kriging	Direct search
5	Soft	Kriging	GA
6	Soft	Kriging	PSO

Table 2.11 – Cylinder optimisation cases
– Titanium refers to a scaffold material with Young's modulus 104 GPa, whereas Soft refers to a scaffold material with Young's modulus 0.2 MPa (similar to granulation tissue); all cases used an initial sampling defined by LHS with 60 samples.

<div style="text-align: right; font-size: 4em; color: #888;">3</div>

In silico investigation of scaffold-supported bone regeneration

3.1 *In silico* model of fracture healing cannot explain bone regeneration within scaffolds

Computer models that have been able to explain bone regeneration in uneventful bone healing scenarios (when the bone repair is successful) [33, 49], were not able to explain tissue distribution and regeneration dynamics during any of the two scaffold-supported regeneration experiments investigated (with titanium and PCL scaffolds) (Figures 3.1, 3.4 a). In addition, the model was also not able to account for tissue patterning in an empty large bone defect (Figure 3.4 b). In all 3 cases, much more bone was predicted at the observation time points (Figures 3.2, 3.3, 3.5 and 3.6) 24 weeks post-surgery for the titanium scaffolds, 3 and 12 months post-surgery for the PCL scaffold and 3 months post-surgery for the empty defect, and followed a different pattern than *in vivo*.

For the titanium scaffolds, bone was observed to closely follow the scaffold pores *in vivo* [13], while the baseline fracture healing computer model predicted a homogeneous bone distribution in the whole callus, and a large callus formation (Figure 3.1). In addition, the *in silico* model predicted remodelling already after ca. 20 weeks for the soft scaffold, what did not happen *in vivo*. Quantification further confirmed the over-estimation of bone formation by the computer model compared to the *in vivo* data (Figures 3.2: case 1, Figure 3.3: case 13). Cartilage quantification in the total region of interest fell within the experimental range, but towards its lower value, with 0.7% compared to 0.3-4.2% for the soft scaffold; and 0.1% compared to 0-1.1% for the stiff scaffold.

Differences between *in silico* predictions and *in vivo* data were even more pronounced for the PCL scaffold: while bridging was only partial after 12 months experimentally, the computer model predicted healing after ca. 4 months (Figure 3.4 a). Again, quantification further confirmed a considerable over-estimation of bone volumes (Figure 3.5). The simulation

<div style="text-align: center;">43</div>
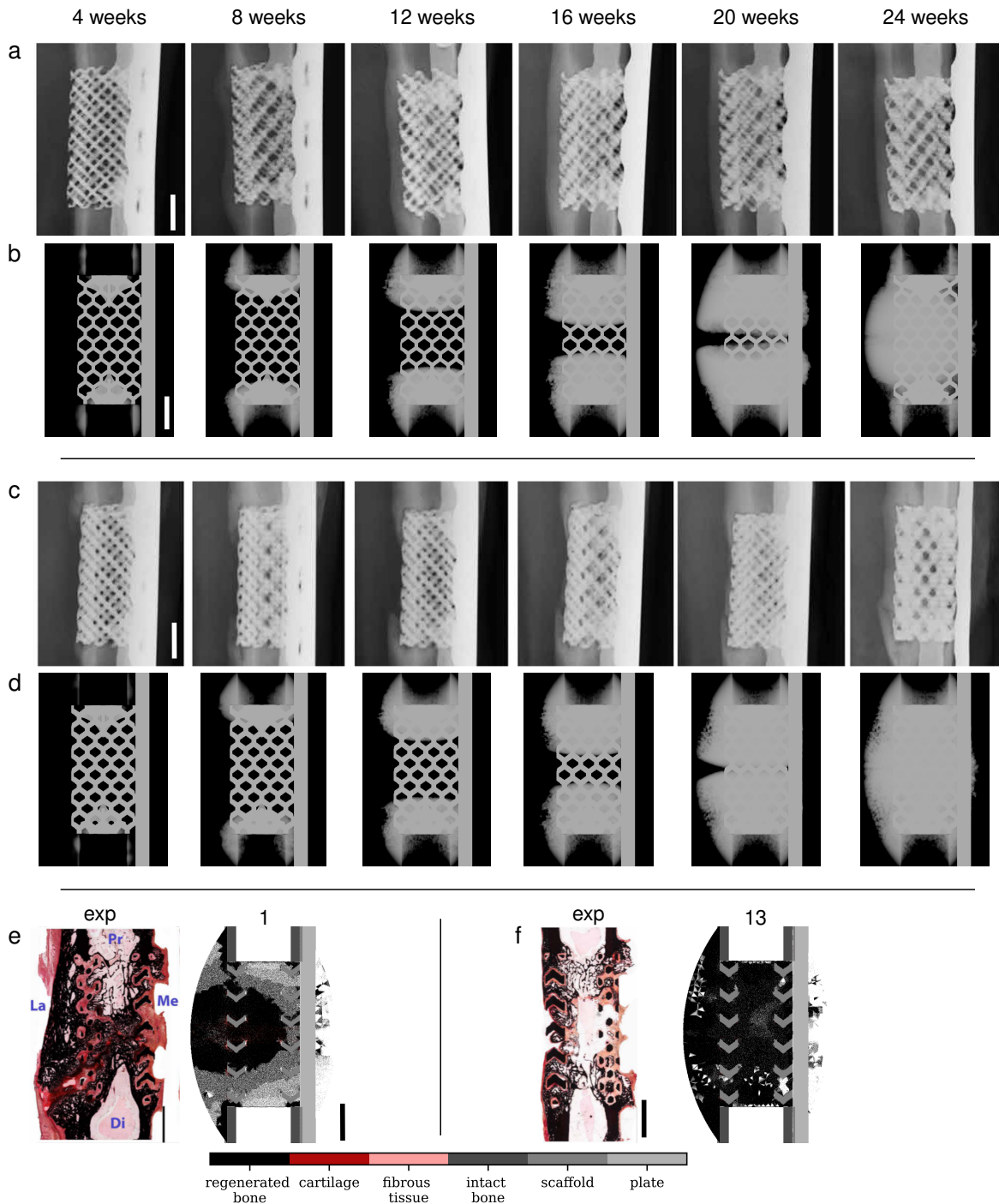
Figure 3.1 – Titanium scaffolds – experiment and baseline simulation: (a-d) X-ray pictures for (a) soft titanium scaffold, experiment; (b) soft titanium scaffold, baseline simulation (1); (c) stiff titanium scaffold, experiment; (d) stiff titanium scaffold, baseline simulation (13); (e-f) 24-week experimental (exp) and baseline simulated histology for (e) the soft titanium scaffold (simulation case 1) and (f) the stiff titanium scaffold (simulation case 13). Scale bars represent 10 mm; the colour legend for the histology is given below; La, Me, Pr and Di indicate lateral, medial, proximal and distal sides, respectively. Experimental images (a, c, e, f) from [13]. Reprinted with permission from AAAS.
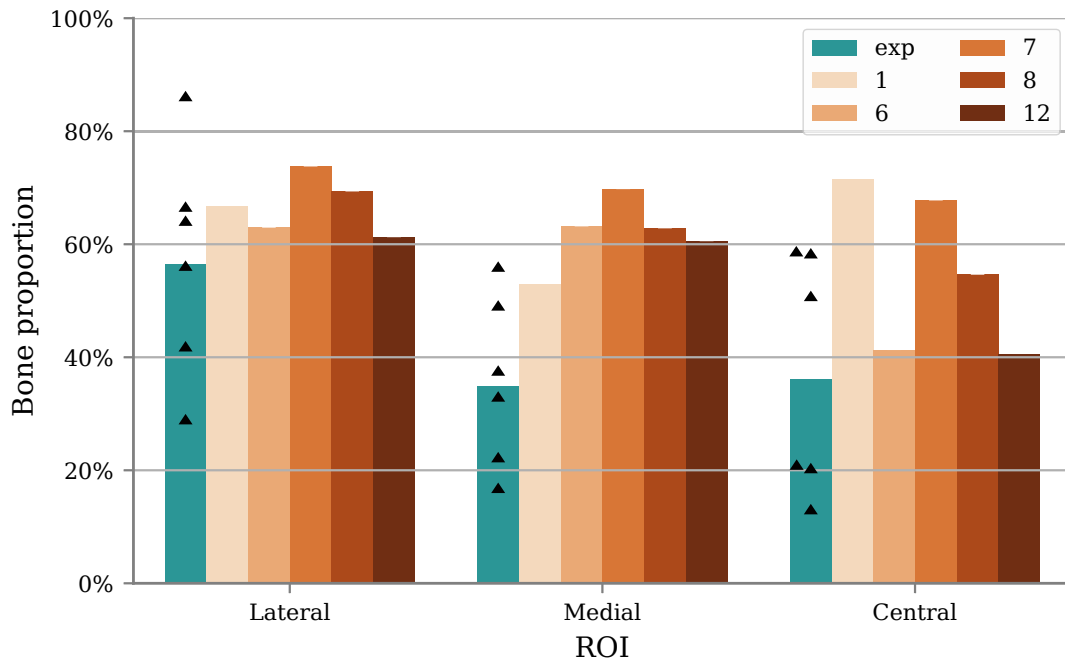
Figure 3.2 – **Soft titanium scaffold set-up** – **quantification**: experimental average and detailed data (triangles) and simulation quantification for lateral, medial, central ROIs. Simulation codes were defined in Table 2.6: (1) baseline; (6) combined osteoconduction and osteoinduction; (7) graft-contained MSCs; (8) combined graft-contained MSCs with osteoconduction and osteoinduction; (12) surface-guided ECM deposition with bone graft osteoconduction.
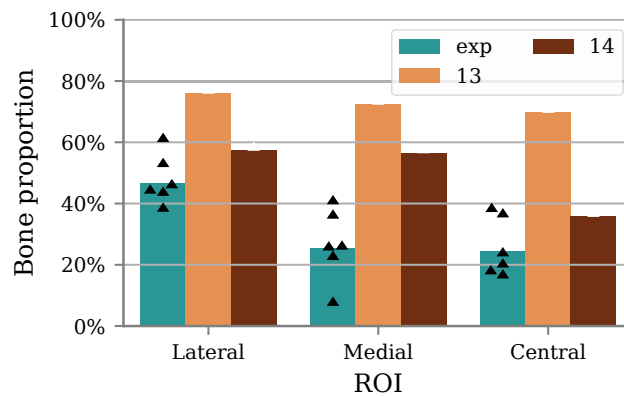
Figure 3.3 – **Stiff titanium scaffold set-up** – **quantification**: experimental average and detailed data (triangles) and simulation quantification for lateral, medial, central ROIs. Simulation codes were defined in Table 2.6: (13) baseline; (14) surface-guided ECM deposition with bone graft osteoconduction.
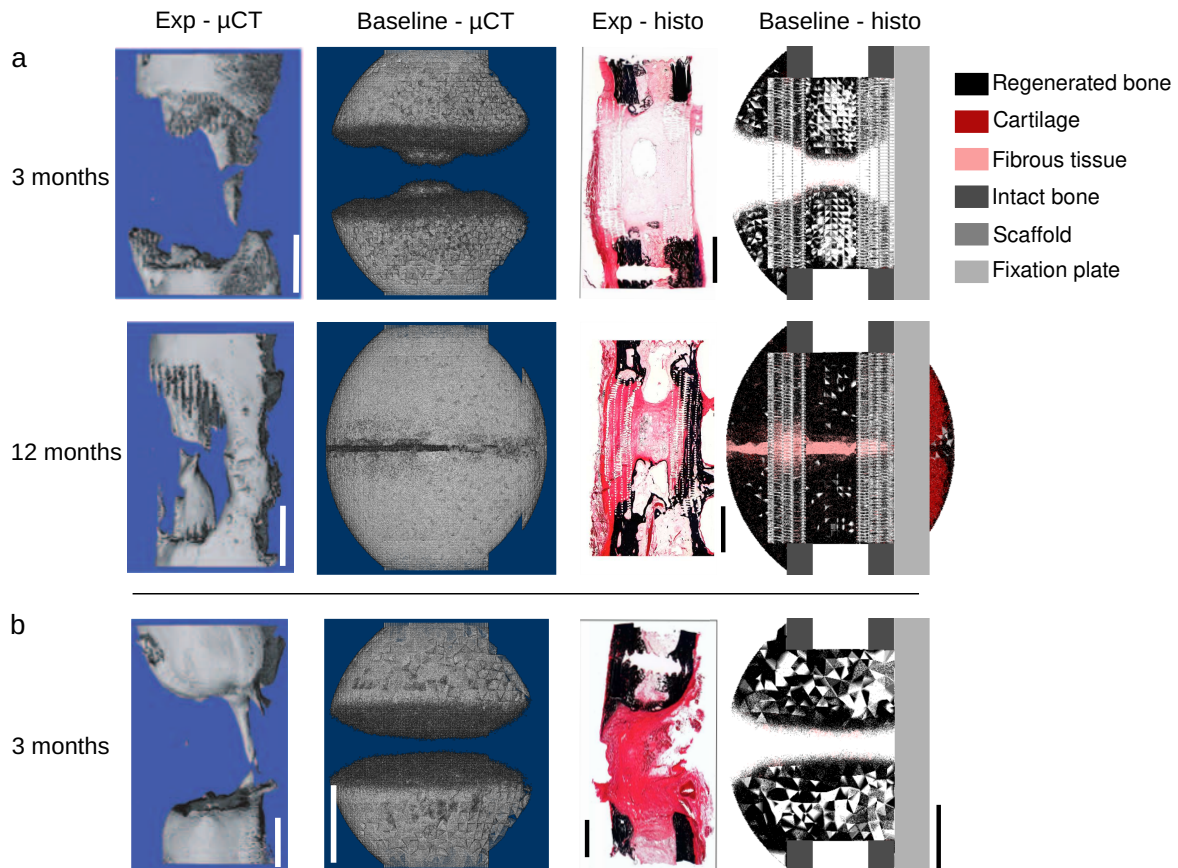
Figure 3.4 – PCL scaffold and empty defect experiment and baseline simulation:
experiment and baseline simulation µCT and histology for (a) the PCL scaffold set-up, 3 and 12
months post-surgery; (b) the empty defect, 3 months post-surgery. Scale bars represent 10 mm;
the colour legend for the histology is given on the right. Experimental images from [9]. Reprinted
with permission from AAAS.

quantification for the PCL scaffold was actually even higher than the experimental data
obtained with the addition of growth factors [9], suggesting that the baseline model would in
reality correspond to a biologically highly stimulated case. Similar conclusions could be drawn
when using the baseline simulation set-up for the empty defect (Figures 3.4 b, 3.6), where a
complete bridging and large amounts of bone were predicted, what did not reproduce the
experimentally observed non-unions. In fact, this rather corresponded to a further experimental
case with autologous bone grafting [9].

Figure 3.5 – **PCL scaffold set-up** – **quantification**: experimental average and detailed data (triangles) and simulation quantification for total, inner duct, scaffold walls ROIs
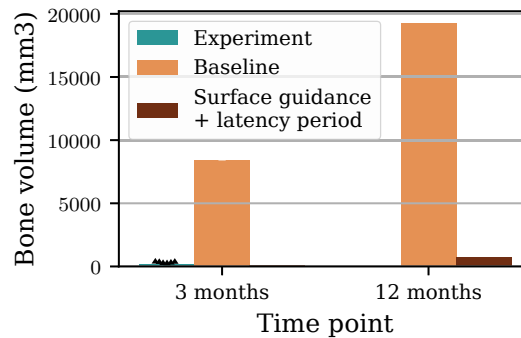
Figure 3.6 – **Empty defect set-up** – **quantification**: experimental average and detailed data (triangles) and simulation quantification for total ROI

3.2 Large bone defect and scaffold-supported regeneration can be explained by alterations in biological activity

Experimentally, large bone defects have been shown not to heal spontaneously [1, 74], or to have a very reduced healing capacity in the presence of a specific scaffold [9]. However, fracture healing computer models predict defect bridging (with or without a scaffold); therefore, computer model modifications were investigated to account for a lack of biological stimulation, on the one hand, and biological stimulating effects (e.g. due to graft or specific biomaterial presence), on the other.

3.2.1 A systematic analysis of the influence of cellular activity on predicted bone regeneration within PCL scaffolds

As the PCL scaffold experimental set-up did not include any biological stimulation, it was used to link cellular activity alterations to the observed impaired healing by performing a systematic analysis of cellular activity (Table 2.5). The cell activity rate parametric study (together with surface-guided ECM deposition) revealed the MSC differentiation rate to have the highest impact on the predicted longer-term outcome (12 months post-surgery). Indeed, simulation cases 3, 5, 7, 8 (all cases implementing a lower MSC differentiation rate) showed marked lower regenerated bone volumes (Figure 3.7). The cell migration speed increase resulted in a slightly faster healing process whose effect would however be negligible after 12 months: bone volumes were for instance higher for simulation case 2 compared to 1 (where only migration speed was altered), and 6 compared to 4 (combined with a lower proliferation) 3 months post-surgery. Combined proliferation and differentiation rate reduction also affected the bone regeneration outcome as can be seen by comparing case 7 (lower differentiation and proliferation rates) to case 1 (baseline levels), both 3 and 12 months post-surgery. This preliminary study emphasised the predominant effect of cell proliferation and differentiation activity levels in the regeneration process.
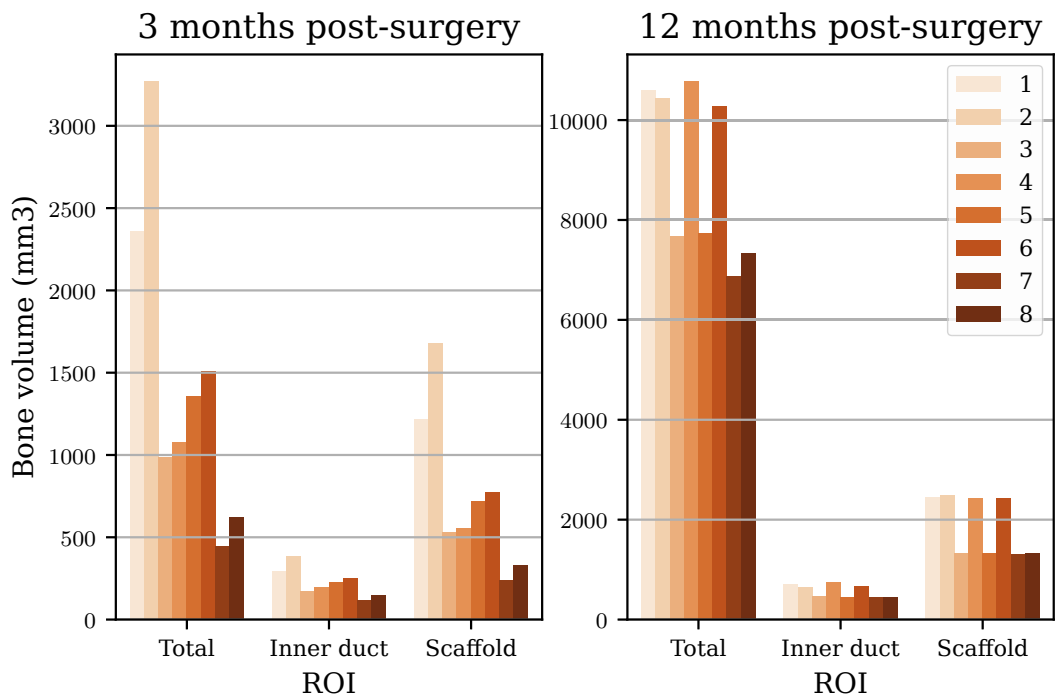
Figure 3.7 – **PCL scaffold cell activity sensitivity analysis**: simulation bone volume quantification in total, inner duct and scaffold ROIs at 3 and 12 months post-surgery for cases: (1) baseline activity levels; (2) higher migration speed; (3) lower differentiation; (4) lower proliferation; (5) higher migration, lower differentiation; (6) higher migration, lower proliferation; (7) lower differentiation and proliferation; (8) higher migration, lower differentiation and proliferation.

3.2.2 Altered biological activity in the empty and PCL scaffold defects

Based on the cell activity analysis (Section 3.2.1), the empty defect was simulated with strongly reduced cell proliferation and differentiation rates (divided by 5) after a latency period of 15 days, in addition to surface-guided migration and ECM deposition. This simulation set-up yielded a good agreement with experimental observations, qualitatively (Figure 3.8 b) and quantitatively (Figures 3.6). Very low amounts of regenerated bone were predicted and followed the intact bone extremities, as observed experimentally on the distal side; however, no bone marrow capping was predicted as seen experimentally on the proximal side (Figure 3.4 b).

For the defect complemented with the PCL scaffold, cell proliferation and differentiation rates were only slightly reduced (divided by 2) to account for the positive effect of the ceramic (TCP) contained in the scaffold material. Also in that case, the simulation set-up yielded a good agreement with experimental observations, both qualitatively (Figure 3.8 a) and quantitatively (Figures 3.5). Bone volume quantification in the various ROIs was in good agreement with the experimental data (Figure 3.5), and mineralised cone formation was predicted in the scaffold pores and inner duct as reported *in vivo* [72] (Figures 3.4 a and 3.8 a).
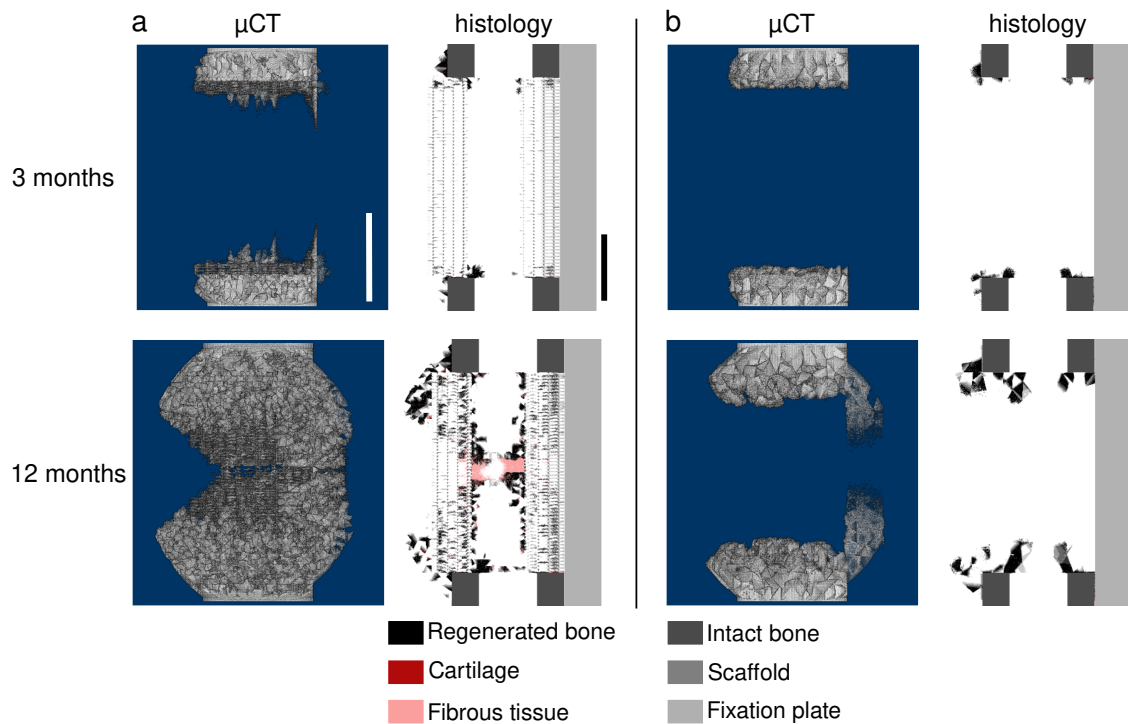
Figure 3.8 – PCL scaffold and empty defect set-ups – complemented simulation: simulated µCT and histology 3 and 12 months post-surgery for (a) the PCL scaffold set-up and (b) the empty defect. Surface-guided cell migration and tissue deposition is assumed in both cases; impaired cell activity levels are assumed in the empty defect and stimulation by the tricalcium phosphate present in the scaffold for the PCL scaffold case. Scale bars represent 10 mm; the colour legend is given below.

3.2.3 Graft stimulating effects in the titanium scaffold set-up

A hypothetical non-stimulated titanium scaffold experiment (without any graft addition in the scaffold pores) was simulated in simulation case no. 2 with a lack of MSC migration

and proliferation after a latency period of 15 days. It resulted in a non-union after 24 weeks with bone marrow capping (Figure 3.9 (2)), as observed experimentally in large bone defect non-unions [74].
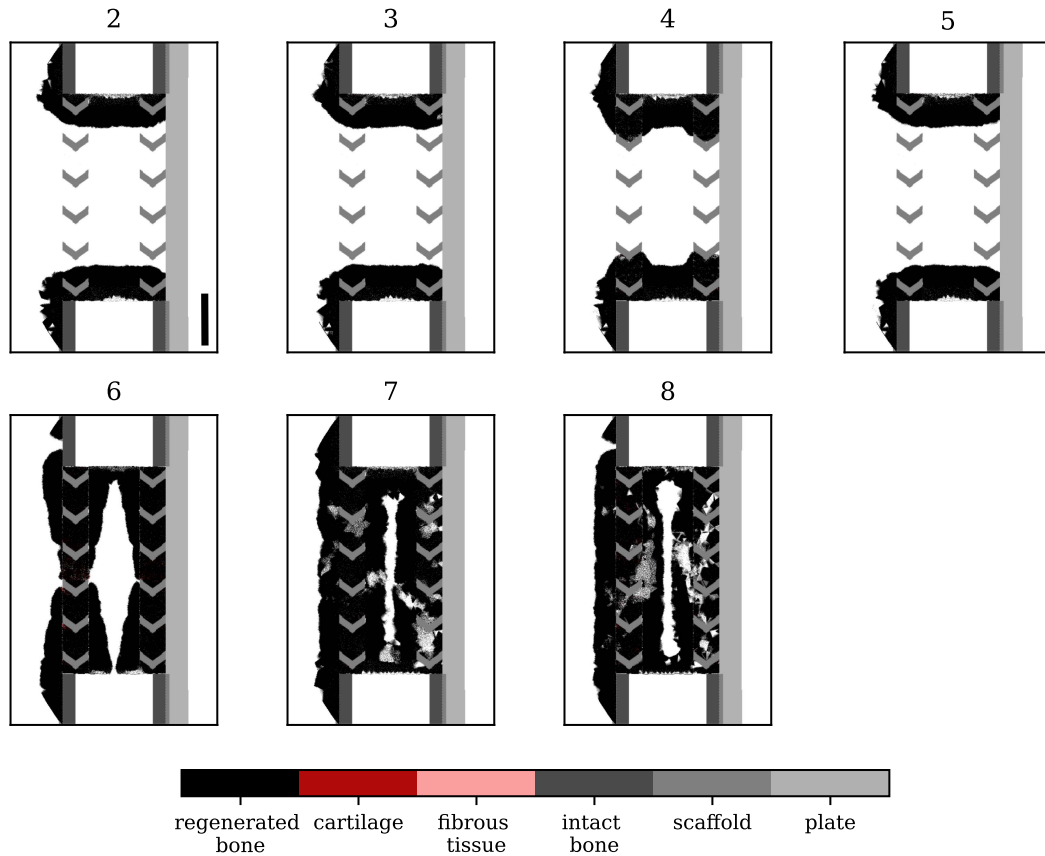
Figure 3.9 – **Titanium scaffold set-up** – **alterations in biological activity**: 24-week simulated histology for (2) non-stimulated regeneration; (3) graft stimulation on cell migration; (4) graft stimulation on cell proliferation; (5) graft stimulation on cell differentiation; (6) combined osteoconduction and osteoinduction; (7) bone graft-contained MSCs; (8) combined bone graft-contained MSCs with osteoconduction and osteoinduction (Table 2.6). The scale bar represents 10 mm; the colour legend is given below.

The addition of graft in the titanium scaffold experiments was hypothesised to generate biological stimulation *via* various mechanisms: stimulation of the MSC migration, proliferation or differentiation and initial presence of MSCs contributing to the regeneration process.

Graft stimulation on MSC migration (case 3) or differentiation (case 5) alone did not have any effect on the healing outcome compared to the non-stimulated regeneration (case 2) (Figure 3.9). Due to their diminished proliferation capacity, MSCs were not present anywhere else than close to the intact bone ends, and did thus not lead to osteoblast differentiation and bone formation. Graft stimulation on MSC proliferation (case 4) showed a slightly increased bone formation after 24 weeks in the scaffold pores, but was still far from a complete bridging. When combining all graft stimulation effects together (case 6), the healing process led to a complete bridging in ca. 20 weeks with regenerated bone following more closely the scaffold pores (containing graft), similar to experimental observations. The resulting bone

quantification of the mid-sagittal plane was within the experimental range for the lateral and central ROIs (Figure 3.2).

The addition of MSCs (both alone and in combination with the graft osteoconductive effects, Figure 3.9: cases 7 and 8) led to a final bone distribution that was also in good agreement with the experiments, in particular with a bone marrow cavity opening through the middle of the defect and a lateral/medial difference in quantification as observed *in vivo* (Figure 3.2: case 8). However, bridging was complete after ca. 10 weeks due to a very fast and homogeneous bone deposition from the MSCs present in the graft. This did not reproduce experimental observations where bone regeneration started from the intact bone extremities and was not homogeneous throughout the defect (Figure 3.1 a).

3.3 Scaffold surface guidance can explain tissue patterning in large bone defects supported or not by a scaffold

To account for the experimental observations that scaffold surfaces act as templates for bone in-growth, two different surface guidance features were investigated: surface-guided MSC migration and surface-guided ECM deposition.

Surface-guided MSC migration considerably slowed down the healing process for the titanium scaffold. In the non-stimulated simulation (Figure 3.10: case 9), the healing extent was even smaller than for the non-stimulated case without surface-guided cell migration (Figure 3.9: case 5). More importantly, even when combined with graft osteoconduction (Figure 3.10: case 10), the defect was still far from bridged after 24 weeks. Surface-guided migration thus represented a very strong healing hindrance for the titanium scaffold set-up. This indicated that surface-guided MSC migration was likely not the driving guidance process in this set-up.

Surface-guided ECM deposition led to a better agreement with experimental data. Case 12 (Figure 3.10 a: case 12 and c) represented the surface-guided ECM deposition combined with graft osteoconduction and showed a healing dynamics similar to the graft stimulation (Figure 3.9: case 6), but with bone being further confined into the scaffold walls; quantification was also in good agreement with the experimental data (Figure 3.2). However, when using the same simulation set-up for the stiff titanium scaffold (Figure 3.10 b and d), the predicted healing process was very similar to the soft scaffold, and failed to reproduce the impaired healing observed *in vivo*, namely a delayed union or non-union, and reduced bone proportions in the quantified ROIs (Figure 3.3) [13].

For the PCL scaffold set-up, both surface-guided MSC migration and ECM deposition were implemented, leading to a good agreement with experimental data in terms of bone regeneration dynamics and patterning (Figure 3.8). In particular, the surface-guided migration allowed a similar simulation set-up to also reproduce the empty defect non-union, with migration being largely impaired in the absence of scaffold surfaces (Figure 3.8 b). In addition, bone growth onto the plate could be reproduced for both the empty defect (12 months post-surgery in the *in silico* prediction and already 3 months post-surgery *in vivo*) and the defect complemented with the scaffold (Figure 3.8), as seen *in vivo* (Figure 3.4).
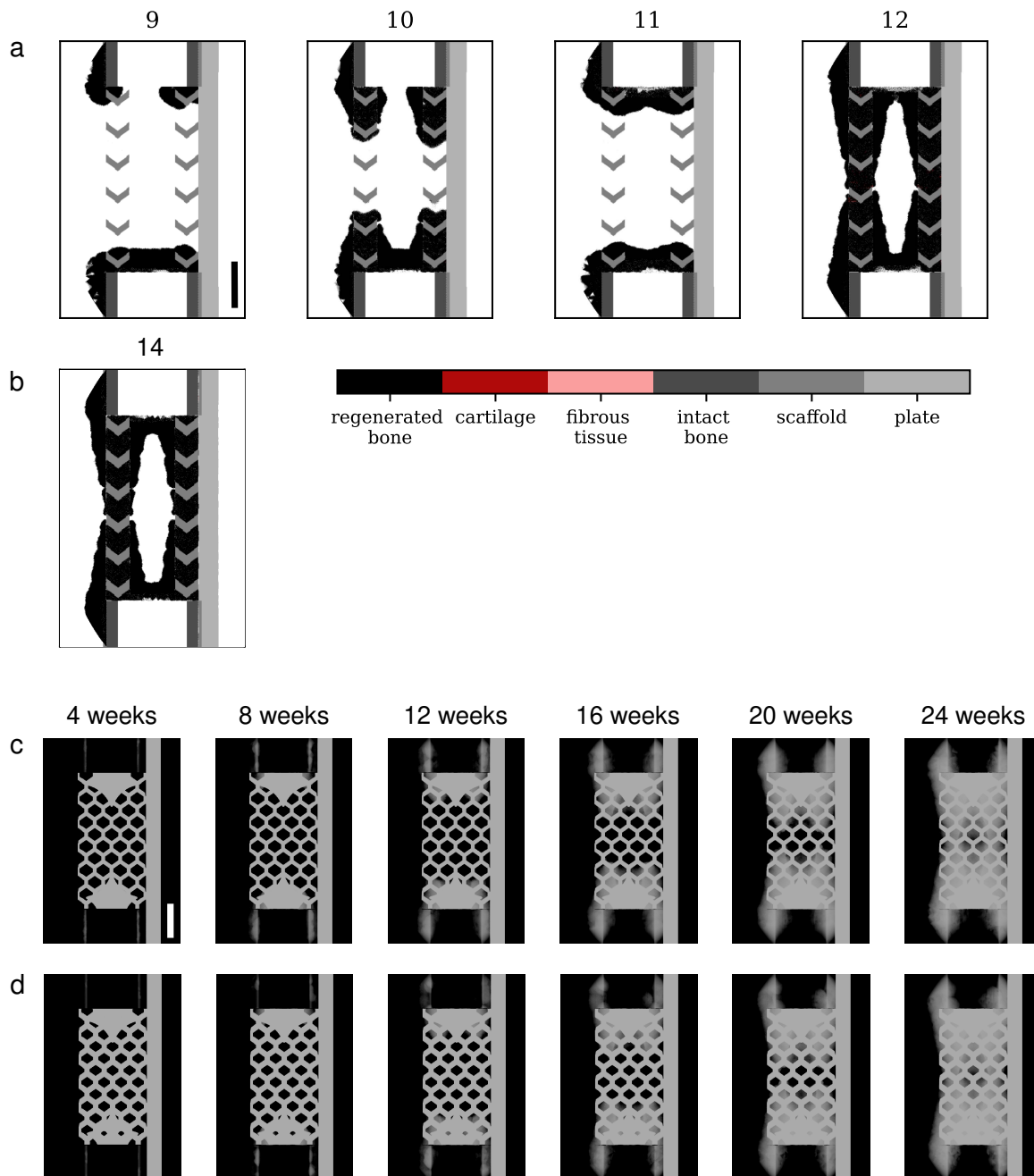
Figure 3.10 – Titanium scaffold set-up – effect of surface guidance: 24-week simulated histology for (a) the soft titanium scaffold: (9) surface-guided migration; (10) surface-guided migration with bone graft osteoconduction; (11) surface-guided ECM deposition; (12) surface-guided ECM deposition with bone graft osteoconduction; (b) stiff titanium scaffold: (14) surface-guided ECM deposition with bone graft osteoconduction (Table 2.6). Simulated X-ray for (c) the soft titanium scaffold (simulation case 12) and (d) the stiff titanium scaffold (simulation case 14). Scale bars represent 10 mm; the colour legend is given next to b.

3.4 An application: cell-based therapeutic strategies

The presented computer model for scaffold-supported bone regeneration was further used to investigate the mechanisms behind healing under a specific therapeutic strategy, the initial seeding of MSCs in the implanted PCL scaffold [9] (Figure 3.11 d). The effect on the regeneration process and outcome of initially seeding different numbers of MSCs (100, 10 000 and 1 million cells) randomly distributed in the scaffold pores was studied.
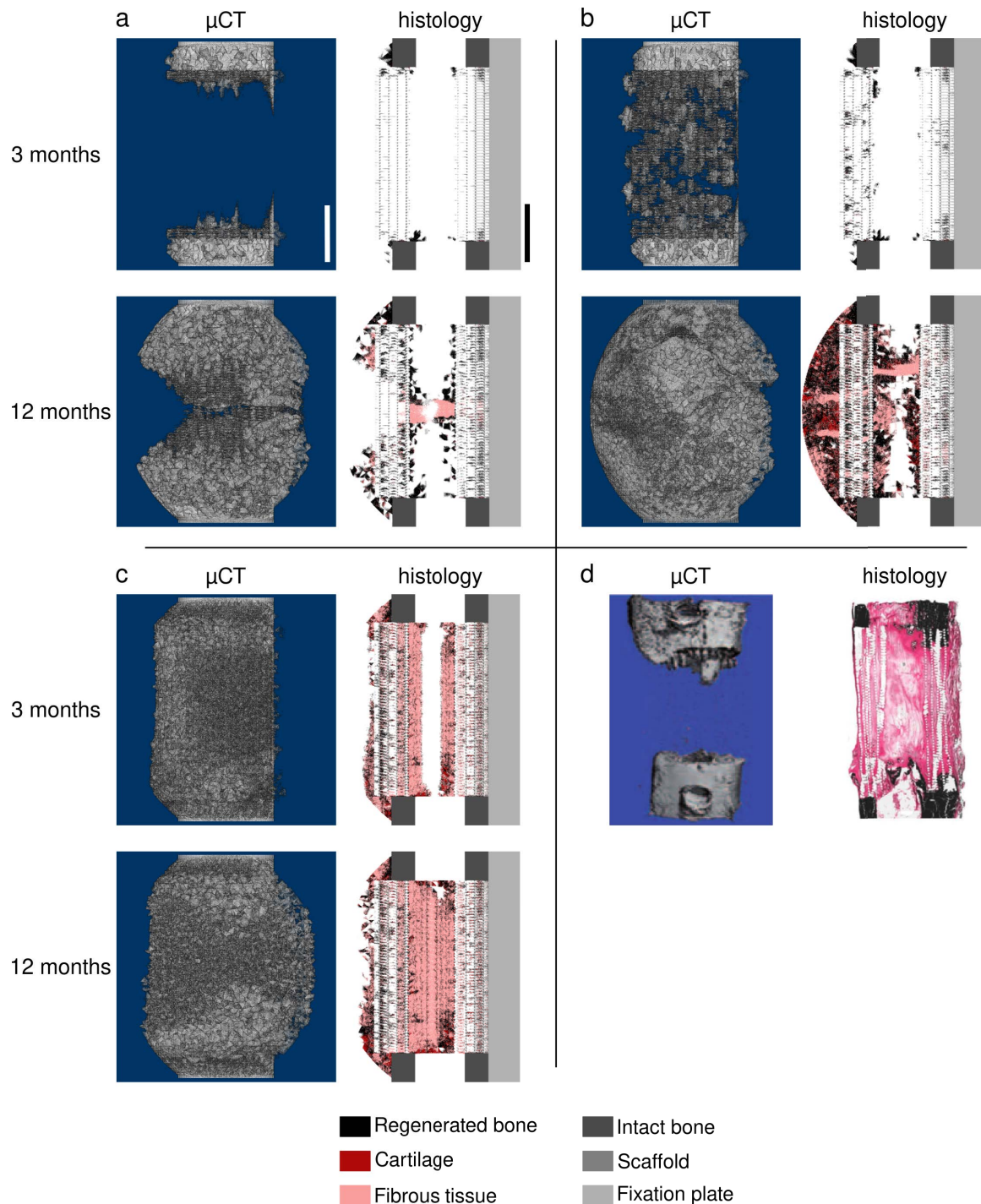
Figure 3.11 – MSC-seeded PCL scaffold outcome: µCT and histology-like images 3 and 12 months post-surgery: (a) 100 cells; (b) 10 000 cells; (c) 1 million cells; (d) experimental data from [9]; reprinted with permission from AAAS. The scale bars represent 10 mm.

When seeding initially 100 MSCs, the regeneration process was the same as without any cells, and the outcome 3 and 12 months post-surgery (Figures 3.11 a, 3.12) was similar to the prediction with the scaffold alone. However, when seeding 10 000 MSCs in the scaffold pores initially, they were shown to contribute to the healing already 3 months post-surgery; large amounts of bone were predicted in the whole callus (Figure 3.11 b). Lastly, the case with 1 million initially seeded MSCs led to an even more complete bone healing already 3 months post-surgery, but no marked difference 12 months post-surgery (Figures 3.11 c, 3.12). The reason for that seemed to be the faster and more homogeneous tissue growth at the beginning of the healing process, leading to a stiffer overall construct; therefore, the surrounding callus was not favouring any tissue deposition because the stiff environment mostly led to a resorption stimulus. Bone thus followed the intact bone geometries instead of forming in the peripheral callus. A direct comparison to the experimental data was difficult as the number of seeded cells in the computer model could not directly be related to a physiological cell number; indeed, the implementation of lattice points that are larger than the typical MSC size meant that one lattice point could contain many MSCs. Nevertheless, experimentally the addition of MSCs did not show any effect compared to the defect with a PCL scaffold alone (Figure 3.11 d); this observation compares best with the case with the lower number of seeded MSCs (100 cells, Figure 3.11 a).
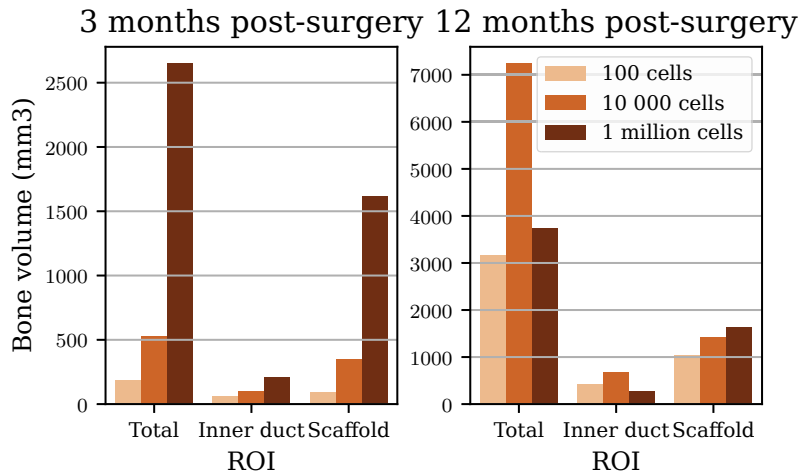
Figure 3.12 – **MSC-seeded PCL scaffold bone regeneration quantification** 3 and 12 months post-surgery

3.5   Discussion

3D-printed scaffolds have been suggested as a promising treatment alternative for large bone defects in various pre-clinical studies [7–15]. However, how exactly they interact with the regenerating tissue has not been elucidated yet. This work aimed at using computer models for bone regeneration to reveal specific features of scaffold-supported large bone defect regeneration. The simulation results suggest that previously validated fracture healing models could not account for scaffold-supported large bone defect regeneration; in fact, a general biological activity reduction in large defects and scaffold surfaces acting as templates for

cellular migration and new ECM deposition could explain scaffold-supported large bone defect regeneration.

Previously, some computer models have been used to predict bone regeneration within scaffolds [51, 67, 70]. However, these models have been developed and validated for uneventful bone fracture healing and further used to predict bone regeneration in different scaffold designs. Only a few *in silico* studies of scaffold-supported bone regeneration were – at least partially – validated against experimental data. Schmitt *et al.* performed a diffusion-based simulation with a principal stress mechanobiological stimulus to predict bone regeneration in a mandible defect supported by a porous titanium scaffold. They obtained good correlation with experimental bone patterning but only considered MSCs and ossification in a 2D set-up, thus not taking into account other tissues (cartilage, fibrous tissue) and the actual 3D geometry of the defect and scaffold [71]. Paris and colleagues used a curvature-based computer model to predict soft and mineralised tissue formation in the same PCL scaffold as studied here [72]. They could reproduce experimental tissue patterning at the pore scale; however, their model did not describe any interaction between tissue regeneration and mechanics and the effect of the scaffold material properties. Liu *et al.* also had a micro-scale focus by restricting their study to one representative unit cell in a rat scaffold instead of the full defect configuration [68]. Nasello and colleagues investigated a femoral condyle defect regeneration, i.e. a different geometry and context than segmental defects; they found the mechanoresponse of bone regeneration to be dependent on location in the body and individual animal variations [131]. Therefore, the studies presented here are the first that predict bone regeneration in (3D) large bone defects complemented with scaffolds, validated against experimental data and including the various phenotypes taking part in the bone regeneration process.

3.5.1 Large bone defect biological activity

The MBBR computer simulations revealed a first aspect not specific to scaffold-supported regeneration but applicable to large bone defects in general, where lower cell activity levels should be assumed compared to uneventful fracture healing. Experimentally, it is well known that such defects do not heal spontaneously and that the healing situation stops evolving after a few months, suggesting strongly impaired cellular behaviour; they result in non-unions with a capping of the bone marrow cavity by regenerated bone [1, 74].

In the simulations, an approach previously described [54] was used where a latency period of 15 days was implemented after which some or all of the cell activities (migration, proliferation, differentiation) were strongly impaired or completely stopped. This assumption was made to reproduce the lack of biological stimulation observed *in vivo*, that may be caused by e.g. a lack of growth factors or an impaired re-vascularisation. Because the titanium scaffold experiments did not include any non-stimulated case (ABG was added in the scaffold pores), it was difficult to use these experimental data to validate the approach; however, the empty 3-cm defect could validate this approach, both qualitatively and quantitatively. Interestingly, when using the baseline MBBR simulation in the empty defect (without a scaffold), regeneration was comparable or even better than observed experimentally with ABG stimulation; similarly, the PCL scaffold baseline simulation showed a better agreement with experimental BMP-7

stimulated cases than with the scaffold alone [9]. These two observations suggest that cell activity rates used in fracture healing computer models reflect biologically stimulated situations in large bone defects.

The computer model predictions suggest that the large defect impaired biological activity could be partially restored to an intermediate level when implanting the PCL-TCP scaffold, likely due to its ceramic content that is thought to enhance proliferation [115, 116] and differentiation [117, 118]. In the computer model, this was implemented with intermediate proliferation and differentiation rates between the empty scaffold non-stimulated case and the baseline fracture healing scenario. This combination resulted in predictions in good agreement with the experimental observations, both qualitatively and quantitatively. No computer simulation so far modelled the effect of a specific scaffold material on the bone regeneration process and cellular activity levels.

In the case of the titanium scaffold, the presence of ABG had a strong effect on the regeneration process, as ABG alone has been previously shown to be sufficient to regenerate a large bone defect [9]. However, the exact graft composition and the way it interacts with bone regeneration remain unclear [3]. Different hypotheses were tested, among which the graft osteoconductive properties, i.e. its necessary presence for cell proliferation and migration to happen at "high" levels, seemed key in reproducing experimental observations. Similar properties have been previously studied in a computer model where they were modelled by an enhanced cell adhesion efficiency [51].

Although bone grafts are usually assumed to contain MSCs and/or osteoblasts that might take part in the regeneration process [3], the simulation predictions suggest that they likely have a very limited contribution. Indeed, if there were many active MSCs in the graft, the predicted bone regeneration would have been faster and happening in a more homogeneous way throughout the defect than seen experimentally. When focusing on the effect of initially seeded MSCs in the PCL scaffold set-up, too low numbers of (active) MSCs were found to have no effect on the regeneration process; in this set-up, a number of approximately 10 000 seemed to be the minimum to have a visible impact on the regeneration, leading to a faster and larger bone formation. However, it should be kept in mind that the "cells" implemented in the *in silico* model do not correspond to individual cells, but rather to a certain number of cells with their corresponding ECM; this makes it difficult to derive an experimentally appropriate MSC seeding number from *in silico* simulations. Interestingly, Reichert *et al.* also studied PCL scaffold-implanted sheep defects with initial MSC seeding. They seeded 35 million cells in each scaffold, but the outcome was very similar to the PCL scaffold alone [9]. Some MSCs might not have stayed in the scaffold but been washed out, or not have been active enough when implanted back in the animals. Other experimental studies reported a higher success in seeding MSCs in bone scaffolds [132], and suggested that MSCs derived from the periosteum performed better than from the bone marrow [133]. Besides, in the work presented here, the number of initially seeded MSCs was also shown to influence the long-term tissue distribution: because the homogeneous MSC presence in the scaffold pores contributed to tissue deposition throughout the scaffold, the mechanics was notably different to the one obtained with bone growth from the intact bone extremities. Consequently, tissue deposition and distribution in the defect were different 12 months post-surgery.

3.5.2 Scaffold surface guidance

Experimentally, it has been reported that structured scaffolds act as templates guiding bone regeneration [13, 42, 43]. In the simulation set-ups, two mechanisms were hypothesised by which this guidance could happen: surface-guided MSC migration, namely the fact that cells would go to a new position only if that position was adjacent to an existing tissue or scaffold surface; and surface-guided ECM deposition, implemented by the fact that MSCs would differentiate towards new phenotypes only at positions adjacent to existing surfaces. A feature similar to surface-guided ECM deposition has already been described elsewhere [73], where the authors assumed bone to be deposited only onto existing bone or scaffold surfaces (thanks to their osteoconductive properties). In this thesis as well, the implementation of surface-guided ECM deposition allowed good agreement with experimental data for both the soft titanium and the PCL scaffolds.

The addition of surface-guided MSC migration was necessary to reproduce the empty defect non-union and the still incomplete PCL scaffold defect healing; however, for the titanium scaffold set-up, it resulted in a more impaired regeneration than actually seen *in vivo*. In that latter case, the ABG presence was likely to over-rule surface-guided MSC migration by providing a high stimulation and an appropriate environment for MSC migration everywhere within the scaffold pores.

3.5.3 Limitations and suggestions for future work

The computer models for bone regeneration had several limitations due to hard-ware and computing time constraints. First, re-vascularisation of the defect was not included in the model as done previously [67, 134], although it can be critical in large defects [20, 59–61]. Possible lack of vascularisation was indirectly modelled by reduced cell activity levels, but future studies could further investigate re-vascularisation in large bone defects and scaffolds and its dependence on mechanical and biological factors. Second, the defect geometries were idealised, with bone segments simplified as cylinders and using ideal instead of real 3D-printed geometries of the scaffolds; the resulting mechanical environment should not be strongly modified, but future studies should use experimental images to define regenerating defect geometries, in particular in the case of patient-specific models. The FE discretisation was fairly coarse and in the case of the PCL scaffold, relying on poor merging operations. However, the mesh convergence analysis performed for the titanium scaffold suggested that this model would appropriately describe the mechanical environment in the callus (Section A.2). In addition, the ABM matrix points were larger than the actual cells they should represent; this assumption impacted the regeneration dynamics predictions, but not the final tissue distribution (Section A.5).

Some specific experimental features from the titanium scaffolds could not be reproduced with the developed computer model: the limited bone growth under the plate (different from the PCL scaffold case), fibro-cartilage deposition directly around the scaffold struts and in general the impaired healing for the stiff scaffold. Further studies are needed to investigate these features in detail. Specifically, surface treatment might be a reason why so few bone grew onto the titanium scaffold struts [135–137]. A biological reaction or disrupted soft tissues

around the fixation plate might explain (in addition to low strains) the limited bone growth under the plate. Additional mechanics influences not taken into account in the computer model yet could explain the stiff scaffold impaired healing, e.g. on cell migration [138–140] or proliferation [141–143].

Future work should further apply this model to different scaffold designs and experimental settings to assess its predictive capability in a variety of situations. The comparison to more experimental data would allow refining further the computer model and improve its generic predictive ability of the scaffold-supported bone regeneration process.

4

Scaffold design parametric studies

In this chapter, the results of the investigation of the influence of scaffold design parameters on bone regeneration predictions are presented and discussed. First, the effect of scaffold geometry and material property changes on bone regeneration outcome was investigated on a simulation set-up similar to the experimental PCL scaffold (Section 4.1). Second, the differences between initial mechanoregulation stimulus, bone regeneration predictions and longer-term remodelling predictions were investigated on a set of cubic scaffold geometries with varying cubic pore sizes (Section 4.2) [144].

4.1 Effect of PCL scaffold design parameters on bone regeneration

4.1.1 Influence of surface-area-to-volume ratio

The four scaffold design geometries used for the SA/V (surface-area-to-volume ratio) study are shown on Figure 4.1 a-d: D1 had the highest SA/V (278.21 mm^{-1}) and D4 the lowest (31.79 mm^{-1}). Even though their porosities were different (91 to 60%), all designs yielded comparable strain levels in the defect region at the initial time-point (Figure 4.1 e-h), corresponding to an initial mechanoregulation stimulus favouring bone in a large majority of the callus volume. To study the effect of the scaffold architecture independently from the mechanics, a fifth design was used (D4_soft), namely D4 with softer material properties (Young's modulus 70 MPa instead of 400 MPa); the corresponding strain distribution post-implantation compared well with design D1 (Figure 4.1 e, i).

The MBBR (mechano-biological bone regeneration) model, including surface guidance and latency period implementations as validated for the PCL scaffold set-up, predicted large variations in terms of bone regeneration outcome for these designs. Surprisingly, regenerated bone proportion in the ROI (inter-cortices) was inversely correlated with the available surfaces (Figures 4.1 j-m, 4.2 a). In D3 and D4, bridging was complete 12 months post-surgery, with 21 and 27% bone in the inter-cortices region, respectively, whereas D1 showed a very impaired
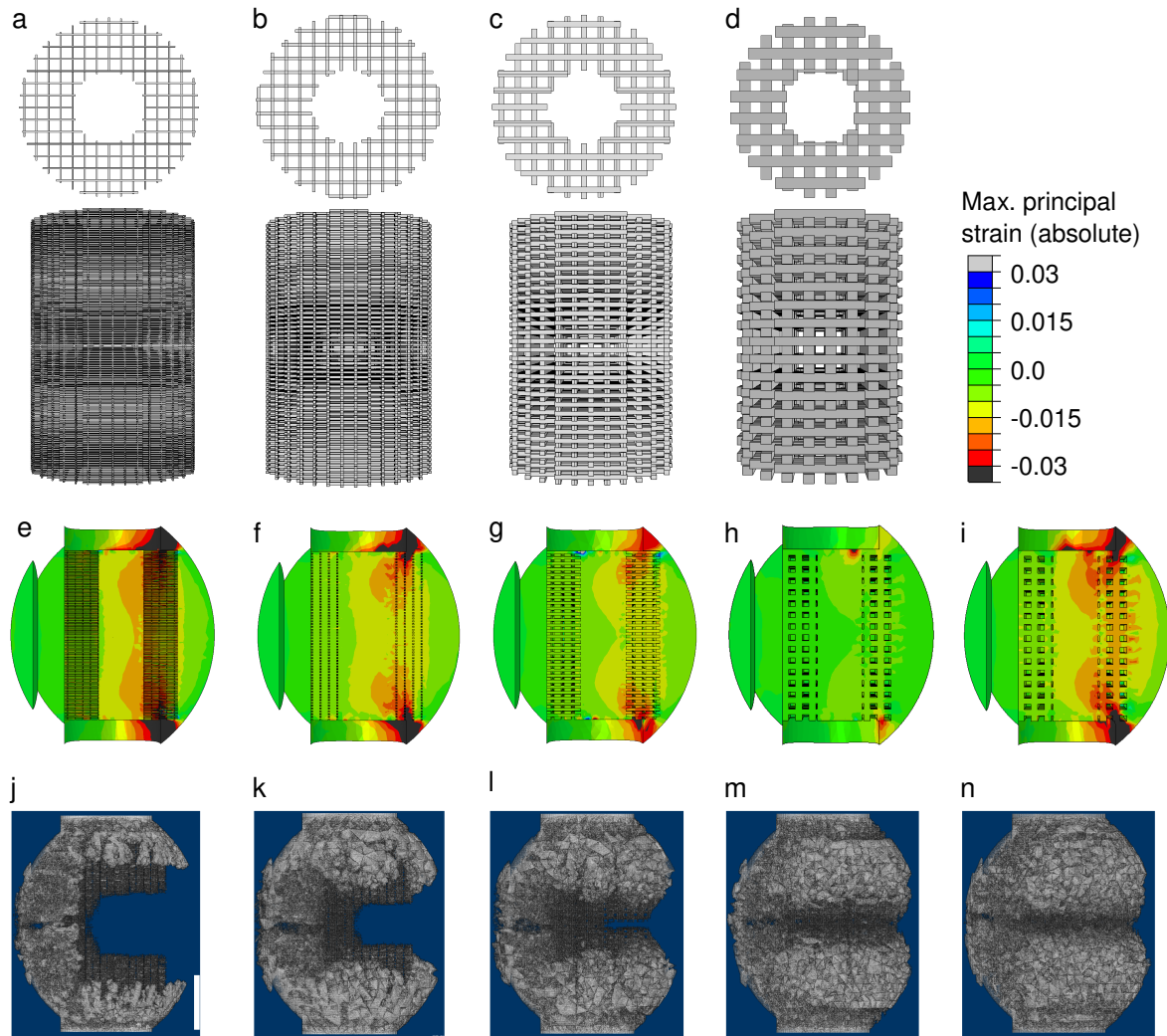
Figure 4.1 – **Surface-area-to-volume ratio effect – geometry, strain distribution and µCT predictions**: (a-d) scaffold designs (top and side views); (e-i) strain distribution post-implantation; (j-n) µCT image prediction 12 months post-surgery for scaffold D1 (a, e, j), D2 (b, f, k), D3 (c, g, l), D4 (d, h, m) and D4_soft (d, i, n). The strain colour legend is given on the top-right; the µCT scale bar represents 10 mm.

healing, with bridging seen mostly along the plate and only 9% regenerated bone in the inter-cortices region.

Detailed analysis of the cellular activity in these scaffolds showed impaired MSC migration, proliferation and differentiation (hence, tissue deposition) in D1 and D2 compared to D3 and D4 (Figure 4.2 b-d). Although the overall SA/V was higher in D1 compared to D4, each individual scaffold surface was much smaller, thus reducing MSC possibilities to migrate or differentiate locally.

Interestingly, the additional D4_soft case yielded even better bone regeneration than D4 (Figures 4.1 n, 4.2 a) both 3 and 12 months post-surgery. Thus, the more strained environment did not explain the differences observed between D1 (strain levels comparable to D4_soft) and D4, that should be mostly caused by the scaffold architecture.
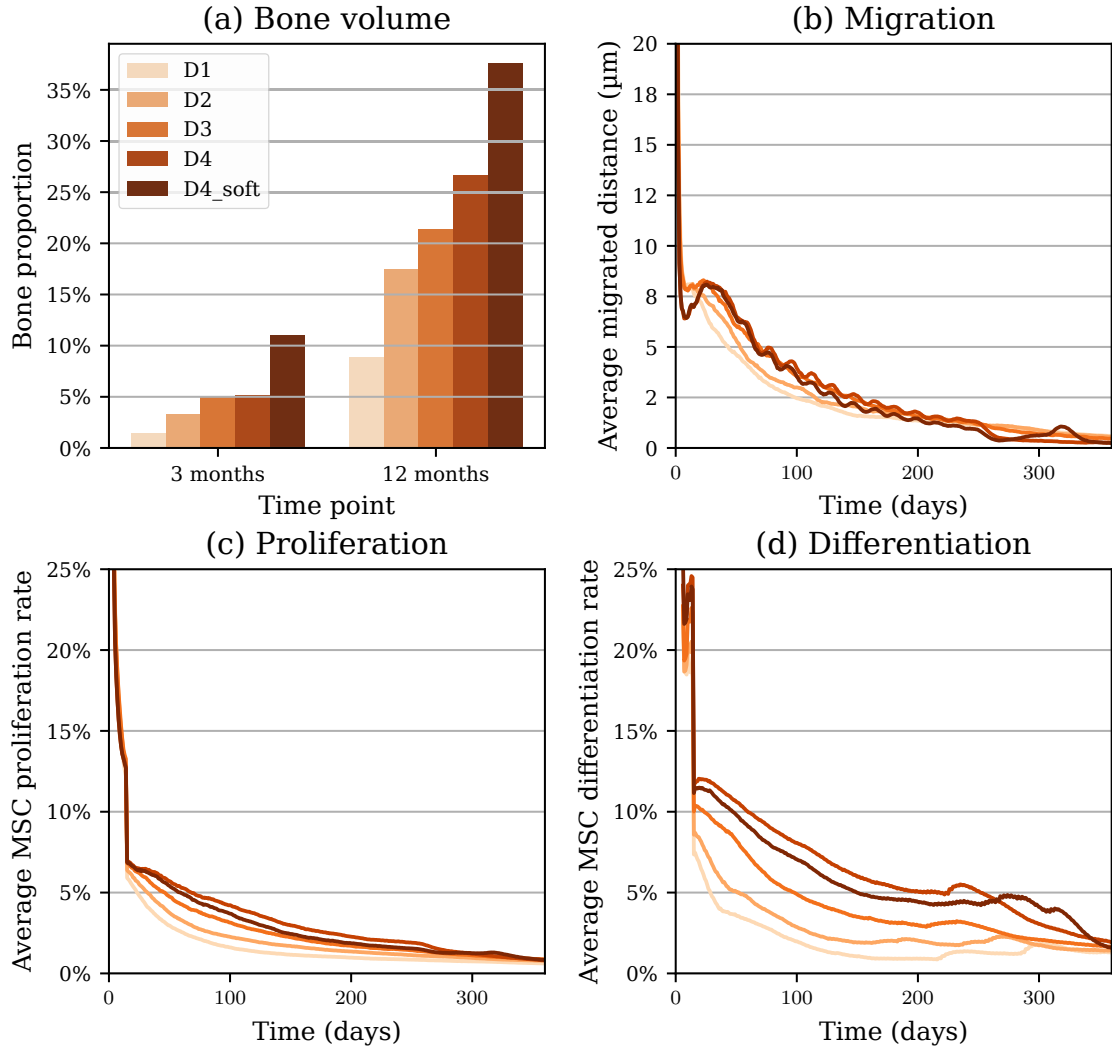
Figure 4.2 – **Surface-area-to-volume ratio effect** – **quantification**: (a) bone proportion in the inter-cortical available volume 3 and 12 months post-surgery predicted by the MBBR model with surface guidance and latency period; (b) average migrated distance by the MSCs over time; (c) average MSC proliferation rate over time (max 30% after the latency period); (d) average MSC differentiation rate over time (max 15% after the latency period).

4.1.2 Influence of geometrical and material parameters

One material and three geometrical parameters were studied on a similar PCL scaffold-derived geometry by means of a 4-parameter, 3-level Taguchi array: scaffold Young's modulus, strut size, inner radius and inter-strut distance. For each scaffold design, the MBBR model was used to simulate bone regeneration over 12 months. The outcome was defined as the proportion of bone in the inter-cortices region after 12 months. Corresponding predicted µCT are shown on Figure 4.3, where notable differences in terms of regeneration extent and bone volumes can be seen. Bone proportion quantification in the inter-cortices further confirmed the variation observed qualitatively (Figure 4.4), with the worst design (T5) leading to 1% regenerated bone whereas the best design (T3) yielded more than 30% after 12 months.

The detailed analysis of the Taguchi array results was done by computing the average outcome obtained for all (2 or 3) simulations at each parameter level (low, intermediate
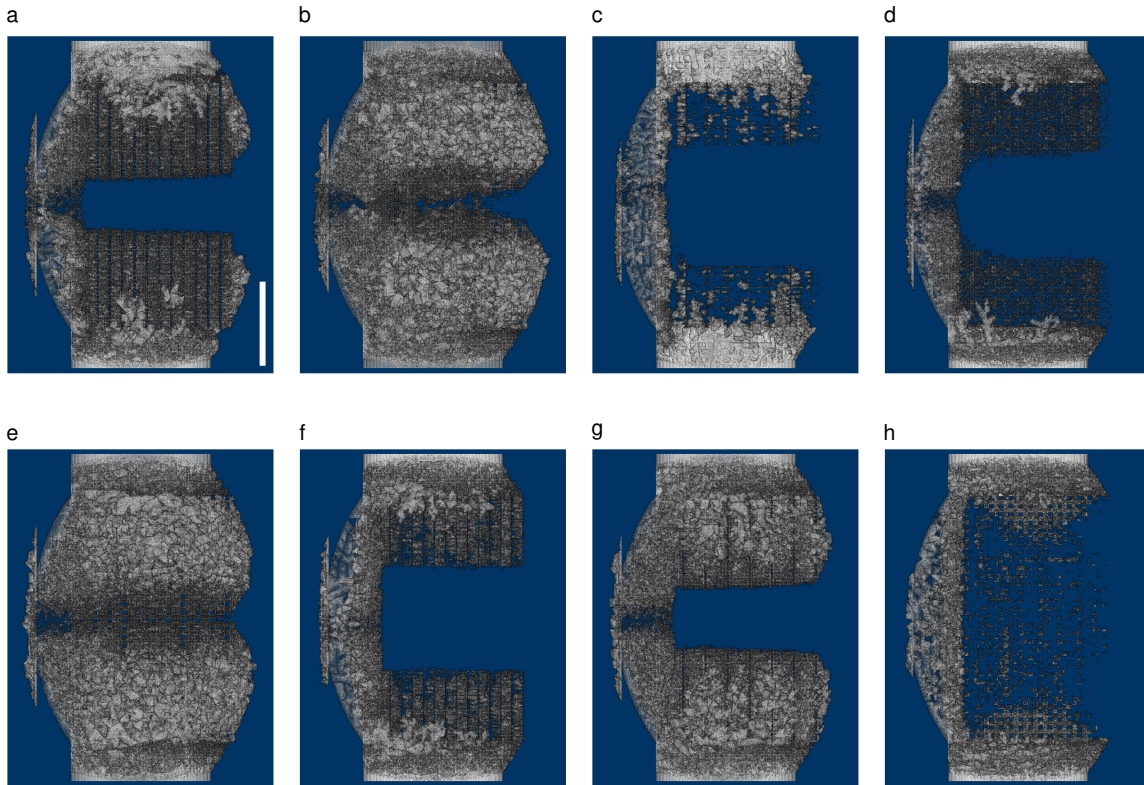
Figure 4.3 – Design parameter sensitivity analysis – µCT predictions at 12 months post-surgery: (a) T2, (b) T3, (c), T4, (d) T5, (e) T6, (f) T7, (g) T8, (h) T9. The scale bar represents 10 mm.
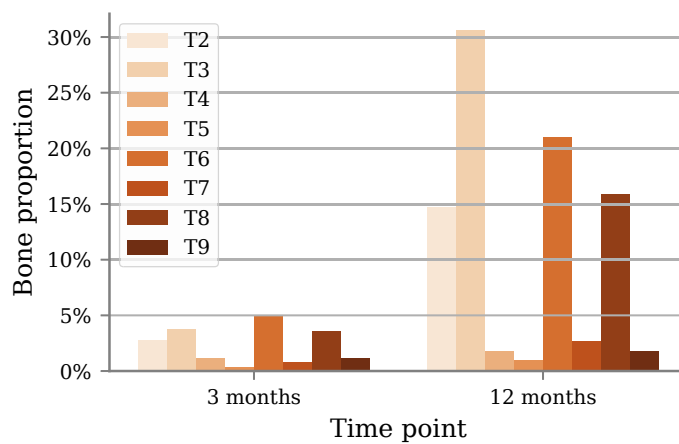
Figure 4.4 – Design parameter sensitivity analysis – quantification: Bone proportion in the inter-cortical shell available volume 3 and 12 months post-surgery as predicted by the bone regeneration model with surface guidance and latency period

or high) and the corresponding sum of squared deviations (the sum of squared differences from the mean) (Table 4.1). This latter value is a measure of the individual influence of a given parameter: the bigger the value is, the more influence the parameter has on the outcome. All design parameters were found to have a marked effect on the regeneration outcome. Scaffold's Young's modulus had the most pronounced effect, with lower Young's modulus values (400 MPa) being notably more favourable for bone regeneration. In particular, the stiffest material (40 GPa) led to mechanoregulation stimuli lying in the bone resorption zone, thus not favouring bone regeneration. Strut size and inter-strut distance came both as next most influential design parameters, with higher values leading to more regenerated bone. With too small struts or pores, healing was notably impaired (2.20% and 1.34% regenerated bone in the inter-cortices, respectively). Lastly, the scaffold inner radius mimicking the bone marrow cavity was found to have the least impact among the range studied (2, 4 and 6 mm). Interestingly, in this case the variations were not monotonous, but both low and large values seemed to be more favourable for bone regeneration than the intermediate one.

Parameter	Low level	Intermediate level	High level	SSD
Young's modulus	22.61%	7.91%	6.74%	0.0484
Strut size	2.20%	10.48%	17.78%	0.0373
Inner radius	18.43%	6.06%	11.38%	0.0237
Inter-strut distance	1.34%	12.77%	16.06%	0.0369

Table 4.1 – **Design parameter sensitivity analysis**. For each parameter, average regenerated bone proportion in the inter-cortices at each level and sum of squared deviations (SSD) are given.

4.2 Dynamics of the bone regeneration process in a cubic scaffold

In the following sub-sections, specific cubic scaffold designs will be referenced by capital letters as follows (Figure 4.6 a-d represent the corresponding scaffold designs):

A A design with large horizontal pores: $x_1 = 0.9$ mm, $x_2 = 0.5$ mm

B The design obtaining best outcome right after implantation: $x_1 = 0.5$ mm, $x_2 = 0.9$ mm

C The design obtaining best outcome after 60 days: $x_1 = 0.7$ mm, $x_2 = 0.8$ mm

D A design with small vertical pores, showing largest difference between post-implantation and regeneration outcome: $x_1 = 0.6$ mm, $x_2 = 0.1$ mm

4.2.1 Initial mechanical signals within the scaffold pores

The initial mechanoregulation stimulus distribution within the cubic scaffold pores was found to be strongly depending on the pore sizes in the 181 included scaffold designs: the outcome ranged from 5 (darker red, Figure 4.5 a) to 99% (darker green, Figure 4.5 a) tissue volume fraction under bone-favouring initial mechanical signals. In particular, large horizontal pores (>0.8 mm) systematically led to non-favourable designs. This was for instance the case
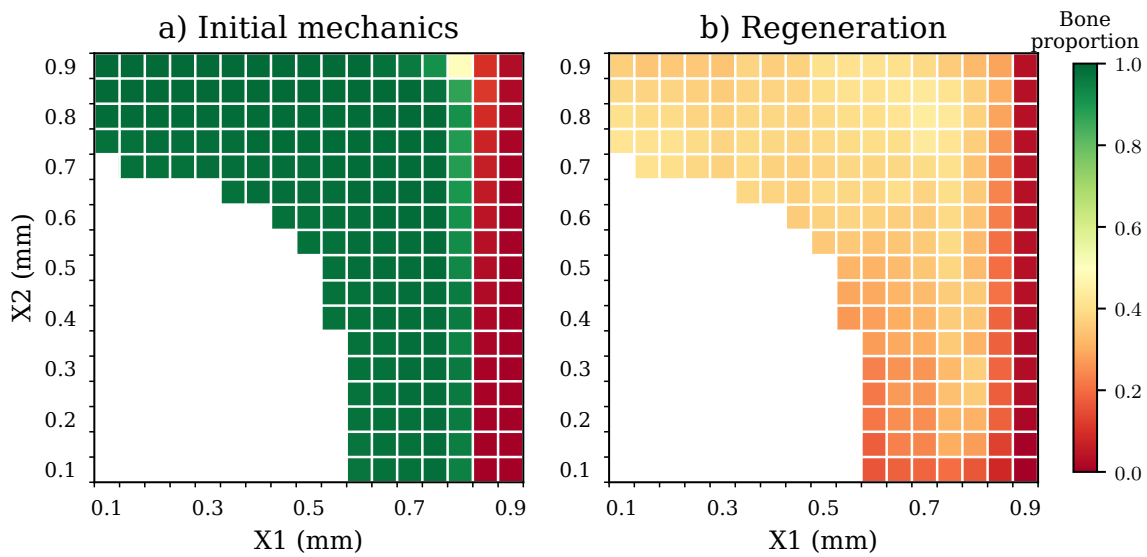
Figure 4.5 – **Cubic scaffold parametric study** – **bone fraction outcome** depending on pore sizes: (a) tissue volume fraction under bone-favouring initial mechanical signals; (b) regenerated bone volume fraction after 60 days

for scaffold design A (Figure 4.6 e). In this design, fibrous tissue was favoured in most of the scaffold pores due to the large deformations; bone was favoured only in small areas on the top and the bottom of the scaffold.

The design yielding best initial outcome was design B (Figure 4.6 b, f) with large vertical pores and intermediate-size horizontal pores. For this design, initial mechanical signals favoured bone in more than 99% of the available tissue space.

4.2.2   Bone regeneration predictions

Similarly, regenerated bone volume fraction after 60 days was also shown to be strongly depending on the pore sizes in the 181 included scaffold designs and varied from 5 (dark red, Figure 4.5 b) to 44% (yellow, Figure 4.5 b) regenerated bone in the available tissue space. Designs with large horizontal pores, such as design A, also performed poorly when looking at the full regeneration process, with a tissue distribution following closely the patterns predicted by the initial stimuli (Figures 4.6 e, i).

However, other scaffold designs showed marked differences between the initial mechanical stimulus and the regenerated bone volume predictions. For example, design B yielded 99% tissue under bone-favouring initial mechanical signals but 40% regenerated bone after 60 days (Figures 4.6 f, j). Design D showed an even stronger difference, with 98% bone-favouring initial mechanical signals but only 16% regenerated bone (Figures 4.6 h, l). In the latter case, the difference was partly due to a more extended fibrous tissue and cartilage regeneration than initially predicted; and mostly to a very slow regeneration process caused by the small vertical pore size that impaired MSC infiltration into the scaffold. Actually, all tested designs with 0.1-mm horizontal pores showed poor healing outcome (Figure 4.5 b).

According to the regeneration prediction, the best-performing design was scaffold C with fairly large horizontal and vertical pores (0.7 and 0.8 mm, respectively); it yielded 44%

regenerated bone after 60 days. Also in this case, there was a large difference when comparing to initial mechanical signals that favoured bone in 99% of the tissue volume. After 60 days, bone could still be seen in large parts of the scaffold pores (Figure 4.6 k). However, large extents of fibrous tissue were present close to the scaffold walls and in the middle of the scaffold, where most of the deformation was concentrated once the rest of the tissue volume was filled with stiffer bone.
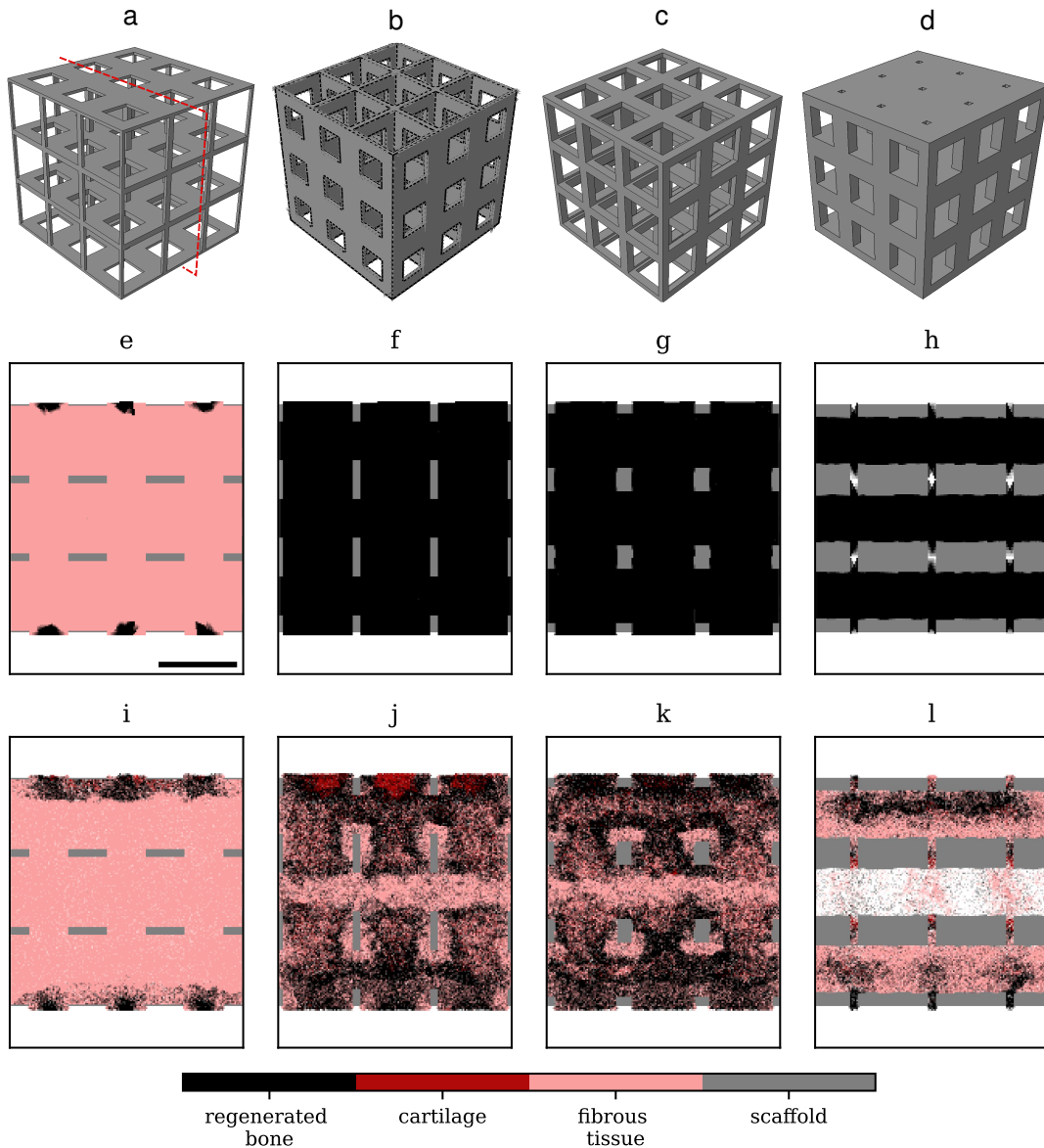
Figure 4.6 – Cubic scaffold parametric study – specific scaffold designs: (a-d) scaffold design, (e-h) tissue distribution favoured by the post-implantation mechanical stimulus in the mid-sagittal plane (depicted by the red dotted line on a), (i-l) tissue distribution after 60 days in the mid-sagittal plane, for scaffold designs A (a,e,i), B (b,f,j), C (c,g,k) and D (d,h,l). Colour code for the regenerated tissues or mechanical stimuli is given below; the scale bar represents 1 mm.

4.3 Discussion

Computer models for scaffold-supported bone regeneration can be used to predict the effect of specific scaffold design parameters and better inform future scaffold design, thus reducing the need for costly and ethically questionable *in vivo* experiments. Here, the computer model validated for the PCL scaffold set-up was used to investigate the effect of varying the SA/V by means of changing the strut size; and the combined effects of strut size, pore size, inner hole radius and material properties. In addition, the baseline computer model for bone healing was used to investigate a simplified cubic scaffold geometry in a systematic manner, with a focus on pore size and comparison between different time horizons (initial mechanical signals, regeneration, long-term remodelling).

4.3.1 Strut size and surface-area-to-volume ratio

The SA/V study revealed that designing a scaffold with more surfaces, in particular a higher SA/V, did not support better bone regeneration, although surface guidance of cell migration and ECM deposition was hypothesised. The exact architecture and, in that case, the extent of each individual surface seemed more critical to enhance bone regeneration. In this study, designs D3 and D4 (with thickest struts and lowest SA/V) were found to perform best, in particular due to a faster regeneration process compared to D1 and D2. MSC migration and differentiation was enhanced due to the larger surfaces at hand; proliferation also showed an increase as cell space was less crowded and more free space was available for new cells. In addition, the lower porosity of designs D3 and D4 also increased the healing speed due to a lower volume to fill with cells and tissues.

Experimentally, only a few studies investigated the impact of changing scaffold strut size. Pobloth and colleagues showed 1.2-mm struts to be more beneficial for bone regeneration than 1.6-mm ones in a titanium honeycomb scaffold implanted in sheep [13]. However, in that case, the different mechanics – due to a much stiffer scaffold material – likely explained the observed discrepancy. In addition, the struts were very thick compared to the cases studied here and resulted in SA/V of 4.8 and $3.7\,mm^{-1}$ for the 1.2 and 1.6-mm scaffold designs, respectively; these ratios were orders of magnitude lower than the ones studied here. Stok and colleagues saw no impact of the strut size (120 and $230\,\mu m$, yielding high SA/V) on another titanium scaffold performance [10]. A further titanium scaffold was studied by de Wild and colleagues who found struts of size 300-400 μm to yield highest bone regeneration volumes in rat calvaria defects [145]. These best-performing designs corresponded to the biggest struts and lowest SA/V (9-$12\,mm^{-1}$) tested in the experimental study, which is in line with the *in silico* results presented here.

4.3.2 Pore size and porosity

The parametric studies presented in this chapter showed contrasting results concerning porosity: the PCL scaffold SA/V study suggested lower porosities (60%) to best support bone regeneration, while the PCL scaffold combined effect analysis suggested bigger pores, hence higher porosity, to achieve the best outcome. Lastly, the cubic scaffold study pointed

towards high porosities as being very beneficial, within a range of ca. 70-90%; higher porosities ($>90\%$) caused too high deformation and fibrous tissue formation. This range is in line with experimental observations [146]. Such contrasting results emphasise the importance of the actual scaffold architecture over a pure macroscopic measure such as porosity to determine the scaffold performance in a bone regeneration context. In fact, the combination and interplay of different scaffold design parameters are critical and account for the contrasting predictions: different porosities depend on the pore and strut sizes that both play a role on bone regeneration; and the scaffold material properties lead, together with the scaffold structure, to a different mechanical environment in the defect that can be favourable or detrimental for bone in-growth.

The PCL scaffold geometrical and material parameter study pointed towards larger pores to be more beneficial for proper cell infiltration and bone formation in the range studied here (600-2400 µm). The cubic scaffold study led to similar conclusions, although the studied range was slightly smaller (100-900 µm): vertical pores should not be smaller than ca. 200-300 µm for good cell infiltration; on the contrary, horizontal pores should not be too large (>850 µm) to avoid too deformable constructs leading to fibrous tissue formation. These results contrast with experimental data suggesting rather small pores (ca. 300 µm) as most beneficial for cell attachment, differentiation, migration and/or bone deposition [11, 19, 20, 147]; however, other values have been reported depending on the exact experimental settings, e.g. 800 µm [21, 145] or 600-1000 µm [146]. Nevertheless, the pore size changes in the computer studies presented here were closely correlated with porosity changes, which explains that bigger pores were more beneficial; again, this highlights the relevance of actual scaffold architecture when investigating scaffold performance. For instance, pore sizes could be considered as dictated by biological requirements and a scaffold architecture could then be built by changing e.g. strut size and arrangement.

4.3.3 Scaffold material properties

In the SA/V study, the fact that different strut sizes resulted in different porosities and mechanics did not explain the more impaired healing for D1 and D2. Indeed, D4_soft (with strain levels comparable to D1) performed even better than D4, rather suggesting a favourable effect of lowering the scaffold Young's modulus. These results were confirmed by the geometrical and material parameter sensitivity analysis, where a lower Young's modulus was also predicted to enhance the bone regeneration outcome. These results are in line with an experimental study where scaffolds made of (soft) polyamide showed better healing outcome than made of (stiff) titanium [14].

4.3.4 Dynamics of the bone regeneration process

The cubic scaffold parametric study is the first *in silico* study that analyses the influence of the bone scaffold design on its mechanobiological performance at different time horizons. Marked differences could be observed between initial (post-surgery) and regeneration outcome predictions, suggesting that the post-surgery mechanical signals cannot be taken as an approximation of the regeneration outcome. In particular, some designs yielded extremely

favourable bone regeneration conditions right after implantation, but a poor healing outcome when taking the actual dynamic regeneration process into account.

Only a few *in silico* studies so far have considered mechanobiological conditions in bone scaffold design. Boccaccio and colleagues performed a series of scaffold unit cell mechanobiological optimisation [70, 82, 104, 105, 148]. However, they took only the initial time-point into account, with an optimisation objective consisting in maximising the amount of tissue under bone-favouring mechanical signals. In a study considering a cubic scaffold of side 1.913 mm with square pores, a Young's modulus of 1000 MPa and a pressure load of 1-2 MPa, their optimal design had a lower porosity than the designs here, and lower bone-favouring volume (only 30% of the tissue volume) [70]. A further *in silico* study used a similar geometry (cubic scaffold of side 1.913 mm with square pores) to investigate the effect of porosity, Young's modulus, loading and degradation behaviour on predicted bone regeneration, taking the full regeneration process into account [66]; with a Young's modulus of 1000 MPa and under a pressure load of 1 MPa, the more porous design (70% porosity) performed best and yielded 43% regenerated bone, close to the results presented in this chapter. Other *in silico* studies compared initial and regeneration outcome in specific designs: a 2D segmental bone defect scaffold [109] and a spine fusion device [69]. Both studies showed, similar to the findings of the studies presented in this chapter, a large difference between initial mechanical signals and actual regeneration predictions.

4.3.5   Limitations and suggestions for future work

The scaffold design parametric studies of this chapter include a few limitations. First and foremost, the MBBR computer model used in the cubic scaffold study has not been validated in a scaffold-supported context; in particular, surface guidance effects were not taken into account. However, the conclusions regarding the relevance of different time horizons would likely remain or even be exacerbated. The one used in the PCL scaffold studies has been validated in a similar experimental set-up but might not be usable with every different scaffold design. In particular, changing the material properties in the model would mean changing the material in reality; thereby, not only would the material properties be different, but the osteoinductive potential of the material (e.g. TCP) might be different. Here, the material was hypothesised to create certain biological stimulation for the healing process; this might not be true if the material is changed to e.g. an inert metal (to achieve a higher Young's modulus). Further validation against more versatile experimental studies would help gaining more understanding on scaffold design parameters' effect on bone regeneration and providing a more generic predictive computer model. In addition, (re-)vascularisation was not taken into account in the computer model, which can be critical in large bone defects [20, 61]; in fact, it was assumed to be sufficient to allow bone growth, and was indirectly taken into account in the biological activity impairment in the PCL scaffold studies. Future studies could specifically investigate which scaffold design best promotes re-vascularisation of the defect.

In addition, these studies focused on the regeneration potential of scaffolds in the mid-term (2 or 12 months, adapted to the scaffold size), but did not include other outcome such as ensuring that the scaffold-tissue construct would not fail; a long-term stability following bone

remodelling and a proper integration of the scaffold with the regenerated bone (only studied for the cubic scaffolds, where a limited effect was found); or on the contrary a proper scaffold biodegradation; and other biological or clinical requirements that would constrain some of the design parameters. For instance, the PCL scaffold inner hole radius and pore sizes are design parameters that might be dictated by experimental or clinical evidence: the inner hole should follow the bone marrow cavity, and literature suggest rather small pore sizes in the range of 300-800 µm for best MSC infiltration, differentiation into osteoblast and bone mineralisation [19, 21, 149].

The cubic scaffold study used a very simplified geometry and loading scenario (pure compression) that is not relevant for direct clinical applications. It should only be seen as a way to investigate certain basic properties of scaffold-supported bone regeneration, but conclusions cannot be translated as such to a clinical setting. Future work should look at more realistic geometries, e.g. derived from actual patient CT-scans, under realistic loading conditions, to derive which scaffold design properties would best support bone regeneration.

<div style="text-align: right; font-size: 6em; color: #cccccc;">5</div>

Scaffold design optimisation

In this chapter, the computer framework for scaffold design optimisation for bone regeneration is presented. First, it was applied to a cubic scaffold design to study the technical considerations needed to achieve reliable results; next, the framework was used for a more realistic scaffold optimisation (cylindrical scaffold in a long bone large defect).

5.1 Cubic scaffold

5.1.1 Non-graded design: influence of sampling size and type

First, the non-graded scaffold design with two design variables (horizontal and vertical pore sizes) was used to assess the initial sampling strategy, using a 181-input uniform sampling as a reference (Table 2.9, optimisation cases 1-4; Table 5.1, Figure 5.1).

Among the uniformly sampled geometries, the scaffold defined by $x_1 = 0.7$ mm and $x_2 = 0.8$ mm yielded highest amount of regenerated bone after 60 days (44.05%). Consequently, the surrogate optimisation case no.1 that used this initial data-set converged to an optimum defined by $x_1 = 0.7001$ mm and $x_2 = 0.8$ mm yielding 44.34% regenerated bone (Table 5.1). Tissue distribution in the mid-plane after 60 days showed bone in the scaffold pores close to the top and bottom, and fibrous tissue around some of the scaffold struts and in the central part of the scaffold (Figure 5.2: case 1).

When using the LHS technique for the initial sampling, optimums were not as good as the one obtained with the uniform sampling (Table 5.1). In particular, using 10 initial scaffold

Case	Initial sampling	x_1 (mm)	x_2 (mm)	Bone proportion
1	uniform (181)	0.7001	0.8000	44.34%
2	LHS (10)	0.7645	0.7055	40.20%
3	LHS (20)	0.7580	0.7533	41.95%
4	LHS (40)	0.7165	0.7833	44.10%

Table 5.1 – **Non-graded cube geometrical optimisation** – sampling influence
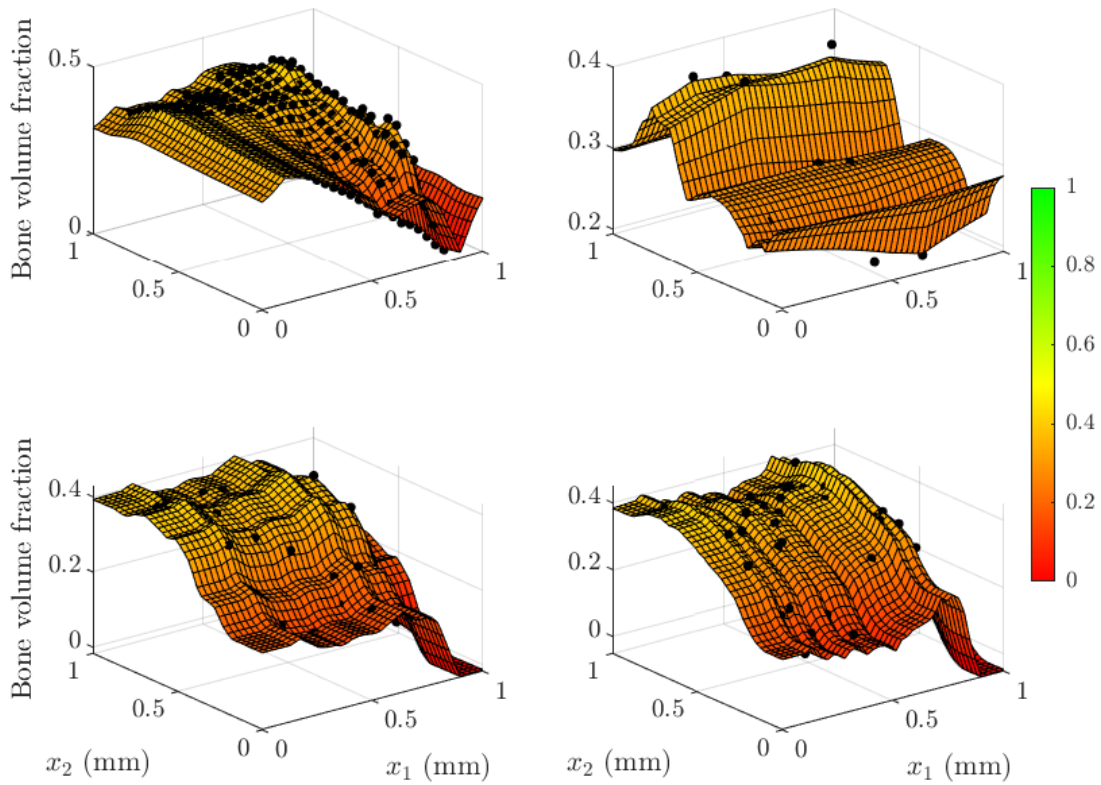
Figure 5.1 – Influence of initial sampling and size – surrogate surface responses: the surface response indicates the surrogate model prediction for given x_1, x_2 values (according to the colour scale given on the right); sampled points are shown additionally as black points.

geometries led to an optimum yielding only 40.20% regenerated bone. However, when using 40 initial scaffold geometries, the surrogate optimisation process converged to a scaffold design close to the one obtained with the uniform sampling ($x_1 = 0.7165$ mm and $x_2 = 0.7833$ mm) and performing similarly (44.10% regenerated bone, Figure 5.2: case 4). It was deduced from this first study that the initial sampling size need to be 20 times the number of variables for subsequent optimisation cases. With this approach, an optimum could be found in 72 h on a standard desktop computer instead of minimum 2-3 months using a classic optimisation process (42 function evaluations instead of hundreds or thousands of evaluations).

The corresponding surrogate model surface responses (objective as a function of x_1 and x_2, Figure 5.1) also revealed a more similar behaviour with the initial data-set of 40 samples obtained by LHS as compared to the uniform sampling. The main differences could be seen for low values of x_1 and x_2, where no data was included in the uniform sampling and that are excluded from the optimisation process because they have too low porosities.
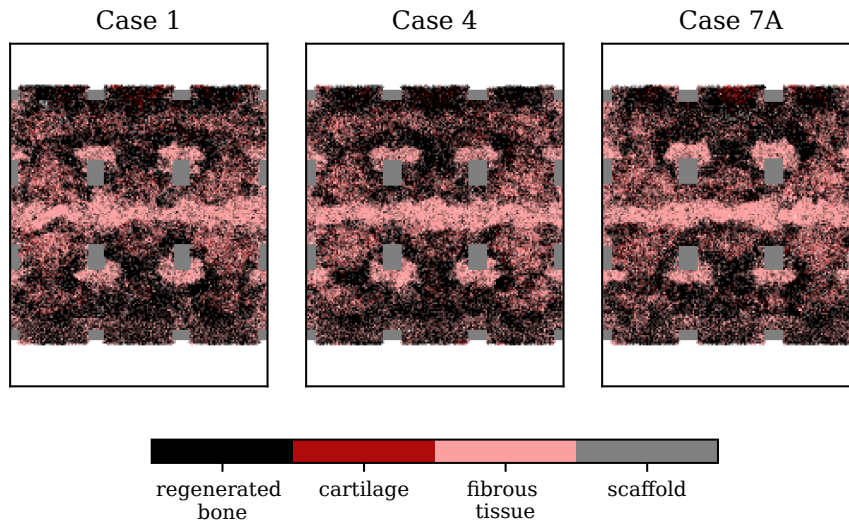
Figure 5.2 – **Optimal cubic scaffold geometries under compression** – **regeneration histological prediction**: middle slice in histology-like colours after 60 days for the optimal cube obtained in cases 1, 4 and 7A. The optimisation cases were defined in Table 2.9.

5.1.2 Graded pore design optimisation

Second, a graded pore cubic scaffold design (four variables) was used to assess surrogate model and optimisation algorithm performance (Table 2.9, optimisation cases 5-7 under compression and 8-12 under compression and bending). Two different initial data-sets (named A and B) were tested, both being obtained by a Latin hypercube sampling of size 80. Further details on the performance of various surrogate models in this configuration are given in Appendix B.1; here, only MARS and Kriging were investigated, that were both yielding a root mean square error of approximately 5% when built on one data-set (A or B) and tested on the other data-set (B or A).

5.1.2.1 Cubic scaffold under compression loading

The optimisation algorithm choice had a marked impact on the surrogate optimisation outcome. For instance, using data-set A, the direct search algorithm performed better than both GA and PSO, with a graded design close to the non-graded optimum obtained in the previous section. This design yielded 44.01% regenerated bone after 60 days, comparable to non-graded design optimisation (Table 5.2, Figure 5.2, case 7A). Interestingly, the optimal design was not taking much benefit from the grading possibility, with values x_1-x_3 being fairly similar to each other. In addition to the optimisation algorithm influence, the actual data-set used to initialise the surrogate model and the optimisation process was also shown to have an impact: data-set A achieved better results than data-set B with GA and direct search algorithms.

Case	Surrogate model	Algorithm	x_1 (mm)	x_2 (mm)	x_3 (mm)	x_4 (mm)	Bone proportion
5A	Kriging	GA	0.5928	0.1058	0.1070	0.6768	43.66%
6A	Kriging	PSO	0.5989	0.1000	0.1070	0.6265	42.32%
7A	Kriging	direct search	0.6549	0.7394	0.7198	0.7797	44.01%
5B	Kriging	GA	0.1653	0.7591	0.7287	0.7809	43.33%
6B	Kriging	PSO	0.1653	0.7591	0.7287	0.7809	43.48%
7B	Kriging	direct search	0.1802	0.7591	0.7287	0.7584	43.22%

Table 5.2 – **Graded cube geometrical optimisation under compression** – optimisation algorithm evaluation

5.1.2.2 Cubic scaffold under compression and bending loading

When the cubic scaffold was subjected to combined compression and bending loading, it resulted in an overall lower bone regeneration potential due to more fibrocartilage formation (caused by more deformation). In addition, in many cases the optimisation algorithm had difficulty converging and the optimal design was actually the best design from the initial data-set (cases 10A, 11A, 12A). The optimal design was obtained here with Kriging surrogate modelling technique and the PSO algorithm. In that case, the design was very graded ($x_1 = 0.46$ mm while $x_2 = 0.12$ mm and $x_3 = 0.13$ mm) and yielded 40.46% regenerated bone in the scaffold pores. Lastly, also here the initial data-set was shown to have an influence, with data-set A leading to consistently more optimal designs than data-set B.

Case	Surrogate model	Algorithm	x_1 (mm)	x_2 (mm)	x_3 (mm)	x_4 (mm)	Bone proportion
8A	Kriging	GA	0.3170	0.1218	0.1527	0.6926	39.44%
9A	Kriging	PSO	0.4555	0.1174	0.1317	0.6664	40.46%
10A	Kriging	direct search	0.3170	0.1218	0.1527	0.6926	39.44%
11A	MARS	PSO	0.3170	0.1218	0.1527	0.6926	39.44%
12A	MARS	direct search	0.3170	0.1218	0.1527	0.6926	39.44%
8B	Kriging	GA	0.5861	0.1795	0.3786	0.6793	38.91%
9B	Kriging	PSO	0.4967	0.1793	0.2469	0.7148	39.08%

Table 5.3 – **Graded cube geometrical optimisation under compression and bending** – optimisation algorithm and surrogate model evaluation. For optimisation cases 10-12, only data-set A was used as it performed better than data-set B

Based on the optimisation performed on the graded cubic scaffold under compression alone and compression combined with bending, the best-performing optimisation algorithm depended on each specific case. However, Kriging always performed better than MARS as a surrogate modelling technique.

5.1.3 Graded design with different pore sizes in x and y directions

Different optimisation algorithms and surrogate modelling techniques were used for the graded design optimisation with different pore sizes in x and y directions (7 variables) (Table 2.9, optimisation cases 13-16; Table 5.4). These results further confirmed that Kriging allowed a better surrogate optimisation process than MARS surrogate modelling technique (comparing cases 14 to 16).

Case	Surrog. model	Algorithm	x_1 (mm)	x_2 (mm)	x_3 (mm)	x_4 (mm)	x_5 (mm)	x_6 (mm)	x_7 (mm)	Bone proportion
13	Kriging	GA	0.6568	0.1034	0.1791	0.1198	0.1495	0.5855	0.7684	38.99%
14	Kriging	PSO	0.4541	0.1067	0.1791	0.3023	0.1799	0.5927	0.7548	40.11%
15	Kriging	direct search	0.5313	0.4326	0.1608	0.1198	0.1077	0.1860	0.7595	39.73%
16	MARS	PSO	0.7047	0.1000	0.7033	0.6007	0.1000	0.1064	0.7772	39.07%

Table 5.4 – Graded cube geometrical optimisation with different pore sizes in x and y directions – optimisation algorithm and surrogate model evaluation

Having more design variables did not yield higher regenerated bone volumes; however, the best design (obtained with Kriging and PSO, case 14) yielded a similar bone regeneration outcome as the 4-variable design (40.11%) but with a more porous scaffold: 62.3% instead of 49.7% (Table 5.4, case 9A). In that case, as for the 4-variable optimisation under mixed loading scenario, the PSO algorithm performed best; however, this algorithm does not allow the implementation of non-linear constraints (e.g. porosity).

5.1.4 Multiple material optimisation

A 7-layer cubic scaffold assuming a symmetry through the mid-xy-plane was optimised for the material properties of each layer; this resulted in 4 different variables (the Young's moduli in each layer) (Table 2.9, optimisation cases 17-19). Depending on the optimisation algorithm used, the outcome varied substantially, leading to very different material property distribution and regenerated bone volumes (Table 5.5). Regenerated bone proportion varied from 66.67 to 78.32%, the best case being obtained with the PSO algorithm. Scaffold material properties did not show a similar distribution rule between the obtained optimums; the main common observation was a consistently lower Young's modulus for the top and bottom layers and a very high Young's modulus for the middle layer.

The regenerated tissue distribution also revealed that best-performing designs showed larger amounts of resorption areas (white zones without any tissue, Figure 5.3: cases 17 and 19) in return for the reduced fibrous tissue extent.

Case	Algorithm	E_1 (MPa)	E_2 (MPa)	E_3 (MPa)	E_4 (MPa)	Bone proportion
17	direct search	5981	98697	9949	93502	75.63%
18	GA	679	14468	62967	92893	66.67%
19	PSO	5947	97962	24351	92792	78.32%

Table 5.5 – **Graded cube material optimisation** – optimisation algorithm evaluation. The kriging surrogate modelling method was used in all cases.
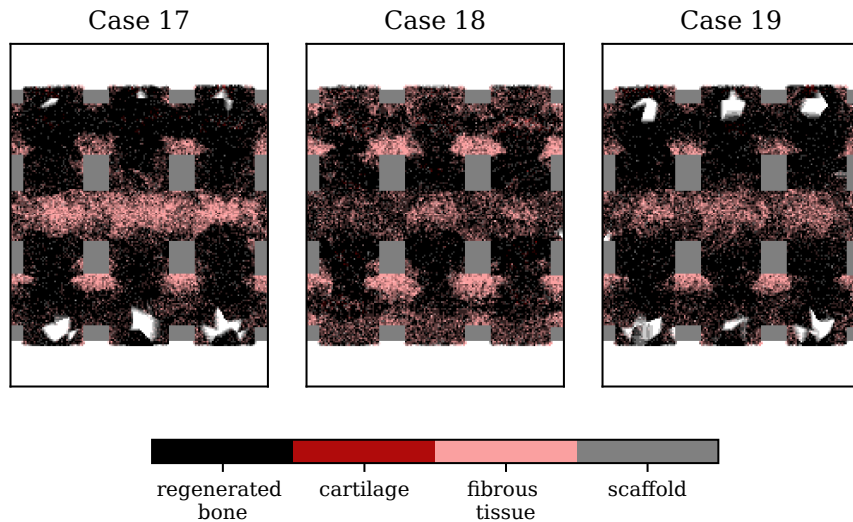
Figure 5.3 – **Optimal cubic scaffold materials** – **regeneration histological prediction**: middle slice in histology-like colours after 60 days for the optimal cube obtained in cases 17, 18 and 19.

5.2 Cylindrical scaffold

5.2.1 Titanium scaffold optimisation

The initial data-set of 60 titanium scaffold designs led to large variations in the predicted regenerated bone proportion, from 9.4 to 96.3%. Porosities of the tested designs (amount of free volume within the hollow cylinder defined by inner radius 5 mm and outer radius 10 mm) varied from 13 to 95%, and showed a moderate positive dependence with regenerated bone volume proportion (Figure 5.4). However, very high porosities (>90%) led to low regenerated bone volume predictions due to high deformations. For each porosity level, very different regenerated bone volumes were predicted depending on the exact scaffold architecture, e.g. from 35 to 90% regenerated bone around 55% porosity (Figure 5.4).

All optimisation algorithms led to a similar outcome in terms of optimal titanium scaffold design ($x_1 = 3.12$ mm, $x_2 = 3.26$ mm, $x_3 = 2.6$ mm) and regenerated bone volume proportion prediction (>95%); this optimal scaffold had 86% porosity. Figure 5.5 a shows the corresponding predicted tissue distribution at the end of the regeneration process. Interestingly, the possibility to have a graded design was not used in the optimum. However, some more graded designs

in the initial data-set led to >90% regenerated bone, with larger pores in the centre of the defect and smaller pores close to the bone extremities. For instance, the design defined by $x_1 = 1.84\,\text{mm}$, $x_2 = 3.45\,\text{mm}$, $x_3 = 2.26\,\text{mm}$ yielded 93% regenerated bone with 71% porosity (Figure 5.5 d). Compared to the optimal design, small regions of bone resorption along some scaffold struts were predicted; the remaining of the scaffold pore volume was filled by bone.
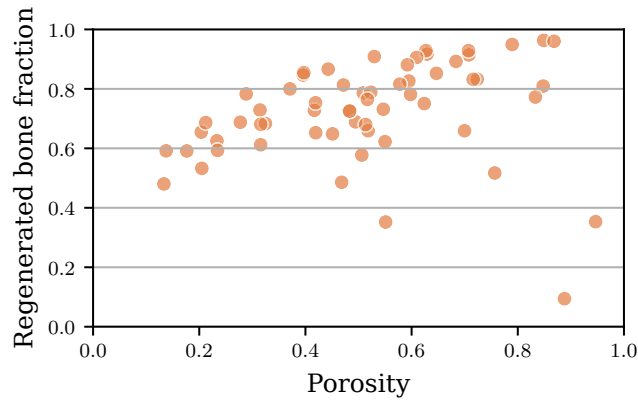
Figure 5.4 – **Cylindrical titanium scaffold objective function of porosity**: porosity of the scaffold is defined as the amount of free volume within the hollow cylinder defined by inner radius 5 mm and outer radius 10 mm; the regenerated bone fraction is counted within that scaffold pore volume.
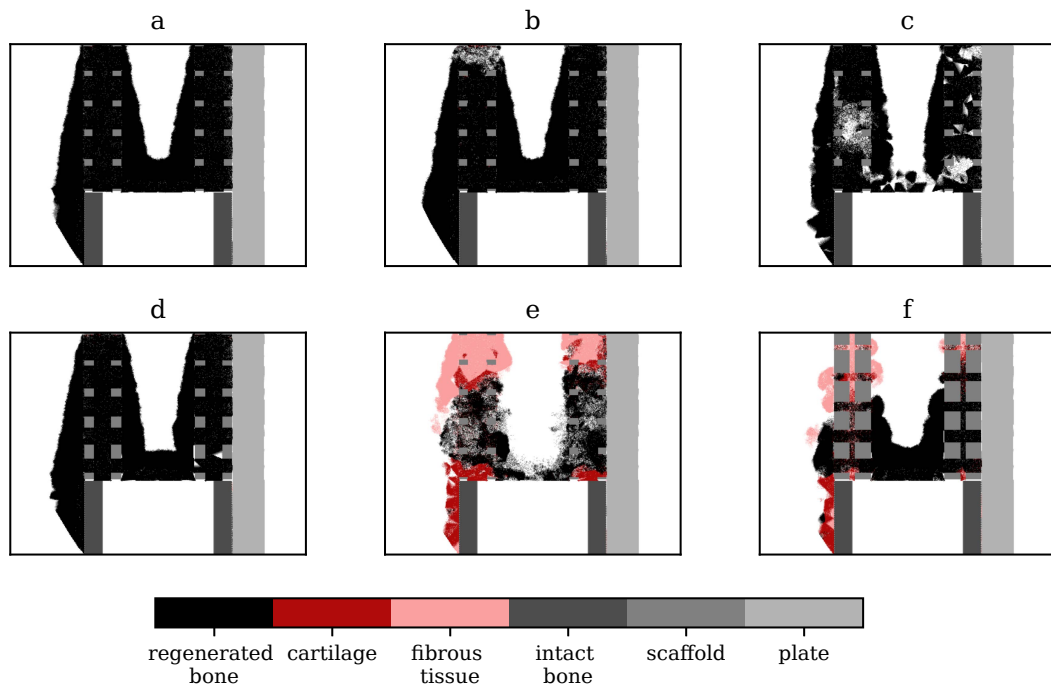
Figure 5.5 – **Optimal cylindrical scaffold designs** − **24-week histology prediction**: Effect of varying loading conditions on the optimal titanium scaffold design ($x_1 = 3.12\,\text{mm}$, $x_2 = 3.26\,\text{mm}$, $x_3 = 2.6\,\text{mm}$): (a) standard loading conditions, used to optimise the design; (b) loading values +50%; (c) loading values -50%. (d) Good-performing more graded titanium scaffold design ($x_1 = 1.84\,\text{mm}$, $x_2 = 3.45\,\text{mm}$, $x_3 = 2.26\,\text{mm}$). (e) Optimal titanium scaffold design ($x_1 = 3.12\,\text{mm}$, $x_2 = 3.26\,\text{mm}$, $x_3 = 2.6\,\text{mm}$) with a softer material (Young's modulus 0.2 MPa). (f) Optimal soft scaffold design ($x_1 = 1.9\,\text{mm}$, $x_2 = 0.77\,\text{mm}$, $x_3 = 0.7\,\text{mm}$).

77

Loading conditions being only an approximation of the expected loading in the defect area, an additional study was performed to compare the healing outcome in the optimal design with higher (+50%) and lower (-50%) compression and bending loading values (Figures 5.5 b, c). Higher loading led to a slightly reduced regenerated bone proportion (90%); lower loading had a stronger effect, leading to 79% regenerated bone and many resorption zones in the scaffold pores.

On the technical side, too many optimisation iterations led to an over-fitting of the surrogate model; in fact, the best design was usually achieved in the first 5 optimisation loops. The optimisation process required approximately 2 weeks for the initial runs (60 simulations) and 3-5 more days for the optimisation loops (5 to 20 more simulations), instead of months or years using a classic optimisation approach.

5.2.2 Soft scaffold optimisation

Simulating the same initial set of scaffold designs assuming a very soft material (Young's modulus 0.2 MPa) led to a marked difference in the regenerated bone predictions (Figure 5.6). Overall, the soft scaffolds led to less regenerated bone (20 to 60%) than the titanium scaffolds. In addition, less porosity was more favourable for bone regeneration because it decreased the deformation leading to fibrous tissue or cartilage formation and reduced the free scaffold pore volume to be occupied by bone.
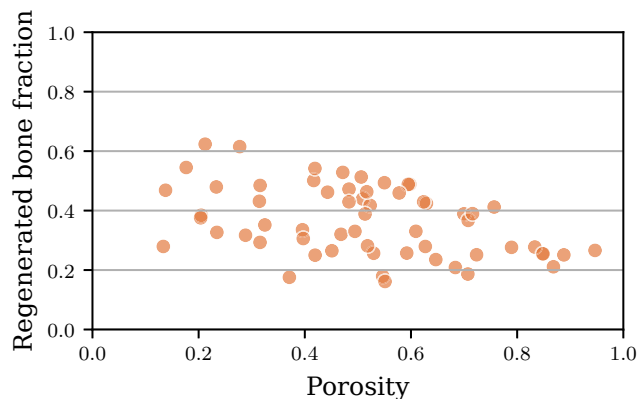
Figure 5.6 – Cylindrical soft scaffold objective function of porosity: porosity of the scaffold is defined as the amount of free volume within the hollow cylinder defined by inner radius 5 mm and outer radius 10 mm; the regenerated bone fraction is counted within that scaffold pore volume.

For instance, the titanium optimal design would perform very badly if made of that soft material, yielding only 27% regenerated bone after 24 weeks instead of 95% (Figure 5.5 e). In that case, much more fibrous tissue and cartilage were predicted due to high deformations (compared to Figure 5.5 a).

On the contrary, the optimal soft scaffold design, obtained with the PSO algorithm, was defined by $x_1 = 1.9$ mm, $x_2 = 0.77$ mm, $x_3 = 0.7$ mm, with a very low porosity (24%) (Figure 5.5 f). This design was predicted to yield 67% regenerated bone after 24 weeks in the scaffold pores; this outcome was not as good as with the titanium optimal design. Interestingly,

the soft scaffold optimum was a graded design, with larger pores close to the intact extremities and smaller ones in the centre of the defect.

5.3 Discussion

5.3.1 Optimisation technical considerations

The preliminary optimisation studies presented here helped refining the technical considerations of the optimisation framework. The use of a surrogate optimisation framework allowed to find an optimum in a few days of simulation time on a standard desktop computer – once the initial data-set (several days or weeks) was simulated – instead of months or years.

In more detail, an initial sampling based on the Latin hypercube sampling method with 20 times the number of variables seemed to achieve reliable results for the subsequent surrogate modelling and to represent a good trade-off between computational time and model accuracy. The best-performing surrogate modelling technique was Kriging in all optimisation cases tested in this work (see also Appendix B.1 for a comparison with further surrogate modelling approaches); this is in line with previous use of this technique for computer model approximations [124, 150, 151]. However, an over-fitting of the surrogate model was observed when too many optimisation iterations were performed (cylindrical scaffold optimisation). Therefore, the number of optimisation loops needs to be carefully controlled, high enough to improve the accuracy around optimal points but not too high to avoid an over-fitting. In the optimisation cases presented here, the optimisation loop was run up to 10 times for the model accuracy improvement, and up to 10 times to improve the optimum. However, the optimum was often found in the first few iterations.

Regarding the optimisation, various (non-gradient-based) algorithms were tested that performed differently depending on each optimisation case. The PSO yielded the best optimums for the mixed loading cases, whereas the direct search was more beneficial for compression only. One of the main limitations of the PSO is that non-linear constraints cannot be taken into account (e.g. porosity constraint). In addition, both PSO and GA are stochastic algorithms whose performance can vary from one run to the next; on the contrary, the direct search is more controlled, but depends on the initial guess and might therefore lead to a local optimum [130]. Consequently, it might be worth checking different optimisation algorithms on a specific optimisation problem, as the optimisation phase is computationally less costly than the initial data-set simulations.

Lastly, the optimisation framework robustness was improved as it was particularly critical for the cylindrical scaffold optimisation: simulation or meshing errors were handled to avoid stopping the optimisation when one error happens; different (random) design points were suggested when an optimum was too close to an already tested design to ensure a good coverage of the design space and mitigate surrogate model over-fitting.

5.3.2 Optimal cubic scaffold designs

The cubic scaffold design optimised as a first step allowed to gain knowledge on the optimal technical specificities for the surrogate optimisation framework (see above) and on

the importance of adapting the number of variables to what is actually needed. Indeed, when comparing the graded to the non-graded designs under compression alone (4 vs. 2 variables), or the 7- and 4-variable graded designs under compression and bending, no great improvement of the optimal scaffold regenerative potential was achieved. However, adding more variables led to a much longer initial data-set simulation step.

Apart from these technical considerations, similar conclusions could be derived from the cubic scaffold geometrical optimisation as from the parametric study presented in Section 2.2.2. Not too large pores in the horizontal directions were more beneficial as they avoided too high deformation leading to fibrous tissue formation; while too small pores in the vertical direction impaired the cell infiltration process. Consequently, optimal designs had values very close to the ones found in the parametric study, around 0.7 mm for the horizontal pores and 0.8 mm for the vertical pores. The addition of bending reduced the healing potential of all scaffolds due to higher deformation; it also removed the symmetry of the design that was therefore making a greater use of the grading possibility (Tables 5.3 and 5.4). These results are in good agreement with a study by Boccaccio and colleagues who also found that grading was not beneficial under compression alone, but improved the bone regeneration potential under a shear load [82].

The layered cubic scaffold material optimisation suggested very different local optima, likely due to the large range of variations allowed for the variables (100 MPa to 100 GPa). It was therefore difficult to yield a general conclusion from these results. The only similarity between the optimums obtained by the different optimisation algorithms was that higher material properties were consistently needed in the middle layer of the scaffold. This could be explained by the higher strains produced there over the course of healing, as a small soft layer gets squeezed between layers of newly formed bone (that grow from the intact cortices). These results are further in line with another *in silico* study by Poh and colleagues where the scaffold porosity was optimised throughout a large defect: their optimum had higher porosity close to the extremities and lower porosity in the centre of the defect, what corresponds to lower and higher effective mechanical properties, respectively [108].

5.3.3   Optimal cylindrical scaffold designs

The study presented here is the first example of a 3D full-size scaffold design optimisation for a large bone defect using a validated mechanobiological computer model for bone regeneration. Two different cases were optimised, assuming a scaffold made of (1) titanium and (2) a soft material with Young's modulus similar to granulation tissue. Compared to the experimental softer honeycomb titanium scaffold (strut width = 1.2 mm) [13], both the porosity and the amount of regenerated bone in the optimal titanium scaffold pores were comparable: 84% porosity and 98% regenerated bone for the experimental scaffold predictions, compared to 85% porosity and 95% regenerated bone for the scaffold optimum. These results show that even with such a simple, regular initial scaffold geometry, a computer model can suggest designs that are performing as good as more complex designs.

Previous *in silico* scaffold design optimisation approaches have focused on the resulting bulk material properties [80, 86, 90, 95, 96, 99, 152]. Only a few studies used mechanobiological approaches to optimise scaffold design for bone regeneration. Boccaccio and colleagues

performed a number of studies on periodic scaffold unit cells to optimise the amount of tissue under bone-favouring stimulus right after implantation [70, 104, 105]. However, the results of Chapter 4 show that this approach does not ensure an actual better bone regeneration due to the dynamics of the healing process. Poh *et al* used a simplified bone regeneration model to optimise the 1D porosity distribution in a large defect scaffold and found that the optimal polymer-ceramic composite scaffold should have higher porosities close to the intact bone extremities and lower porosities in the middle of the defect [108]; however, their approach did not include the scaffold micro-architecture optimisation. Nevertheless, a similar trend was obtained here with the soft scaffold optimisation, where porosity was higher close to the intact bone extremities and very low in the centre of the defect; on the contrary, good graded titanium scaffolds showed higher porosity in the centre of the defect. The reason for it might be the need for a more strained environment to stimulate bone growth, as the use of titanium results in a stiff construct. Lastly, Wu and colleagues performed a time-dependent mechanobiological topology optimisation of a scaffold for a 2D large bone defect [109]. Although limited to 2D, their approach allowed a greater scaffold design freedom thanks to the topology optimisation approach. However, their bone regeneration model was derived from remodelling theories and did not include other cell types (chondrocytes, fibroblasts), thus making it less reliable in a defect regeneration context.

The sensitivity of the scaffold healing potential to the loading conditions was rather low, suggesting that the optimisation process is fairly robust to small loading condition variations. More importantly, this study suggests that un-loading of the patient's wounded limb is not necessarily wished (comparing Figure 5.5 c to a). Indeed, the standard loading (a) corresponds to peak load values under normal walking conditions; while a very reduced loading (c) decreased the regeneration potential due to greater bone resorption zones in the scaffold pores.

A tendency towards increased regenerated bone volume was found with increasing porosity in the initial data-set simulations for titanium scaffolds (Figure 5.4). However, similar porosities led to very different outcome, suggesting that the exact structure of the scaffold is more critical than the resulting macroscopic porosity. These results are in line with observations discussed in Chapter 4. On the contrary, the soft scaffolds showed a tendency for improved regenerated bone volume with lower porosity; in fact, for those designs, the Young's modulus was so low that the deformations were high, leading to fibrous tissue and cartilage formation. Consequently, the titanium optimal design, if made of that same soft material, would perform very badly and yield only 27% regenerated bone; an optimal scaffold design therefore strongly depends on the material used for the scaffold. Here, the optimal soft scaffold design was found to be far less porous than the optimal titanium scaffold, with very small pores in the centre of the defect and in the vertical direction; it yielded less regenerated bone than the optimal titanium scaffold (67% vs. 95%). This low porosity allowed to limit deformation but also to artificially increase the regenerated bone volume proportion. Thus, the optimal titanium scaffold pores were predicted to be filled with $3900\,mm^3$ bone compared to $700\,mm^3$ bone in the optimal soft scaffold pores. This observation suggests to consider the absolute value of regenerated bone as objective. In addition, so soft scaffolds have been shown not to be stable enough for bone regeneration applications when used alone. For instance, a collagen unstructured scaffold was implanted in rat large defects and was prone to mechanical failure or slipping out of the defect;

however, it showed a very good regeneration potential as it triggered endochondral ossification, the process by which cartilage is first deposited and then followed by bone mineralisation [37]. A solution to take advantage of such scaffolds while ensuring a proper mechanical stability might be to combine them with stiffer support structures.

5.3.4 Limitations and suggestions for future work

The approach described here included a series of limitations. First, the choice was made to use a surrogate optimisation approach and therefore to rely on a simplified relationship (surrogate model) between the input (scaffold design variables) and the output (regenerated bone volume in the scaffold pores). However, the surrogate model precision was assessed during the optimisation process for each new case. Next, the MBBR computer models used in both studies had limitations. For the cubic scaffold, the baseline bone healing model was used that was shown not to yield reliable results for scaffold-supported regeneration (e.g. lack of surface guidance); in addition, the geometry was not relevant for bone regeneration purposes. For the cylindrical scaffold, the geometry was closer to a long bone defect but still simplified (see Chapter 3 for further discussion on the assumptions made). In that case, the used MBBR model achieved good results for one experimental study (softer titanium scaffold) but not in another slightly different set-up (stiffer titanium scaffold with strut width 1.6 mm) (Chapter 3). Therefore, its prediction capability should be further assessed and improved for a broader range of scaffold designs to draw more reliable conclusions from the optimisation outcome.

In addition, no constraints were applied to the optimisation process with regards to the printability and producibility of the scaffold optimal designs, e.g. angles between successive layers of material or a minimal feature size. Such constraints have been taken into account in other scaffold design optimisation studies [89, 153]. Besides, a minimal porosity constraint was applied to the cubic scaffold but not the cylindrical scaffold and might be needed for biological requirements (proper re-vascularisation and nutrient supply).

Future work should further develop the more realistic scaffold design optimisation framework and possibly adapt it to a real-case scenario. It would be particularly valuable to interact with experimental studies to provide suggestions for improved scaffold design on the one hand, and gain more data to improve and validate the computer model predictions on the other. To envision the use of this computer framework in a more clinically relevant set-up, speed should be further improved by optimising the regeneration computer model. Lastly, combining a surrogate optimisation approach with topology optimisation would give more freedom in the scaffold design, as already performed in 2D by Wu *et al* [109]; however, topology optimisation relies on many variables and would likely require even higher computational times or other mathematical techniques to deal with the increased complexity.

<div style="text-align: right; font-size: 4em; color: #cccccc; font-weight: bold;">6</div>

Conclusions

6.1   Achievements and contribution to the field

Given a segmental large bone defect located in long bones (femur or tibia), the main research question of the thesis was to investigate what scaffold designs would best support the endogenous regeneration. Indeed, 3D-printed scaffolds are not the clinical gold standard so far because their design relies on trial-and-error approaches and the healing outcome is unknown *a priori* (Figure 6.1).

The first step of the thesis was the development and validation against experimental data of a computer model describing scaffold-supported large bone defect regeneration (Chapter 3). To do so, a previously existing fracture healing model was complemented to account for the specificities of large defects and scaffold presence. The predictive capability of the model was assessed against sheep studies using titanium scaffolds, a PCL-TCP scaffold and an empty large bone defect. The model could reproduce experimental results with a reasonable qualitative and quantitative agreement. More importantly, the features implemented in the model to achieve a good predictive capability revealed possible biological mechanisms at hand in scaffold-supported large bone defect regeneration. First, the importance of biological stimulation – or the lack thereof – was highlighted. In the absence of any stimulation (empty defect), strong cell activity reductions had to be hypothesised to reproduce the experimental observations; while certain scaffold material (TCP) or the presence of autologous bone graft (titanium scaffolds) increased the cell activity levels and ensured a better healing capacity. Second, surface guidance effects could explain the regeneration patterns observed *in vivo*, with both migration (unless over-ruled by ABG presence) and tissue deposition following existing tissue or scaffold surfaces. However, it remains to be elucidated why the internal fixation plate showed a good guidance capability in one case (PCL-TCP scaffold) but not in the other (titanium scaffolds).

The parametric studies performed on scaffolds derived from the PCL-TCP scaffold and on a simplified cubic scaffold revealed a large influence of design parameters such as strut and pore sizes and scaffold material properties on bone regeneration (Chapter 4). These parameters

Large bone defect

Scaffold implantation

Healing outcome?

Scaffold design parametric **optimisation** for maximal bone formation (Chapter 5)

?

Optimal designs: Porous stiff scaffolds and more bulky soft scaffolds

Scaffold-supported MBBR computer model (Chapter 3)

Comparison of different **scaffold designs** and **time horizons** (Chapter 4)

Scaffold design properties:
- Geometry: pore and strut sizes
- Material properties

Dynamics of the bone regeneration process: contrast between initial mechanics and bone regeneration predictions

Specific mechanisms revealed:
1. (Lack of) biological stimulation
2. Surface guidance effects

Figure 6.1 – Graphical abstract: starting from a large bone defect, healing could be predicted using an *in silico* model and the effects of different scaffold design parameters were investigated; lastly, a framework for parametric optimisation of a scaffold for a given defect was developed, to ensure maximal bone regeneration. Main findings are described in dark green.

influenced the healing outcome thanks to a more appropriate mechanical environment (more favourable mechanoregulation stimulus) over time, and/or locally larger surfaces allowing a faster cell migration and tissue deposition. In addition, the cubic scaffold systematic study confirmed the relevance of considering the complete dynamic regeneration process when designing a scaffold and not taking only the initial mechanical environment into account. We previously coined this principle as a multi-dynamic optimisation approach [84].

The last part of the thesis was dedicated to the implementation of a scaffold design parametric optimisation framework (Chapter 5). Because of the need to include the complete regeneration process, a surrogate optimisation approach was adopted that allowed to yield results in a reasonable, yet long, time (a few weeks including the initial data-set simulations). Results obtained for the various geometries revealed that the choice of design variables should be made carefully as more design variables did not necessarily yield a better healing outcome. The exact loading conditions applied on an optimal design had a rather limited impact, suggesting the optimum to be robust for imprecise loading conditions. Conversely, changing the material properties of the scaffold had a stark effect: the titanium optimal scaffold for a large bone defect was a very porous design, whereas assuming a much softer material resulted in a more bulky optimal design with smaller pores and thicker walls.

6.2 Computational efficiency

As a critical point for eventual applications in a clinical context, computational efficiency was consistently improved wherever possible in this thesis. The *in silico* models were based on simple geometries and did not include the vascularisation process. FE and lattice discretisations were relatively coarse, but still yielding reliable results according to preliminary results. The FEA frequency was reduced to remain accurate enough in depicting the callus material changes but decrease the simulation time needed. The choice of purely elastic instead of a poro-elastic analysis in some cases (PCL scaffold and cubic scaffolds) also led to a reduced computing time. For the PCL scaffold, using a material pooling to describe the elements in the callus was necessary to obtain a reasonable simulation time (1 day instead of 10). In addition, small optimisation of the C++ code were performed, in particular in the way to browse elements randomly to ensure no bias in the simulations while keeping them fast.

In the optimisation process, the choice of a surrogate modelling strategy was dictated by computational efficiency; proper definition of the design variables was also necessary to avoid too costly initial runs and unreliable optimisation outcome.

However, despite these improvements, the computer code is still not fast enough for clinical applications. Future work should focus on systematically improving the code, further simplifying the models and making a broader use of parallel computing possibilities.

6.3 Recommendations for future work

The focus of this work was put on sheep lower limb long bones with critical-sized segmental defects. However, the principles and developed computational framework could be extended and adapted to any type of bone and any species – in particular for human clinical purpose,

provided that the healing mechanoregulation is known. Such a framework could be employed in a personalised medicine approach if the specific healing potential of an individual is known (e.g. influenced by factors such as smoking, diabetes, etc.).

Future work should aim at tackling the limitations of this thesis. With regards to scaffold-supported large bone defect regeneration, the computer model could be further complemented to improve its predictive capability. In particular, it failed at describing the stiff titanium scaffold results, suggesting that more mechanics-dependent behaviours should be taken into account (e.g. cell migration, proliferation or differentiation rates). Besides, further comparisons to *in vivo* studies would improve the confidence in the model predictions and ensure more general predictive capabilities, not fitted to a specific experimental case. Additional behaviours such as bone remodelling and scaffold degradation behaviour should be integrated to ensure a global understanding of the regeneration process.

Further parametric studies should investigate other design variables and other types of scaffold designs (e.g. comparing different scaffold architectures); ideally, these should also be compared to some experimental data to ensure the reliability of the conclusions. Thus, the computer framework could help extrapolating results from an experimental study to similar scaffold designs.

Future work should aim at applying the optimisation framework to realistic geometries, based on experimental or clinical cases. Despite the afore-mentioned computational efficiency issues, such work would help designing scaffolds with higher healing potential and reduce the amount of experimental studies. Ideally, this computer modelling work should be performed alongside with experiments to improve knowledge on both sides: focusing on most promising scaffold designs on the one hand and improving the knowledge and model predictive capability on the other. For that purpose, a more integrated and user-friendly interface of the computer model would be a great asset for eventual clinical applications.

In addition, sensitivity of the optimisation process to the loading conditions, the geometry of the defect and the choice of design variables should be performed to better understand the outcome of the optimisation process and evaluate its robustness to uncertainties. In particular, this would help assessing the reliability of the suggested optimums and their range of use. Scaffold degradation behaviour could be incorporated in the optimisation framework and thus include a further dynamic effect in the regeneration process.

Besides, additional constraints should be implemented for the scaffold optimisation process, e.g. related to the production of the scaffold or biological requirements. These could include constraints on the geometry to ensure that the scaffold is printable by the chosen production technique; and inter-connectivity of the pores, minimal porosity or minimal pore size constraints to allow a good re-vascularisation and nutrient supply inside the scaffold pores.

In a later step, topology optimisation approaches could be developed, as they would allow a more complete freedom of design for the bone scaffold. However, the coupling of topology optimisation technique with a stochastic bone regeneration computer model would likely yield very complex mathematical questions and even higher computation times.

References

[1] C. Schlundt, C. H. Bucher, S. Tsitsilonis, H. Schell, G. N. Duda, and K. Schmidt-Bleek, « Clinical and Research Approaches to Treat Non-union Fracture », *Current Osteoporosis Reports*, vol. 16, no. 2, pp. 155–168, Apr. 2018, ISSN: 1544-2241. DOI: 10.1007/s11914-018-0432-1.

[2] T. A. Einhorn, « Enhancement of fracture-healing. », *JBJS*, vol. 77, no. 6, pp. 940–956, Jun. 1995, ISSN: 0021-9355.

[3] C. G. Finkemeier, « Bone-Grafting and Bone-Graft Substitutes », *The Journal of Bone & Joint Surgery*, vol. 84, no. 3, pp. 454–464, Mar. 2002, ISSN: 0021-9355.

[4] T. T. Roberts and A. J. Rosenbaum, « Bone grafts, bone substitutes and orthobiologics », *Organogenesis*, vol. 8, no. 4, pp. 114–124, Oct. 2012, ISSN: 1547-6278. DOI: 10.4161/org.23306.

[5] R. Dimitriou, G. I. Mataliotakis, A. G. Angoules, N. K. Kanakaris, and P. V. Giannoudis, « Complications following autologous bone graft harvesting from the iliac crest and using the RIA: A systematic review », *Injury*, vol. 42, S3–S15, Sep. 2011, ISSN: 00201383. DOI: 10.1016/j.injury.2011.06.015.

[6] E. Roddy, M. R. DeBaun, A. Daoud-Gray, Y. P. Yang, and M. J. Gardner, « Treatment of critical-sized bone defects: clinical and tissue engineering perspectives », *European Journal of Orthopaedic Surgery & Traumatology*, vol. 28, no. 3, pp. 351–362, Apr. 2018, ISSN: 1432-1068. DOI: 10.1007/s00590-017-2063-0.

[7] M. C. Kruyt, W. J. A. Dhert, C. Oner, C. A. van Blitterswijk, A. J. Verbout, and J. D. de Bruijn, « Optimization of bone-tissue engineering in goats », *Journal of Biomedical Materials Research Part B: Applied Biomaterials*, vol. 69B, no. 2, pp. 113–120, 2004, ISSN: 1552-4981. DOI: 10.1002/jbm.b.10073.

[8] R. W. Lindsey, Z. Gugala, E. Milne, M. Sun, F. H. Gannon, and L. L. Latta, « The efficacy of cylindrical titanium mesh cage for the reconstruction of a critical-size canine segmental femoral diaphyseal defect », *Journal of Orthopaedic Research*, vol. 24, no. 7, pp. 1438–1453, Jul. 2006, ISSN: 1554-527X. DOI: 10.1002/jor.20154.

[9] J. C. Reichert, A. Cipitria, D. R. Epari, S. Saifzadeh, P. Krishnakanth, A. Berner, M. A. Woodruff, H. Schell, M. Mehta, M. A. Schuetz, G. N. Duda, and D. W. Hutmacher, « A Tissue Engineering Solution for Segmental Defect Regeneration in Load-Bearing Long Bones », *Science Translational Medicine*, vol. 4, no. 141, 141ra93, Jul. 2012, ISSN: 1946-6234, 1946-6242. DOI: 10.1126/scitranslmed.3003720.

[10] J. V. der Stok, O. P. V. der Jagt, S. A. Yavari, M. F. P. D. Haas, J. H. Waarsing, H. Jahr, E. M. M. V. Lieshout, P. Patka, J. A. N. Verhaar, A. A. Zadpoor, and H. Weinans, « Selective laser melting-produced porous titanium scaffolds regenerate bone in critical size cortical bone defects », *Journal of Orthopaedic Research*, vol. 31, no. 5, pp. 792–799, 2013, ISSN: 1554-527X. DOI: `10.1002/jor.22293`.

[11] G. Li, L. Wang, W. Pan, F. Yang, W. Jiang, X. Wu, X. Kong, K. Dai, and Y. Hao, « In vitro and in vivo study of additive manufactured porous Ti6Al4V scaffolds for repairing bone defects », *Scientific Reports*, vol. 6, p. 34 072, Sep. 2016, ISSN: 2045-2322. DOI: `10.1038/srep34072`.

[12] A. B. Lovati, S. Lopa, C. Recordati, G. Talo, C. Turrisi, M. Bottagisio, M. Losa, E. Scanziani, and M. Moretti, « In Vivo Bone Formation Within Engineered Hydroxyapatite Scaffolds in a Sheep Model », *Calcified Tissue International*, vol. 99, no. 2, pp. 209–223, Aug. 2016, ISSN: 0171-967X. DOI: `10.1007/s00223-016-0140-8`.

[13] A.-M. Pobloth, S. Checa, H. Razi, A. Petersen, J. C. Weaver, K. Schmidt-Bleek, M. Windolf, A. Á. Tatai, C. P. Roth, K.-D. Schaser, G. N. Duda, and P. Schwabe, « Mechanobiologically optimized 3D titanium-mesh scaffolds enhance bone regeneration in critical segmental defects in sheep », *Science Translational Medicine*, vol. 10, no. 423, eaam8828, Jan. 2018, ISSN: 1946-6234, 1946-6242. DOI: `10.1126/scitranslmed.aam8828`.

[14] N. Reznikov, O. R. Boughton, S. Ghouse, A. E. Weston, L. Collinson, G. W. Blunn, J. R. T. Jeffers, J. P. Cobb, and M. M. Stevens, « Individual response variations in scaffold-guided bone regeneration are determined by independent strain- and injury-induced mechanisms », *Biomaterials*, vol. 194, pp. 183–194, Feb. 2019, ISSN: 0142-9612. DOI: `10.1016/j.biomaterials.2018.11.026`.

[15] A. M. Crovace, L. Lacitignola, D. M. Forleo, F. Staffieri, E. Francioso, A. Di Meo, J. Becerra, A. Crovace, and L. Santos-Ruiz, « 3D Biomimetic Porous Titanium (Ti6Al4V ELI) Scaffolds for Large Bone Critical Defect Reconstruction: An Experimental Study in Sheep », *Animals*, vol. 10, no. 8, p. 1389, Aug. 2020, ISSN: 2076-2615. DOI: `10.3390/ani10081389`.

[16] F. A. Shah, O. Omar, F. Suska, A. Snis, A. Matic, L. Emanuelsson, B. Norlindh, J. Lausmaa, P. Thomsen, and A. Palmquist, « Long-term osseointegration of 3D printed CoCr constructs with an interconnected open-pore architecture prepared by electron beam melting », *Acta Biomaterialia*, vol. 36, pp. 296–309, May 2016, ISSN: 1742-7061. DOI: `10.1016/j.actbio.2016.03.033`.

[17] H. Eftekhari, A. Jahandideh, A. Asghari, A. Akbarzadeh, and S. Hesaraki, « Assessment of polycaprolacton (PCL) nanocomposite scaffold compared with hydroxyapatite (HA) on healing of segmental femur bone defect in rabbits », *Artificial Cells, Nanomedicine, and Biotechnology*, vol. 45, no. 5, pp. 961–968, Jul. 2017, ISSN: 2169-1401. DOI: `10.1080/21691401.2016.1198360`.

[18] A. Entezari, I. Roohani, G. Li, C. R. Dunstan, P. Rognon, Q. Li, X. Jiang, and H. Zreiqat, « Architectural Design of 3D Printed Scaffolds Controls the Volume and Functionality of Newly Formed Bone », *Advanced Healthcare Materials*, vol. 8, no. 1, p. 1 801 353, 2019, ISSN: 2192-2659. DOI: `10.1002/adhm.201801353`.

[19] C. M. Murphy, M. G. Haugh, and F. J. O'Brien, « The effect of mean pore size on cell attachment, proliferation and migration in collagen–glycosaminoglycan scaffolds for bone tissue engineering », *Biomaterials*, vol. 31, no. 3, pp. 461–466, Jan. 2010, ISSN: 0142-9612. DOI: `10.1016/j.biomaterials.2009.09.063`.

[20] S. Bose, M. Roy, and A. Bandyopadhyay, « Recent advances in bone tissue engineering scaffolds », *Trends in Biotechnology*, vol. 30, no. 10, pp. 546–554, Oct. 2012, ISSN: 0167-7799. DOI: `10.1016/j.tibtech.2012.07.005`.

[21] N. Abbasi, S. Hamlet, R. M. Love, and N.-T. Nguyen, « Porous scaffolds for bone regeneration », *Journal of Science: Advanced Materials and Devices*, vol. 5, no. 1, pp. 1–9, Mar. 2020, ISSN: 2468-2179. DOI: `10.1016/j.jsamd.2020.01.007`.

[22] P. Lichte, H. C. Pape, T. Pufe, P. Kobbe, and H. Fischer, « Scaffolds for bone healing: Concepts, materials and evidence », *Injury*, Bone Regeneration in the 21st Century, vol. 42, no. 6, pp. 569–573, Jun. 2011, ISSN: 0020-1383. DOI: `10.1016/j.injury.2011.03.033`.

[23] J. C. Reichert, M. E. Wullschleger, A. Cipitria, J. Lienau, T. K. Cheng, M. A. Schütz, G. N. Duda, U. Nöth, J. Eulert, and D. W. Hutmacher, « Custom-made composite scaffolds for segmental defect repair in long bones », *International Orthopaedics*, vol. 35, no. 8, pp. 1229–1236, Aug. 2011, ISSN: 0341-2695. DOI: `10.1007/s00264-010-1146-x`.

[24] K. Palka and R. Pokrowiecki, « Porous Titanium Implants: A Review », *Advanced Engineering Materials*, vol. 20, no. 5, p. 1 700 648, May 2018, ISSN: 1438-1656. DOI: `10.1002/adem.201700648`.

[25] M. Ramu, M. Ananthasubramanian, T. Kumaresan, R. Gandhinathan, and S. Jothi, « Optimization of the configuration of porous bone scaffolds made of polyamide/hydroxyapatite composites using selective laser sintering for tissue engineering applications », *Bio-Medical Materials and Engineering*, Sep. 2018, ISSN: 1878-3619. DOI: `10.3233/BME-181020`.

[26] K. Schmidt-Bleek, A. Petersen, A. Dienelt, C. Schwarz, and G. N. Duda, « Initiation and early control of tissue regeneration – bone healing as a model system for tissue regeneration », *Expert Opinion on Biological Therapy*, vol. 14, no. 2, pp. 247–259, Feb. 2014, ISSN: 1471-2598. DOI: `10.1517/14712598.2014.857653`.

[27] I. H. Kalfas, « Principles of bone healing », *Neurosurgical Focus*, vol. 10, no. 4, pp. 1–4, Apr. 2001. DOI: `10.3171/foc.2001.10.4.2`.

[28] R. Marsell and T. A. Einhorn, « The biology of fracture healing », *Injury*, Bone Regeneration in the 21st Century, vol. 42, no. 6, pp. 551–555, Jun. 2011, ISSN: 0020-1383. DOI: `10.1016/j.injury.2011.03.031`.

REFERENCES

[29] J. Wolff, *Das Gesetz der Transformation der Knochen*, 1. Aufl.; Reprint der Ausg. Berlin, 1892 / Hrsg.: Georg Bergmann. Berlin: Pro Business, 2010, ISBN: 978-3-86805-648-8.

[30] R. Huiskes, W. D. Van Driel, P. J. Prendergast, and K. Søballe, « A biomechanical regulatory model for periprosthetic fibrous-tissue differentiation », *Journal of Materials Science. Materials in Medicine*, vol. 8, no. 12, pp. 785–788, Dec. 1997, ISSN: 0957-4530.

[31] D. R. Carter, G. S. Beaupré, N. J. Giori, and J. A. Helms, « Mechanobiology of skeletal regeneration », *Clinical Orthopaedics and Related Research*, no. 355 Suppl, S41–55, Oct. 1998, ISSN: 0009-921X.

[32] L. E. Claes and C. A. Heigele, « Magnitudes of local stress and strain along bony surfaces predict the course and type of fracture healing », *Journal of Biomechanics*, vol. 32, no. 3, pp. 255–266, Mar. 1999, ISSN: 0021-9290. DOI: `10.1016/S0021-9290(98)00153-5`.

[33] S. Checa, P. J. Prendergast, and G. N. Duda, « Inter-species investigation of the mechano-regulation of bone healing: Comparison of secondary bone healing in sheep and rat », *Journal of Biomechanics*, vol. 44, no. 7, pp. 1237–1245, Apr. 2011, ISSN: 0021-9290. DOI: `10.1016/j.jbiomech.2011.02.074`.

[34] D. Lacroix and P. J. Prendergast, « A mechano-regulation model for tissue differentiation during fracture healing: analysis of gap size and loading », *Journal of Biomechanics*, vol. 35, no. 9, pp. 1163–1171, Sep. 2002, ISSN: 0021-9290. DOI: `10.1016/S0021-9290(02)00086-6`.

[35] J. F. Keating, A. H. R. W. Simpson, and C. M. Robinson, « The management of fractures with bone loss », *The Journal of Bone and Joint Surgery. British volume*, vol. 87-B, no. 2, pp. 142–150, Feb. 2005, ISSN: 0301-620X. DOI: `10.1302/0301-620X.87B2.15874`.

[36] H. Bezstarosti, W. J. Metsemakers, E. M. M. van Lieshout, L. W. Voskamp, K. Kortram, M. A. McNally, L. C. Marais, and M. H. J. Verhofstad, « Management of critical-sized bone defects in the treatment of fracture-related infection: a systematic review and pooled analysis », *Archives of Orthopaedic and Trauma Surgery*, Aug. 2020, ISSN: 1434-3916. DOI: `10.1007/s00402-020-03525-0`.

[37] A. Petersen, A. Princ, G. Korus, A. Ellinghaus, H. Leemhuis, A. Herrera, A. Klaumünzer, S. Schreivogel, A. Woloszyk, K. Schmidt-Bleek, S. Geissler, I. Heschel, and G. N. Duda, « A biomaterial with a channel-like pore architecture induces endochondral healing of bone defects », *Nature Communications*, vol. 9, no. 1, p. 4430, Oct. 2018, ISSN: 2041-1723. DOI: `10.1038/s41467-018-06504-7`.

[38] E. J. Woo, « Adverse Events After Recombinant Human BMP2 in Nonspinal Orthopaedic Procedures », *Clinical Orthopaedics & Related Research*, vol. 471, no. 5, pp. 1707–1711, May 2013, ISSN: 0009-921X. DOI: `10.1007/s11999-012-2684-x`.

[39] P. V. Giannoudis, T. A. Einhorn, G. Schmidmaier, and D. Marsh, « The diamond concept – open questions », *Injury*, 5th European Symposium on Tissue Engineering: Bone Biology Congress 2008, vol. 39, S5–S8, Sep. 2008, ISSN: 0020-1383. DOI: `10.1016/S0020-1383(08)70010-X`.

[40] L. Polo-Corrales, M. Latorre-Esteves, and J. E. Ramirez-Vick, « Scaffold Design for Bone Regeneration », *Journal of nanoscience and nanotechnology*, vol. 14, no. 1, pp. 15–56, Jan. 2014, ISSN: 1533-4880.

[41] R. J. O'Keefe and J. Mao, « Bone Tissue Engineering and Regeneration: From Discovery to the Clinic—An Overview », *Tissue Engineering Part B: Reviews*, vol. 17, no. 6, pp. 389–392, Sep. 2011, ISSN: 1937-3368. DOI: `10.1089/ten.teb.2011.0475`.

[42] A. Cipitria, C. Lange, H. Schell, W. Wagermaier, J. C. Reichert, D. W. Hutmacher, P. Fratzl, and G. N. Duda, « Porous scaffold architecture guides tissue formation », *Journal of Bone and Mineral Research*, vol. 27, no. 6, pp. 1275–1288, Jun. 2012, ISSN: 08840431. DOI: `10.1002/jbmr.1589`.

[43] A. Berner, M. A. Woodruff, C. X. F. Lam, M. T. Arafat, S. Saifzadeh, R. Steck, J. Ren, M. Nerlich, A. K. Ekaputra, I. Gibson, and D. W. Hutmacher, « Effects of scaffold architecture on cranial bone healing », *International Journal of Oral and Maxillofacial Surgery*, vol. 43, no. 4, pp. 506–513, Apr. 2014, ISSN: 0901-5027. DOI: `10.1016/j.ijom.2013.05.008`.

[44] M. Kellomäki, H. Niiranen, K. Puumanen, N. Ashammakhi, T. Waris, and P. Törmälä, « Bioabsorbable scaffolds for guided bone regeneration and generation », *Biomaterials*, Orthopaedic Polymeric Biomaterials: Applications of Biodegradables, vol. 21, no. 24, pp. 2495–2505, Dec. 2000, ISSN: 0142-9612. DOI: `10.1016/S0142-9612(00)00117-4`.

[45] B. G. Sengers, M. Taylor, C. P. Please, and R. O. Oreffo, « Computational modelling of cell spreading and tissue regeneration in porous scaffolds », *Biomaterials*, vol. 28, no. 10, pp. 1926–1940, Apr. 2007, ISSN: 01429612. DOI: `10.1016/j.biomaterials.2006.12.008`.

[46] M. Werner, N. A. Kurniawan, G. Korus, C. V. C. Bouten, and A. Petersen, « Mesoscale substrate curvature overrules nanoscale contact guidance to direct bone marrow stromal cell migration », *Journal of The Royal Society Interface*, vol. 15, no. 145, p. 20 180 162, Aug. 2018. DOI: `10.1098/rsif.2018.0162`.

[47] H. Isaksson, C. C. van Donkelaar, R. Huiskes, and K. Ito, « Corroboration of mechanoregulatory algorithms for tissue differentiation during fracture healing: comparison with in vivo results », *Journal of Orthopaedic Research*, vol. 24, no. 5, pp. 898–907, May 2006, ISSN: 1554-527X. DOI: `10.1002/jor.20118`.

[48] E. Borgiani, G. N. Duda, and S. Checa, « Multiscale Modeling of Bone Healing: Toward a Systems Biology Approach », *Frontiers in Physiology*, vol. 8, May 2017, ISSN: 1664-042X. DOI: `10.3389/fphys.2017.00287`.

[49] E. Borgiani, G. Duda, B. Willie, and S. Checa, « Bone healing in mice: does it follow generic mechano-regulation rules? », *Facta Universitatis, Series: Mechanical Engineering*, vol. 13, no. 3, pp. 217–227, Dec. 2015, ISSN: 2335-0164.

REFERENCES

[50] D. Lacroix, P. J. Prendergast, G. Li, and D. Marsh, « Biomechanical model to simulate tissue differentiation and bone regeneration: Application to fracture healing », *Medical and Biological Engineering and Computing*, vol. 40, no. 1, pp. 14–21, Jan. 2002, ISSN: 1741-0444. DOI: 10.1007/BF02347690.

[51] J. A. Sanz-Herrera, J. M. Garcia-Aznar, and M. Doblare, « A mathematical model for bone tissue regeneration inside a specific type of scaffold », *Biomechanics and Modeling in Mechanobiology*, vol. 7, no. 5, pp. 355–366, Oct. 2008, ISSN: 1617-7940. DOI: 10.1007/s10237-007-0089-7.

[52] X. Sun, Y. Kang, J. Bao, Y. Zhang, Y. Yang, and X. Zhou, « Modeling vascularized bone regeneration within a porous biodegradable CaP scaffold loaded with growth factors », *Biomaterials*, vol. 34, no. 21, pp. 4971–4981, Jul. 2013, ISSN: 0142-9612. DOI: 10.1016/j.biomaterials.2013.03.015.

[53] S. R. Moore, G. M. Saidel, U. Knothe, and M. L. K. Tate, « Mechanistic, Mathematical Model to Predict the Dynamics of Tissue Genesis in Bone Defects via Mechanical Feedback and Mediation of Biochemical Factors », *PLOS Computational Biology*, vol. 10, no. 6, e1003604, Jun. 2014, ISSN: 1553-7358. DOI: 10.1371/journal.pcbi.1003604.

[54] E. Borgiani, « Multiscale in silico model to investigate compromised bone healing conditions », 2020. DOI: 10.14279/DEPOSITONCE-10604.

[55] L. Wang, Q. Shi, Y. Cai, Q. Chen, X. Guo, and Z. Li, « Mechanical–chemical coupled modeling of bone regeneration within a biodegradable polymer scaffold loaded with VEGF », *Biomechanics and Modeling in Mechanobiology*, Jun. 2020, ISSN: 1617-7940. DOI: 10.1007/s10237-020-01339-y.

[56] L. Geris, A. Gerisch, J. V. Sloten, R. Weiner, and H. V. Oosterwyck, « Angiogenesis in bone fracture healing: A bioregulatory model », *Journal of Theoretical Biology*, vol. 251, no. 1, pp. 137–158, Mar. 2008, ISSN: 0022-5193. DOI: 10.1016/j.jtbi.2007.11.008.

[57] S. Checa and P. J. Prendergast, « A Mechanobiological Model for Tissue Differentiation that Includes Angiogenesis: A Lattice-Based Modeling Approach », *Annals of Biomedical Engineering*, vol. 37, no. 1, pp. 129–145, Jan. 2009, ISSN: 1573-9686. DOI: 10.1007/s10439-008-9594-9.

[58] C. Sandino, S. Checa, P. J. Prendergast, and D. Lacroix, « Simulation of angiogenesis and cell differentiation in a CaP scaffold subjected to compressive strains using a lattice modeling approach », *Biomaterials*, vol. 31, no. 8, pp. 2446–2452, Mar. 2010, ISSN: 0142-9612. DOI: 10.1016/j.biomaterials.2009.11.063.

[59] M. W. Laschke, Y. Harder, M. Amon, I. Martin, J. Farhadi, A. Ring, N. Torio-Padron, R. Schramm, M. Rücker, D. Junker, J. M. Häufel, C. Carvalho, M. Heberer, G. Germann, B. Vollmar, and M. D. Menger, « Angiogenesis in Tissue Engineering: Breathing Life into Constructed Tissue Substitutes », *Tissue Engineering*, vol. 12, no. 8, pp. 2093–2104, Aug. 2006, ISSN: 1076-3279. DOI: 10.1089/ten.2006.12.2093.

[60] S. Stratton, N. B. Shelke, K. Hoshino, S. Rudraiah, and S. G. Kumbar, « Bioactive polymeric scaffolds for tissue engineering », *Bioactive Materials*, vol. 1, no. 2, pp. 93–108, Dec. 2016, ISSN: 2452-199X. DOI: 10.1016/j.bioactmat.2016.11.001.

[61] M. Bienert, « Angiogenesis in Bone Tissue Engineering », *Journal of Stem Cell Research and Medicine*, vol. 4, no. 1, 2019, ISSN: 23986530. DOI: 10.15761/JSCRM.1000129.

[62] R. Huiskes, H. Weinans, and B. van Rietbergen, « The relationship between stress shielding and bone resorption around total hip stems and the effects of flexible materials », *Clinical Orthopaedics and Related Research*, pp. 124–134, Jan. 1992, ISSN: 0009921X.

[63] H. Weinans, R. Huiskes, and H. J. Grootenboer, « Effects of material properties of femoral hip components on bone remodeling », *Journal of Orthopaedic Research*, vol. 10, no. 6, pp. 845–853, 1992, ISSN: 1554-527X. DOI: 10.1002/jor.1100100614.

[64] M. Doblaré, J. García, and J. Cegoñino, « Development of an Internal Bone Remodelling Theory and Applications to Some Problems in Orthopaedic Biomechanics », *Meccanica*, vol. 37, no. 4, pp. 365–374, Jul. 2002, ISSN: 1572-9648. DOI: 10.1023/A:1020835720405.

[65] J. M. García, M. Doblaré, and J. Cegoñino, « Bone remodelling simulation: a tool for implant design », *Computational Materials Science*, vol. 25, no. 1, pp. 100–114, Sep. 2002, ISSN: 0927-0256. DOI: 10.1016/S0927-0256(02)00254-9.

[66] D. P. Byrne, D. Lacroix, J. A. Planell, D. J. Kelly, and P. J. Prendergast, « Simulation of tissue differentiation in a scaffold as a function of porosity, Young's modulus and dissolution rate: Application of mechanobiological models in tissue engineering », *Biomaterials*, vol. 28, no. 36, pp. 5544–5554, Dec. 2007, ISSN: 0142-9612. DOI: 10.1016/j.biomaterials.2007.09.003.

[67] S. Checa and P. J. Prendergast, « Effect of cell seeding and mechanical loading on vascularization and tissue formation inside a scaffold: A mechano-biological model using a lattice approach to simulate cell activity », *Journal of Biomechanics*, vol. 43, no. 5, pp. 961–968, Mar. 2010, ISSN: 0021-9290. DOI: 10.1016/j.jbiomech.2009.10.044.

[68] L. Liu, Q. Shi, Q. Chen, and Z. Li, « Mathematical modeling of bone in-growth into undegradable porous periodic scaffolds under mechanical stimulus », *Journal of Tissue Engineering*, vol. 10, p. 2 041 731 419 827 167, Jan. 2019, ISSN: 2041-7314. DOI: 10.1177/2041731419827167.

[69] M. Bashkuev, S. Checa, S. Postigo, G. Duda, and H. Schmidt, « Computational analyses of different intervertebral cages for lumbar spinal fusion », *Journal of Biomechanics*, vol. 48, no. 12, pp. 3274–3282, Sep. 2015, ISSN: 1873-2380. DOI: 10.1016/j.jbiomech.2015.06.024.

[70] A. Boccaccio, A. E. Uva, M. Fiorentino, L. Lamberti, and G. Monno, « A Mechanobiology-based Algorithm to Optimize the Microstructure Geometry of Bone Tissue Scaffolds », *International Journal of Biological Sciences*, vol. 12, no. 1, pp. 1–17, Jan. 2016, ISSN: 1449-2288. DOI: 10.7150/ijbs.13158.

REFERENCES

[71]   M. Schmitt, R. Allena, T. Schouman, S. Frasca, J. M. Collombet, X. Holy, and P. Rouch, « Diffusion model to describe osteogenesis within a porous titanium scaffold », *Computer Methods in Biomechanics and Biomedical Engineering*, vol. 19, no. 2, pp. 171–179, Jan. 2016, ISSN: 1025-5842. DOI: 10.1080/10255842.2014.998207.

[72]   M. Paris, A. Götz, I. Hettrich, C. M. Bidan, J. W. C. Dunlop, H. Razi, I. Zizak, D. W. Hutmacher, P. Fratzl, G. N. Duda, W. Wagermaier, and A. Cipitria, « Scaffold curvature-mediated novel biomineralization process originates a continuous soft tissue-to-bone interface », *Acta Biomaterialia*, vol. 60, pp. 64–80, Sep. 2017, ISSN: 1742-7061. DOI: 10.1016/j.actbio.2017.07.029.

[73]   V. S. Cheong, P. Fromme, A. Mumith, M. J. Coathup, and G. W. Blunn, « Novel adaptive finite element algorithms to predict bone ingrowth in additive manufactured porous implants », *Journal of the Mechanical Behavior of Biomedical Materials*, vol. 87, pp. 230–239, Nov. 2018, ISSN: 1751-6161. DOI: 10.1016/j.jmbbm.2018.07.019.

[74]   M. Mehta, H. Schell, C. Schwarz, A. Peters, K. Schmidt-Bleek, A. Ellinghaus, H. J. Bail, G. N. Duda, and J. Lienau, « A 5-mm femoral defect in female but not in male rats leads to a reproducible atrophic non-union », *Archives of Orthopaedic and Trauma Surgery*, vol. 131, no. 1, pp. 121–129, Jan. 2011, ISSN: 1434-3916. DOI: 10.1007/s00402-010-1155-7.

[75]   V. Viateau, G. Guillemin, V. Bousson, K. Oudina, D. Hannouche, L. Sedel, D. Logeart-Avramoglou, and H. Petite, « Long-bone critical-size defects treated with tissue-engineered grafts: A study on sheep », *Journal of Orthopaedic Research*, vol. 25, no. 6, pp. 741–749, 2007, ISSN: 1554-527X. DOI: 10.1002/jor.20352.

[76]   A. Cipitria, W. Wagermaier, P. Zaslansky, H. Schell, J. C. Reichert, P. Fratzl, D. W. Hutmacher, and G. N. Duda, « BMP delivery complements the guiding effect of scaffold architecture without altering bone microstructure in critical-sized long bone defects: A multiscale analysis », *Acta Biomaterialia*, vol. 23, pp. 282–294, Sep. 2015, ISSN: 1742-7061. DOI: 10.1016/j.actbio.2015.05.015.

[77]   L. Zhang, M. Qiao, H. Gao, B. Hu, H. Tan, X. Zhou, and C. M. Li, « Investigation of mechanism of bone regeneration in a porous biodegradable calcium phosphate (CaP) scaffold by a combination of a multi-scale agent-based model and experimental optimization/validation », *Nanoscale*, vol. 8, no. 31, pp. 14 877–14 887, 2016, ISSN: 2040-3364. DOI: 10.1039/c6nr01637e.

[78]   J. A. Sanz-Herrera, J. M. García-Aznar, and M. Doblaré, « On scaffold designing for bone regeneration: A computational multiscale approach », *Acta Biomaterialia*, vol. 5, no. 1, pp. 219–229, Jan. 2009, ISSN: 1742-7061. DOI: 10.1016/j.actbio.2008.06.021.

[79]   K. Saitou, K. Izui, S. Nishiwaki, and P. Papalambros, « A Survey of Structural Optimization in Mechanical Product Development », *Journal of Computing and Information Science in Engineering*, vol. 5, no. 3, pp. 214–226, Sep. 2005, ISSN: 1530-9827. DOI: 10.1115/1.2013290.

[80]   S. J. Hollister, R. D. Maddox, and J. M. Taboas, « Optimal design and fabrication of scaffolds to mimic tissue properties and satisfy biological constraints », *Biomaterials*, vol. 23, no. 20, pp. 4095–4103, Oct. 2002, ISSN: 0142-9612. DOI: `10.1016/S0142-9612(02)00148-5`.

[81]   J. Wieding, A. Wolf, and R. Bader, « Numerical optimization of open-porous bone scaffold structures to match the elastic properties of human cortical bone », *Journal of the Mechanical Behavior of Biomedical Materials*, vol. 37, pp. 56–68, Sep. 2014, ISSN: 1751-6161. DOI: `10.1016/j.jmbbm.2014.05.002`.

[82]   A. Boccaccio, A. E. Uva, M. Fiorentino, G. Mori, and G. Monno, « Geometry Design Optimization of Functionally Graded Scaffolds for Bone Tissue Engineering: A Mechanobiological Approach », *PLOS ONE*, vol. 11, no. 1, e0146935, Jan. 2016, ISSN: 1932-6203. DOI: `10.1371/journal.pone.0146935`.

[83]   X. Wang, S. Xu, S. Zhou, W. Xu, M. Leary, P. Choong, M. Qian, M. Brandt, and Y. M. Xie, « Topological design and additive manufacturing of porous metals for bone scaffolds and orthopaedic implants: A review », *Biomaterials*, vol. 83, pp. 127–141, Mar. 2016, ISSN: 0142-9612. DOI: `10.1016/j.biomaterials.2016.01.012`.

[84]   C. Metz, G. N. Duda, and S. Checa, « Towards multi-dynamic mechano-biological optimization of 3D-printed scaffolds to foster bone regeneration », *Acta Biomaterialia*, vol. 101, pp. 117–127, Jan. 2020, ISSN: 1742-7061. DOI: `10.1016/j.actbio.2019.10.029`.

[85]   *Topology Optimization Theory, Methods, and Applications.* Berlin, Heidelberg: Springer Berlin Heidelberg, 2004, ISBN: 978-3-662-05086-6.

[86]   N. Uth, J. Mueller, B. Smucker, and A.-M. Yousefi, « Validation of scaffold design optimization in bone tissue engineering: finite element modeling versus designed experiments », *Biofabrication*, vol. 9, no. 1, p. 015 023, Feb. 2017, ISSN: 1758-5090. DOI: `10.1088/1758-5090/9/1/015023`.

[87]   C.-Y. Lin, C.-C. Hsiao, P.-Q. Chen, and S. J. Hollister, « Interbody Fusion Cage Design Using Integrated Global Layout and Local Microstructure Topology Optimization », *Spine*, vol. 29, no. 16, pp. 1747–1754, Aug. 2004, ISSN: 0362-2436. DOI: `10.1097/01.BRS.0000134573.14150.1A`.

[88]   H. G. Chuah, I. A. Rahim, and M. I. Yusof, « Topology optimisation of spinal interbody cage for reducing stress shielding effect », *Computer Methods in Biomechanics and Biomedical Engineering*, vol. 13, no. 3, pp. 319–326, Jun. 2010, ISSN: 1025-5842. DOI: `10.1080/10255840903208189`.

[89]   M. Langelaar, « Topology optimization of 3D self-supporting structures for additive manufacturing », *Additive Manufacturing*, vol. 12, pp. 60–70, Oct. 2016, ISSN: 2214-8604. DOI: `10.1016/j.addma.2016.06.010`.

REFERENCES

[90] Z. Xiao, Y. Yang, R. Xiao, Y. Bai, C. Song, and D. Wang, « Evaluation of topology-optimized lattice structures manufactured via selective laser melting », *Materials & Design*, vol. 143, pp. 27–37, Apr. 2018, ISSN: 0264-1275. DOI: `10.1016/j.matdes.2018.01.023`.

[91] A. Sutradhar, G. H. Paulino, M. J. Miller, and T. H. Nguyen, « Topological optimization for designing patient-specific large craniofacial segmental bone replacements », *Proceedings of the National Academy of Sciences*, vol. 107, no. 30, pp. 13 222–13 227, Jul. 2010, ISSN: 0027-8424, 1091-6490. DOI: `10.1073/pnas.1001208107`.

[92] D.-m. Xiao, Y.-q. Yang, X.-b. Su, D. Wang, and Z.-y. Luo, « Topology optimization of microstructure and selective laser melting fabrication for metallic biomaterial scaffolds », *Transactions of Nonferrous Metals Society of China*, vol. 22, no. 10, pp. 2554–2561, Oct. 2012, ISSN: 1003-6326. DOI: `10.1016/S1003-6326(11)61500-8`.

[93] H. d. A. Almeida and P. J. da Silva Bártolo, « Virtual topological optimisation of scaffolds for rapid prototyping », *Medical Engineering & Physics*, vol. 32, no. 7, pp. 775–782, Sep. 2010, ISSN: 1350-4533. DOI: `10.1016/j.medengphy.2010.05.001`.

[94] M. R. Dias, J. M. Guedes, C. L. Flanagan, S. J. Hollister, and P. R. Fernandes, « Optimization of scaffold design for bone tissue engineering: A computational and experimental study », *Medical Engineering & Physics*, vol. 36, no. 4, pp. 448–457, Apr. 2014, ISSN: 1350-4533. DOI: `10.1016/j.medengphy.2014.02.010`.

[95] J. K. Guest and J. H. Prévost, « Optimizing multifunctional materials: Design of microstructures for maximized stiffness and fluid permeability », *International Journal of Solids and Structures*, vol. 43, no. 22, pp. 7028–7047, Nov. 2006, ISSN: 0020-7683. DOI: `10.1016/j.ijsolstr.2006.03.001`.

[96] V. J. Challis, A. P. Roberts, J. F. Grotowski, L.-C. Zhang, and T. B. Sercombe, « Prototypes for Bone Implant Scaffolds Designed via Topology Optimization and Manufactured by Solid Freeform Fabrication », *Advanced Engineering Materials*, vol. 12, no. 11, pp. 1106–1110, Nov. 2010, ISSN: 1527-2648. DOI: `10.1002/adem.201000154`.

[97] H. Kang, C.-Y. Lin, and S. J. Hollister, « Topology optimization of three dimensional tissue engineering scaffold architectures for prescribed bulk modulus and diffusivity », *Structural and Multidisciplinary Optimization*, vol. 42, no. 4, pp. 633–644, Oct. 2010, ISSN: 1615-1488. DOI: `10.1007/s00158-010-0508-8`.

[98] Y. Chen, V. Bloemen, S. Impens, M. Moesen, F. P. Luyten, and J. Schrooten, « Characterization and Optimization of Cell Seeding in Scaffolds by Factorial Design: Quality by Design Approach for Skeletal Tissue Engineering », *Tissue Engineering Part C: Methods*, vol. 17, no. 12, pp. 1211–1221, Sep. 2011, ISSN: 1937-3384. DOI: `10.1089/ten.tec.2011.0092`.

[99] S. Sturm, S. Zhou, Y.-W. Mai, and Q. Li, « On stiffness of scaffolds for bone tissue engineering - a numerical study », *Journal of Biomechanics*, vol. 43, no. 9, pp. 1738–1744, Jun. 2010, ISSN: 1873-2380. DOI: `10.1016/j.jbiomech.2010.02.020`.

[100] P. Makowski and W. Kuś, « Optimization of bone scaffold structures using experimental and numerical data », *Acta Mechanica*, vol. 227, no. 1, pp. 139–149, Jan. 2016, ISSN: 1619-6937. DOI: `10.1007/s00707-015-1421-4`.

[101] S. J. Hollister and C. Y. Lin, « Computational design of tissue engineering scaffolds », *Computer Methods in Applied Mechanics and Engineering*, Computational Bioengineering, vol. 196, no. 31, pp. 2991–2998, Jun. 2007, ISSN: 0045-7825. DOI: `10.1016/j.cma.2006.09.023`.

[102] C.-C. Chang, Y. Chen, S. Zhou, Y.-W. Mai, and Q. Li, « Computational Design for Scaffold Tissue Engineering », in *Biomaterials for Implants and Scaffolds*, Q. Li and Y. W. Mai, Eds., vol. 8, Berlin: Springer-Verlag Berlin, 2017, pp. 349–369, ISBN: 978-3-662-53574-5.

[103] C. Y. Lin, N. Kikuchi, and S. J. Hollister, « A novel method for biomaterial scaffold internal architecture design to match bone elastic properties with desired porosity », *Journal of Biomechanics*, vol. 37, no. 5, pp. 623–636, May 2004, ISSN: 0021-9290. DOI: `10.1016/j.jbiomech.2003.09.029`.

[104] A. Boccaccio, M. Fiorentino, A. E. Uva, L. N. Laghetti, and G. Monno, « Rhombicuboctahedron unit cell based scaffolds for bone regeneration: geometry optimization with a mechanobiology - driven algorithm », *Materials Science & Engineering C-Materials for Biological Applications*, vol. 83, pp. 51–66, Feb. 2018, ISSN: 0928-4931. DOI: `10.1016/j.msec.2017.09.004`.

[105] G. Percoco, A. E. Uva, M. Fiorentino, M. Gattullo, V. M. Manghisi, and A. Boccaccio, « Mechanobiological Approach to Design and Optimize Bone Tissue Scaffolds 3D Printed with Fused Deposition Modeling: A Feasibility Study », *Materials*, vol. 13, no. 3, p. 648, Jan. 2020. DOI: `10.3390/ma13030648`.

[106] D. J. Kelly and P. J. Prendergast, « Prediction of the Optimal Mechanical Properties for a Scaffold Used in Osteochondral Defect Repair », *Tissue Engineering*, vol. 12, no. 9, pp. 2509–2519, Sep. 2006, ISSN: 1076-3279. DOI: `10.1089/ten.2006.12.2509`.

[107] Y.-G. Koh, J.-A. Lee, Y. S. Kim, H. Y. Lee, H. J. Kim, and K.-T. Kang, « Optimal mechanical properties of a scaffold for cartilage regeneration using finite element analysis », *Journal of Tissue Engineering*, vol. 10, p. 2 041 731 419 832 133, Jan. 2019, ISSN: 2041-7314. DOI: `10.1177/2041731419832133`.

[108] P. S. P. Poh, D. Valainis, K. Bhattacharya, M. van Griensven, and P. Dondl, « Optimization of Bone Scaffold Porosity Distributions », *Scientific Reports*, vol. 9, no. 1, p. 9170, Jun. 2019, ISSN: 2045-2322. DOI: `10.1038/s41598-019-44872-2`.

[109] C. Wu, J. Fang, A. Entezari, G. Sun, M. V Swain, Y. Xu, G. P. Steven, and Q. Li, « A time-dependent mechanobiology-based topology optimization to enhance bone growth in tissue scaffolds », *Journal of Biomechanics*, p. 110 233, Jan. 2021, ISSN: 0021-9290. DOI: `10.1016/j.jbiomech.2021.110233`.

REFERENCES

[110] G. N. Duda, K. Eckert-Hübner, R. Sokiranski, A. Kreutner, R. Miller, and L. Claes, « Analysis of inter-fragmentary movement as a function of musculoskeletal loading conditions in sheep », *Journal of Biomechanics*, vol. 31, no. 3, pp. 201–210, Dec. 1997, ISSN: 0021-9290. DOI: 10.1016/S0021-9290(97)00127-9.

[111] International Organization for Standardization, *International Standard ISO/IEC 14882:2020(E) – Programming Language C++*, https://isocpp.org/std/the-standard, 2020.

[112] H. Isaksson, C. C. van Donkelaar, R. Huiskes, and K. Ito, « A mechano-regulatory bone-healing model incorporating cell-phenotype specific activity », *Journal of Theoretical Biology*, vol. 252, no. 2, pp. 230–246, May 2008, ISSN: 0022-5193. DOI: 10.1016/j.jtbi.2008.01.030.

[113] P. A. Appeddu and B. D. Shur, « Molecular analysis of cell surface beta-1,4-galactosyltransferase function during cell migration », *Proceedings of the National Academy of Sciences*, vol. 91, no. 6, pp. 2095–2099, Mar. 1994, ISSN: 0027-8424, 1091-6490. DOI: 10.1073/pnas.91.6.2095.

[114] S. Postigo, H. Schmidt, A. Rohlmann, M. Putzier, A. Simón, G. Duda, and S. Checa, « Investigation of different cage designs and mechano-regulation algorithms in the lumbar interbody fusion process – A finite element analysis », *Journal of Biomechanics*, vol. 47, no. 6, pp. 1514–1519, Apr. 2014, ISSN: 0021-9290. DOI: 10.1016/j.jbiomech.2014.02.005.

[115] S. Aunoble, D. Clément, P. Frayssinet, M. F. Harmand, and J. C. L. Huec, « Biological performance of a new β-TCP/PLLA composite material for applications in spine surgery: In vitro and in vivo studies », *Journal of Biomedical Materials Research Part A*, vol. 78A, no. 2, pp. 416–422, 2006, ISSN: 1552-4965. DOI: 10.1002/jbm.a.30749.

[116] S. Haimi, N. Suuriniemi, A.-M. Haaparanta, V. Ellä, B. Lindroos, H. Huhtala, S. Räty, H. Kuokkanen, G. K. Sándor, M. Kellomäki, S. Miettinen, and R. Suuronen, « Growth and Osteogenic Differentiation of Adipose Stem Cells on PLA/Bioactive Glass and PLA/β-TCP Scaffolds », *Tissue Engineering Part A*, vol. 15, no. 7, pp. 1473–1480, Dec. 2008, ISSN: 1937-3341. DOI: 10.1089/ten.tea.2008.0241.

[117] S. Nakamura, T. Matsumoto, J.-I. Sasaki, H. Egusa, K. Y. Lee, T. Nakano, T. Sohmura, and A. Nakahira, « Effect of Calcium Ion Concentrations on Osteogenic Differentiation and Hematopoietic Stem Cell Niche-Related Protein Expression in Osteoblasts », *Tissue Engineering Part A*, vol. 16, no. 8, pp. 2467–2473, Mar. 2010, ISSN: 1937-3341. DOI: 10.1089/ten.tea.2009.0337.

[118] Y. Li, T. Jiang, L. Zheng, and J. Zhao, « Osteogenic differentiation of mesenchymal stem cells (MSCs) induced by three calcium phosphate ceramic (CaP) powders: A comparative study », *Materials Science and Engineering: C*, vol. 80, pp. 296–300, Nov. 2017, ISSN: 0928-4931. DOI: 10.1016/j.msec.2017.05.145.

[119] C. Perier-Metz, G. N. Duda, and S. Checa, « Mechano-Biological Computer Model of Scaffold-Supported Bone Regeneration: Effect of Bone Graft and Scaffold Structure on Large Bone Defect Tissue Patterning », *Frontiers in Bioengineering and Biotechnology*, vol. 8, 2020, ISSN: 2296-4185. DOI: 10.3389/fbioe.2020.585799.

[120] J. D. Hunter, « Matplotlib: A 2D Graphics Environment », *Computing in Science Engineering*, vol. 9, no. 3, pp. 90–95, May 2007, ISSN: 1558-366X. DOI: 10.1109/MCSE.2007.55.

[121] J. T. Bushberg, Ed., *The Essential Physics of Medical Imaging*, 3. ed., international ed. Philadelphia: Wolters Kluwer Health/Lippincott Williams & Wilkins, 2012, ISBN: 978-1-4511-1810-0.

[122] M. Abramoff, P. Magalhães, and S. Ram, « Image Processing with ImageJ », *Biophotonics International*, vol. 11, pp. 36–42, Nov. 2003.

[123] R. S. Rao, C. G. Kumar, R. S. Prakasham, and P. J. Hobbs, « The Taguchi methodology as a statistical tool for biotechnological applications: A critical appraisal », *Biotechnology Journal*, vol. 3, no. 4, pp. 510–523, Apr. 2008, ISSN: 18606768, 18607314. DOI: 10.1002/biot.200700201.

[124] T. Simpson, L. Dennis, and W. Chen, « Sampling Strategies for Computer Experiments: Design and Analysis », *International Journal of Reliability and Application*, vol. 2, pp. 209–240, 2002.

[125] H. B. Nielsen, S. N. Lophaven, and J. Søndergaard, *DACE - A Matlab Kriging Toolbox*, Informatics and Mathematical Modelling, Technical University of Denmark, DTU, Richard Petersens Plads, Building 321, DK-2800 Kgs. Lyngby, 2002.

[126] A. Chirokov, *Scattered Data Interpolation and Approximation using Radial Base Functions*, MATLAB Central File Exchange, 2006.

[127] G. Jekabsons, *ARESLab: Adaptive Regression Splines toolbox for Matlab/Octave*, 2016.

[128] T. W. Simpson, T. M. Mauery, J. J. Korte, and F. Mistree, « Kriging Models for Global Approximation in Simulation-Based Multidisciplinary Design Optimization », *AIAA Journal*, vol. 39, no. 12, pp. 2233–2241, Dec. 2001, ISSN: 0001-1452. DOI: 10.2514/2.1234.

[129] B. Rahmani, C. Perier-Metz, and S. Checa, « An optimization framework for the design of scaffolds towards enhanced bone regeneration », May 2020.

[130] I. The MathWorks, *Global Optimization Toolbox Manual*. Natick, Massachusetts, United States, 2020.

[131] G. Nasello, A. Vautrin, J. Pitocchi, M. Wesseling, J. H. Kuiper, M. Á. Pérez, and J. M. García-Aznar, « Mechano-driven regeneration predicts response variations in large animal model based on scaffold implantation site and individual mechano-sensitivity », *Bone*, p. 115 769, Dec. 2020, ISSN: 8756-3282. DOI: 10.1016/j.bone.2020.115769.

REFERENCES

[132] S. Baba, T. Inoue, Y. Hashimoto, D. Kimura, M. Ueda, K. Sakai, N. Matsumoto, C. Hiwa, T. Adachi, and M. Hojo, « Effectiveness of scaffolds with pre-seeded mesenchymal stem cells in bone regeneration –Assessment of osteogenic ability of scaffolds implanted under the periosteum of the cranial bone of rats– », *Dental Materials Journal*, vol. advpub, pp. 1 011 170 088–1 011 170 088, 2010. DOI: 10.4012/dmj.2009-123.

[133] A. B. González-Gil, J. M. Lamo-Espinosa, E. Muiños-López, P. Ripalda-Cemboráin, G. Abizanda, J. Valdés-Fernández, T. López-Martínez, M. Flandes-Iparraguirre, I. Andreu, M. R. Elizalde, K. Stuckensen, J. Groll, E. M. De-Juan-Pardo, F. Prósper, and F. Granero-Moltó, « Periosteum-derived mesenchymal progenitor cells in engineered implants promote fracture healing in a critical-size defect rat model », *Journal of Tissue Engineering and Regenerative Medicine*, vol. 0, no. 0, Feb. 2019, ISSN: 1932-6254. DOI: 10.1002/term.2821.

[134] D. P. Burke and D. J. Kelly, « Substrate Stiffness and Oxygen as Regulators of Stem Cell Differentiation during Skeletal Tissue Regeneration: A Mechanobiological Model », *PLOS ONE*, vol. 7, no. 7, e40737, Jul. 2012, ISSN: 1932-6203. DOI: 10.1371/journal.pone.0040737.

[135] P. B. F. Soares, C. C. G. Moura, C. R. Chinaglia, E. D. Zanotto, D. Zanetta-Barbosa, and A. Stavropoulos, « Effect of titanium surface functionalization with bioactive glass on osseointegration: An experimental study in dogs », *Clinical Oral Implants Research*, vol. 29, no. 11, pp. 1120–1125, 2018, ISSN: 1600-0501. DOI: 10.1111/clr.13375.

[136] E. P. Su, D. F. Justin, C. R. Pratt, V. K. Sarin, V. S. Nguyen, S. Oh, and S. Jin, « Effects of titanium nanotubes on the osseointegration, cell differentiation, mineralisation and antibacterial properties of orthopaedic implant surfaces », *The Bone & Joint Journal*, vol. 100-B, no. 1_Supple_A, pp. 9–16, Jan. 2018, ISSN: 2049-4394. DOI: 10.1302/0301-620X.100B1.BJJ-2017-0551.R1.

[137] B. E. Pippenger, M. Rottmar, B. S. Kopf, S. Stübinger, F. H. D. Torre, S. Berner, and K. Maniura-Weber, « Surface modification of ultrafine-grained titanium: Influence on mechanical properties, cytocompatibility, and osseointegration potential », *Clinical Oral Implants Research*, vol. 30, no. 1, pp. 99–110, 2019, ISSN: 1600-0501. DOI: 10.1111/clr.13396.

[138] C.-M. Lo, H.-B. Wang, M. Dembo, and Y.-l. Wang, « Cell Movement Is Guided by the Rigidity of the Substrate », *Biophysical Journal*, vol. 79, no. 1, pp. 144–152, Jul. 2000, ISSN: 0006-3495. DOI: 10.1016/S0006-3495(00)76279-5.

[139] N. Von Offenberg Sweeney, P. M. Cummins, E. J. Cotter, P. A. Fitzpatrick, Y. A. Birney, E. M. Redmond, and P. A. Cahill, « Cyclic strain-mediated regulation of vascular endothelial cell migration and tube formation », *Biochemical and Biophysical Research Communications*, vol. 329, no. 2, pp. 573–582, Apr. 2005, ISSN: 0006-291X. DOI: 10.1016/j.bbrc.2005.02.013.

[140]   M. Dietrich, H. Le Roy, D. B. Brückner, H. Engelke, R. Zantl, J. O. Rädler, and C. P. Broedersz, « Guiding 3D cell migration in deformed synthetic hydrogel microstructures », *Soft Matter*, vol. 14, no. 15, pp. 2816–2826, 2018, ISSN: 1744-683X, 1744-6848. DOI: 10.1039/C8SM00018B.

[141]   J. A. Hannafin, E. A. Attia, R. Henshaw, R. F. Warren, and M. M. Bhargava, « Effect of cyclic strain and plating matrix on cell proliferation and integrin expression by ligament fibroblasts », *Journal of Orthopaedic Research*, vol. 24, no. 2, pp. 149–158, 2006, ISSN: 1554-527X. DOI: 10.1002/jor.20018.

[142]   S. Saha, L. Ji, J. J. de Pablo, and S. P. Palecek, « Inhibition of human embryonic stem cell differentiation by mechanical strain », *Journal of Cellular Physiology*, vol. 206, no. 1, pp. 126–137, Jan. 2006, ISSN: 0021-9541. DOI: 10.1002/jcp.20441.

[143]   P. Moreo, J. M. García-Aznar, and M. Doblaré, « Modeling mechanosensing and its effect on the migration and proliferation of adherent cells », *Acta Biomaterialia*, vol. 4, no. 3, pp. 613–621, May 2008, ISSN: 1742-7061. DOI: 10.1016/j.actbio.2007.10.014.

[144]   C. Perier-Metz, G. N. Duda, and S. Checa, « Initial mechanical conditions within an optimized bone scaffold do not ensure bone regeneration – an in silico analysis », *Biomechanics and Modeling in Mechanobiology*, Jun. 2021, ISSN: 1617-7940. DOI: 10.1007/s10237-021-01472-2.

[145]   M. De Wild, C. Ghayor, S. Zimmermann, J. Rüegg, F. Nicholls, F. Schuler, T.-H. Chen, and F. E. Weber, « Osteoconductive Lattice Microarchitecture for Optimized Bone Regeneration », *3D Printing and Additive Manufacturing*, vol. 6, no. 1, pp. 40–49, Jun. 2018, ISSN: 2329-7662. DOI: 10.1089/3dp.2017.0129.

[146]   A.-M. Băbțan, D. Timuș, O. Sorițău, B. A. Boșca, R. Barabas, A. Ionel, N. B. Petrescu, C. N. Feurdean, I. R. Bordea, G. Saraci, Ş. C. Vesa, and A. Ilea, « Tissue Integration and Biological Cellular Response of SLM-Manufactured Titanium Scaffolds », *Metals*, vol. 10, no. 9, p. 1192, Sep. 2020. DOI: 10.3390/met10091192.

[147]   Y. Zheng, Q. Han, J. Wang, D. Li, Z. Song, and J. Yu, « Promotion of Osseointegration between Implant and Bone Interface by Titanium Alloy Porous Scaffolds Prepared by 3D Printing », *ACS Biomaterials Science & Engineering*, Jul. 2020. DOI: 10.1021/acsbiomaterials.0c00662.

[148]   A. Boccaccio, A. E. Uva, M. Fiorentino, V. Bevilacqua, C. Pappalettere, and G. Monno, « A Computational Approach to the Design of Scaffolds for Bone Tissue Engineering », in *Advances in Bionanomaterials, Bionam 2016*, S. Piotto, F. Rossi, S. Concilio, E. Reverchon, and G. Cattaneo, Eds., Berlin: Springer-Verlag Berlin, 2018, pp. 111–117, ISBN: 978-3-319-62027-5 978-3-319-62026-8.

[149]   R. Wu, Y. Li, M. Shen, X. Yang, L. Zhang, X. Ke, G. Yang, C. Gao, Z. Gou, and S. Xu, « Bone tissue regeneration: The role of finely tuned pore architecture of bioactive scaffolds before clinical translation », *Bioactive Materials*, vol. 6, no. 5, pp. 1242–1254, May 2021, ISSN: 2452-199X. DOI: 10.1016/j.bioactmat.2020.11.003.

REFERENCES

[150] M. Li, G. Li, and S. Azarm, « A Kriging Metamodel Assisted Multi-Objective Genetic Algorithm for Design Optimization », *Journal of Mechanical Design*, vol. 130, no. 3, pp. 031401-031401–10, Feb. 2008, ISSN: 1050-0472. DOI: `10.1115/1.2829879`.

[151] J. P. C. Kleijnen, « Kriging metamodeling in simulation: A review », *European Journal of Operational Research*, vol. 192, no. 3, pp. 707–716, Feb. 2009, ISSN: 0377-2217. DOI: `10.1016/j.ejor.2007.10.013`.

[152] S. J. Hollister, « Porous scaffold design for tissue engineering », *Nature Materials*, vol. 4, no. 7, pp. 518–524, Jul. 2005, ISSN: 1476-4660. DOI: `10.1038/nmat1421`.

[153] M. Asadi-Eydivand, M. Solati-Hashjin, A. Fathi, M. Padashi, and N. A. Abu Osman, « Optimal design of a 3D-printed scaffold using intelligent evolutionary algorithms », *Applied Soft Computing*, vol. 39, pp. 36–47, Feb. 2016, ISSN: 1568-4946. DOI: `10.1016/j.asoc.2015.11.011`.

[154] M. D. Byrne, *How Many Times Should a Stochastic Model Be Run? An Approach Based on Confidence Intervals.*

[155] F. E. Ritter, M. J. Schoelles, K. S. Quigley, and L. C. Klein, « Determining the Number of Simulation Runs: Treating Simulations as Theories by Not Sampling Their Behavior », in *Human-in-the-Loop Simulations: Methods and Practice*, L. Rothrock and S. Narayanan, Eds., London: Springer, 2011, pp. 97–116, ISBN: 978-0-85729-883-6. DOI: `10.1007/978-0-85729-883-6_5`.

[156] E. Borgiani, C. Figge, B. Kruck, B. M. Willie, G. N. Duda, and S. Checa, « Age-Related Changes in the Mechanical Regulation of Bone Healing Are Explained by Altered Cellular Mechanoresponse », *Journal of Bone and Mineral Research: The Official Journal of the American Society for Bone and Mineral Research*, May 2019, ISSN: 1523-4681. DOI: `10.1002/jbmr.3801`.

A

Mechanobiological bone regeneration model evaluations

A.1   Influence of the implementation of stochastic processes on bone regeneration predictions

The *in silico* MBBR simulations included stochastic processes in the agent-based model (cellular activity implementation), as new cell positions for migration, and cells for proliferation, differentiation and apoptosis are picked in a random way. These processes therefore depend on the random seed defined at the beginning of the simulation. However, due to the time necessary to run only one such simulation, each simulation case could not be run several times as needed [154, 155]. Therefore, a few simulation cases were run with different random seeds to evaluate the confidence that can be given to the results obtained in all simulations in general.

Two specific models developed for the titanium scaffold simulations were run five times each, with the soft scaffold geometry (strut width 1.2 mm): (1) baseline (fracture healing model) and (2) surface-guided ECM deposition and graft osteoconductive properties (migration and proliferation enhanced only in graft presence in the scaffold pores). Resulting tissue distribution predictions over time and bone and cartilage quantification in the mid-sagittal plane after 24 weeks (Figure 2.4 a) were compared between the different simulation runs.

Quantification after 24 weeks showed very similar values between the different runs, with less than 5% relative difference for most of the bone quantification, although one "outlier" could be observed in the baseline simulation cases (run 4 in the medial ROI) (Figure A.1). In addition, the lateral, medial and central ROI quantified bone amounts from all baseline simulation runs were clearly distinct from all complemented model runs. For instance, the quantification in the lateral ROI varied from 65 to 69% for the baseline simulations and from 61 to 62% for the complemented model runs; 52-59% compared to 60-61% in the medial ROI; and more than 70% compared to 40-41% in the central ROI.

Furthermore, the pairs of most different runs for each simulation set-up were in very good qualitative agreement between each other, showing similar tissue distributions at the different time points of interest (4, 8, 12, 16, 20, 24 weeks) (Figure A.2). Healing dynamics and approximate bridging times were the same in all runs for each simulation set-up.

Based on these observations, one run for each simulation set-up was assumed to give enough confidence when comparing different simulation set-ups with each other and with experimental results (where relative variations between animals and the average went up to 50%) [13].
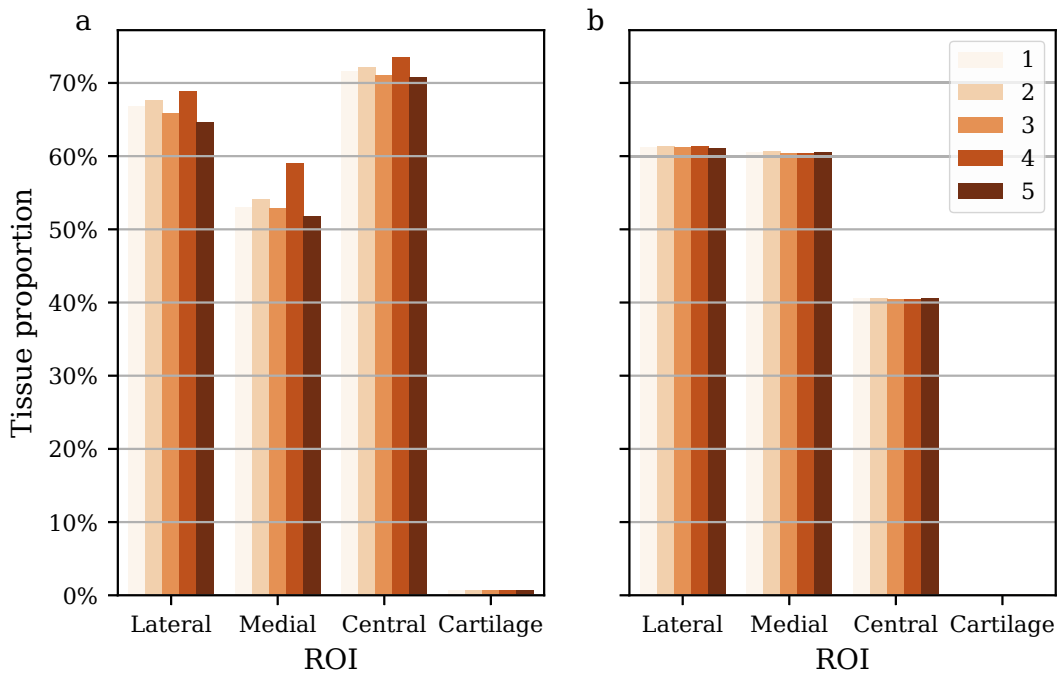
Figure A.1 – **Stochasticity evaluation** – **quantification**: bone proportion in the medial, lateral and central ROIs and cartilage proportion after 24 weeks for five runs of (a) the baseline model; (b) the model complemented with surface-guided ECM deposition and graft osteoconduction.
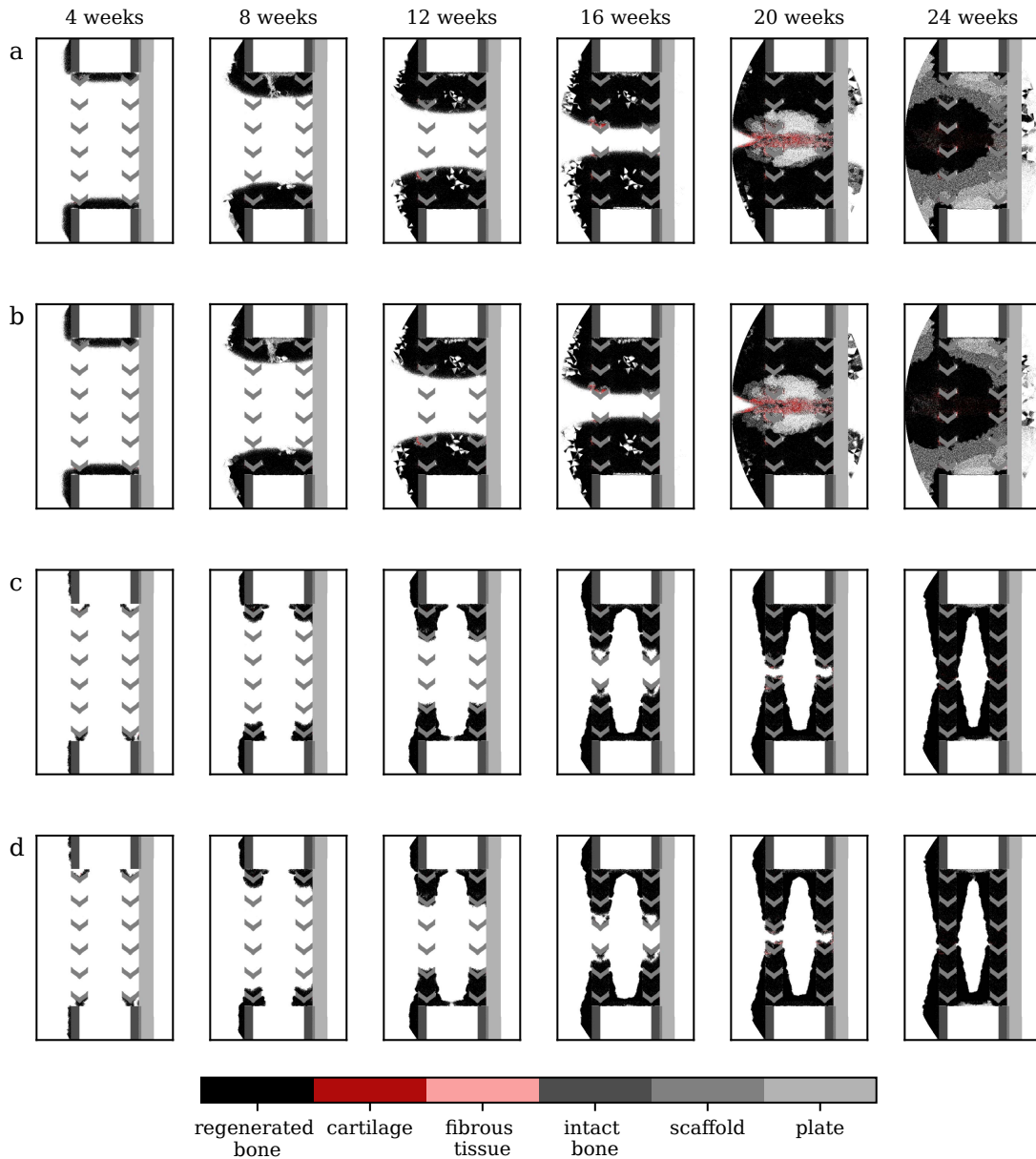
Figure A.2 – Stochasticity evaluation: histology pictures after 4, 8, 12, 16, 20 and 24 weeks in the mid-sagittal plane for run cases showing largest differences: (a) baseline model, run 4; (b) baseline model, run 5; (c) model complemented with surface-guided ECM deposition and graft osteoconduction, run 4; (d) model complemented with surface-guided ECM deposition and graft osteoconduction, run 5.

A.2 Mesh convergence analysis

A mesh convergence analysis of the callus and titanium soft scaffold was performed to evaluate which precision could be expected from the chosen mesh size. Characteristics of the tested meshes are given in Table A.1. The analysis was limited by the software capacity to mesh the complex geometries.

Case	Callus seed size range (mm)	Scaffold seed size range (mm)	Run time (s)	First principal strain (maximal)	Second principal strain	Third principal strain (minimal)
1	0.7-7	0.12-1.2	19'11"	5.60E-3	1.78E-3	-7.41E-3
2	0.2-2	0.07-0.7	38'51"	5.30E-3	1.48E-3	-6.80E-3
3	0.1-1	0.05-0.5	2h36'12"	3.93E-3	9.63E-4	-4.94E-3
4	0.03-1	0.04-0.4	3h17'34"	4.20E-3	1.46E-3	-5.72E-3

Table A.1 – **Scaffold-supported large bone defect mesh convergence analysis**: scaffold and callus mesh characteristics, corresponding simulation run times and averaged principal strain values in a set of highly strained elements (central pore on the lateral side, depicted on Figure A.3)

When comparing the initial strain prediction (right after scaffold implantation, i.e. with a callus filled with soft granulation tissue) between the 4 different cases, lower deformation was observed for the finer meshes (Figure A.3). This qualitative observation was further confirmed by the quantification of the principal strain values in a set of elements located in the central pore on the lateral side (Figure A.3 d), as the most strained regions of the callus showed up to 30% difference between the coarsest mesh (case 1) and the finest mesh (case 4) (Table A.1). However, most of the strain values were still within the bone-favouring range for all cases; those differences were therefore assumed to have no effect on the bone regeneration prediction and the coarsest mesh was used for the bone regeneration simulations. This allowed to stick to a reasonable FEA running time (20 minutes instead of more than 3 hours), what was crucial as the FEA had to be repeated several times for each regeneration simulation.
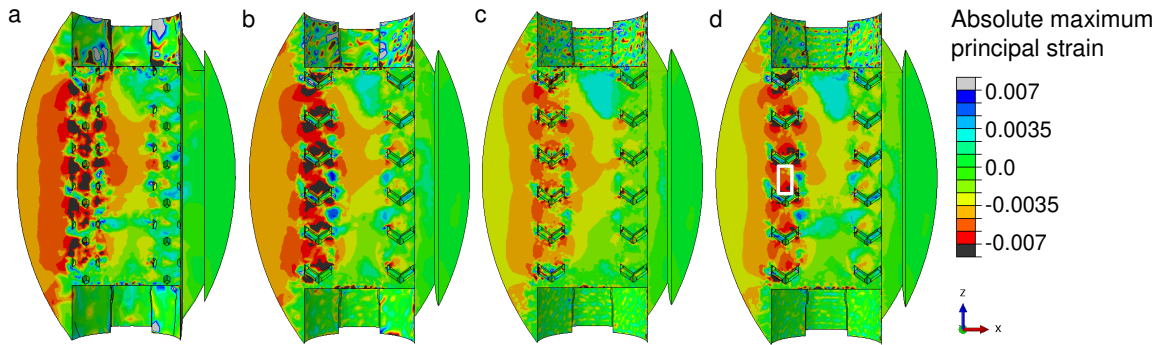
Figure A.3 – **Soft titanium scaffold and callus mesh convergence analysis**: initial absolute maximum principal strain distribution in the mid-sagittal plane with different mesh sizes: (a) case 1 (coarsest mesh); (b) case 2; (c) case 3; (d) case 4 (finest mesh). The white rectangle on (d) depicts the region where the principal strain values were averaged for a quantitative analysis.

A.3 FEA frequency analysis

To improve the overall bone regeneration simulation speed, the frequency of FEA runs was investigated. In previous works, a run at every iteration (one day) was usually performed [33]. However, the tissue deposition and maturation and subsequent material property changes are

known to be slow. Here, healing predictions with a reduced (one FEA every 3 iterations) and higher frequency (one FEA every iteration) were compared.

Figure A.4 shows the predictions of the baseline model and the model complemented with surface-guided ECM deposition and graft osteoconduction, respectively, both having a higher FEA frequency (every day); they can be compared with Figure A.2 (a,b for the baseline and c,d for the complemented model). Similar predictions were made in both cases for the complemented model. At 24 weeks post-surgery, bone quantification in the ROIs was similar: 61, 61 and 41% in the lateral, medial and central ROIs, respectively, for the model with a higher FEA frequency; compared to 60, 60 and 40% for the lower FEA frequency. The baseline model also showed similar bone regeneration patterning and dynamics until 20 weeks post-surgery; the 24-week time point was, however, much more depending on the FEA frequency, with a stronger remodelling prediction for the lower FEA frequency and stronger differences in the quantification: 60, 47 and 56% in the lateral, medial and central ROIs, respectively, compared to 67, 53 and 72% for the lower FEA frequency. This can be explained by the fact that bone resorption is sensitive to very small mechanical environment changes, thus making it necessary to have finer and more frequent FEA. However, because this remodelling did not happen *in vivo* and was one of the baseline model flaws, the lower FEA frequency (every 3 days) was considered to achieve reliable results. This resulted in overall simulation times nearly divided by 3 (as the FEA runs are the most time-consuming part of the simulation), i.e. 1 instead of 3 days.
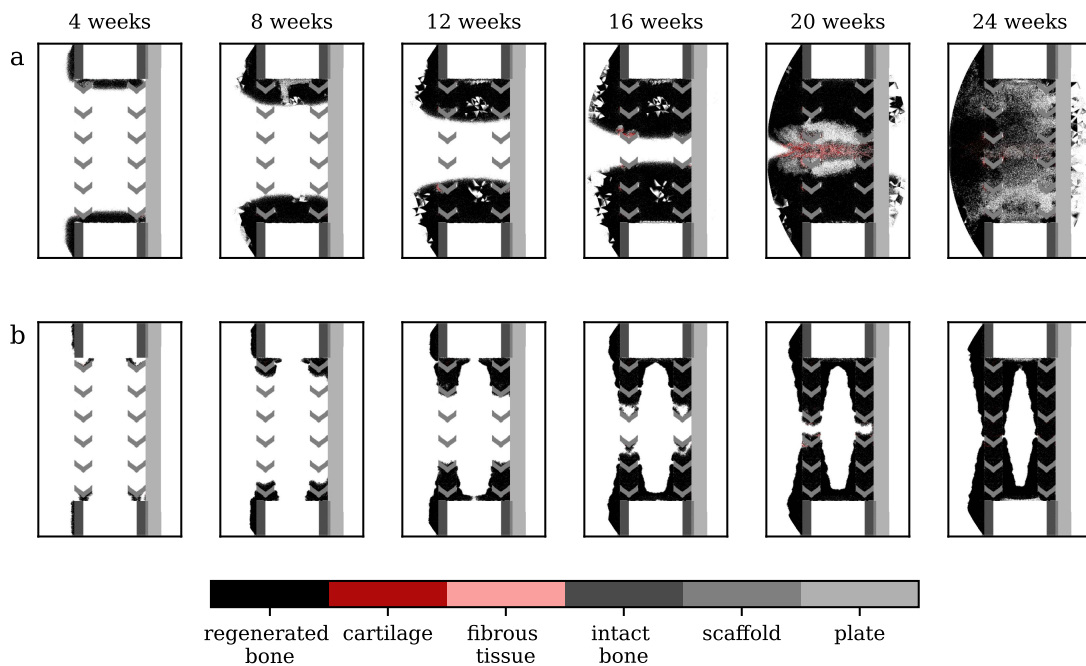
Figure A.4 − Bone regeneration model − FEA frequency evaluation: histology pictures after 4, 8, 12, 16, 20 and 24 weeks in the mid-sagittal plane for: (a) baseline model, FEA run every iteration; (b) model complemented with surface-guided ECM deposition and graft osteoconduction, FEA run every iteration.

A.4 Callus size effect on bone regeneration simulation

A further analysis was performed on the callus size implemented in the bone regeneration model. As the experimental data did not show any notable callus, the implemented callus was not directly related to biological data. It delimited the space in which the ABM cells could move, proliferate and deposit new tissues, but the focus was mostly set on the central part of the defect, between both intact bone extremities. The effect of the defined callus size on bone healing predictions in this region was therefore investigated by running a simulation with a twice wider callus (circle arcs of maximum width 20 mm instead of 10 mm at mid-height).

The size of the callus did not affect the predicted regeneration dynamics and only slightly affected the tissue patterning from 20 weeks post-surgery on (Figure A.5 compared to Figure A.2 a, b). As mentioned before, the different patterning here was due to the remodelling predictions of the model that were more sensitive to the mechanical environment.
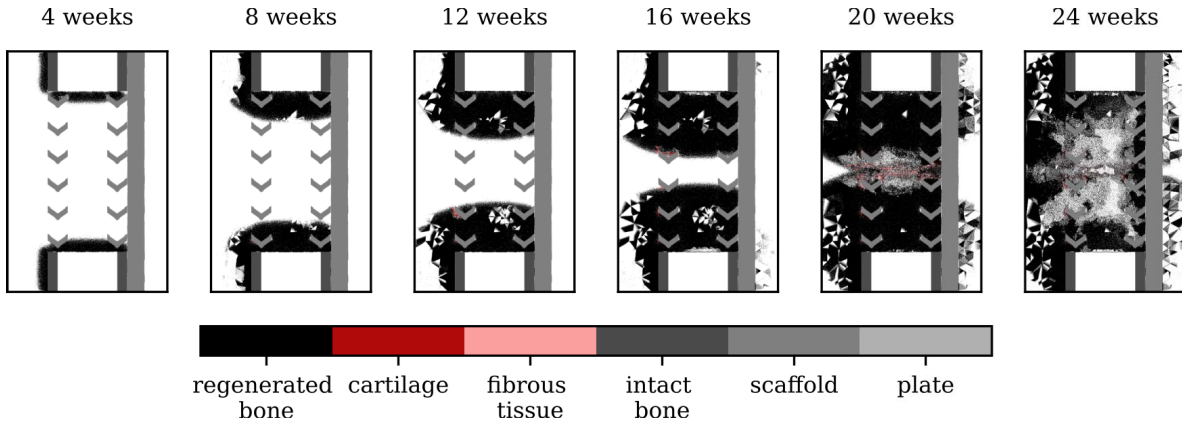
Figure A.5 – **Bone regeneration model – effect of the callus size definition**: histology pictures after 4, 8, 12, 16, 20 and 24 weeks in the mid-sagittal plane for the baseline model with a bigger callus.

A.5 ABM point size analysis

The effect of the ABM point size definition on the bone regeneration model predictions was investigated. In the past, smaller cubic points (of size 10 µm) have been used in similar computer models for bone regeneration [49, 156]. These smaller points are more appropriate to represent one unique cell [112]. However, because the studies of this thesis focused on large defects in a large animal (sheep), using such small matrix points would have resulted in very large matrices, leading to slow simulations and large memory requirements.

To assess the validity of using cubic cell volumes with size 100-µm, the baseline model predictions (Figure A.2 a, b) were compared to the same simulation set-up predictions obtained with smaller points (50 µm) (Figure A.6). The comparison revealed a marked effect of the ABM point size on the regeneration predictions and especially on the healing dynamics: smaller points led to a slower healing process, due to a reduced effective migration speed. The 24-week time point of the smaller-point model corresponded to the 16-week time point of the bigger-point model. As the computer model (with bigger points) was predicting slower bone regeneration than observed *in vivo*, migration speed or other parameters might need to be

adapted to better reflect the experimental reality, but the model predictions were considered reliable to predict the regeneration process.
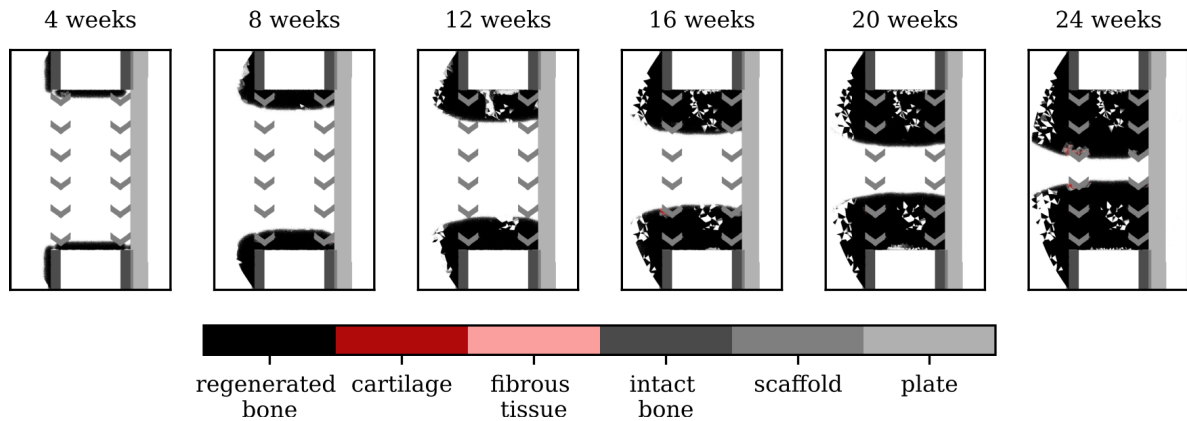
Figure A.6 – **Bone regeneration model – effect of the ABM point size definition**: histology pictures after 4, 8, 12, 16, 20 and 24 weeks in the mid-sagittal plane for the baseline model, with smaller matrix point size (50 µm).

A.6 Material pools for PCL scaffold simulations

As briefly described in Section 2.1.2.2, the PCL scaffold simulations used a material definition simplification based on 35 material pools defined in Table 2.2. For each FE, the average Young's modulus value obtained from the rule of mixtures was compared to the material pools' extrema and the element was attributed to the corresponding material pool. For each material pool, a solid section was then defined in the Abaqus input file containing all elements of the given pool; this solid section had the material pool mechanical properties (both Young's modulus and Poisson ratio) (Table 2.2). To evaluate the impact of this simplification on the simulation predictions, the following analyses were performed:

— the element pool sizes were evaluated at 3, 6 and 12 months post-surgery
— the average Young's modulus for each pool was derived from the detailed FE material properties and the error relative to the pool's implemented Young's modulus was computed at 3, 6 and 12 months post-surgery
— qualitative comparison between the material pools and full material description models was performed using the predicted µCT images
— bone volumes were quantified in the ROIs defined for the PCL scaffold set-up (Figure 2.4 b)

The analysis revealed non-homogeneous distribution throughout the material pools, some containing only a few hundreds elements and others tens of thousands (Figure A.7 a). However, Young's modulus errors in each material pool were in general lower than 5%; larger errors (ca. 10%) occurred only for the least populated pools, so with an expected low influence on the simulation predictions (Figure A.7 b).

When comparing baseline simulation predictions with a full material description or a material pool implementation, no marked differences were observed. µCT data showed very similar patterns 3 and 12 months post-surgery (Figure A.8). Moreover, the quantified bone volumes in the ROIs were similar in both simulation set-ups, with less than 2.5% relative error
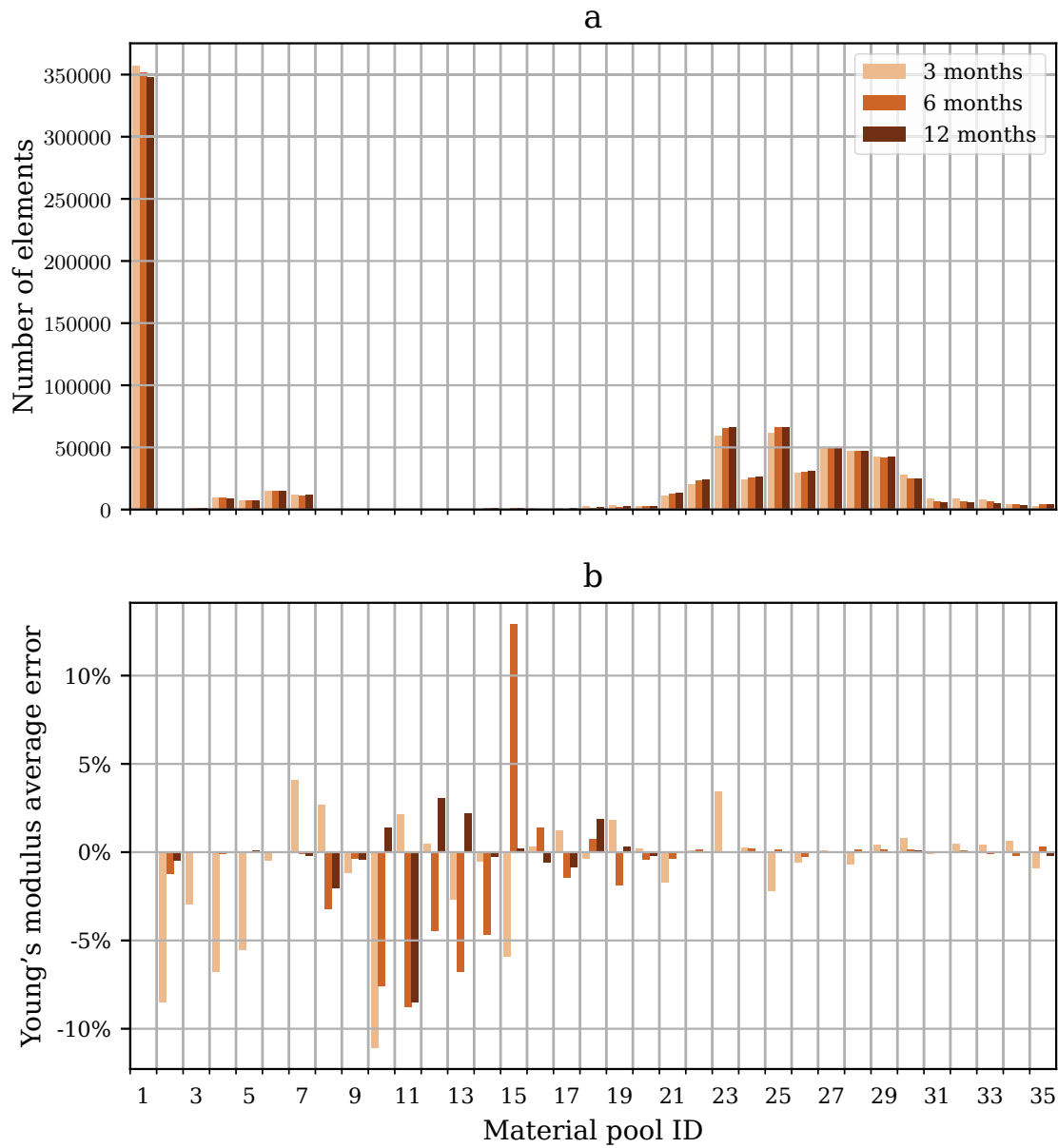
Figure A.7 – PCL scaffold material groups analysis: (a) number of finite elements in a given pool; (b) average relative error done on the FE Young's modulus due to the material pool implementation. Both graphs show data at 3, 6 and 12 months post-surgery.
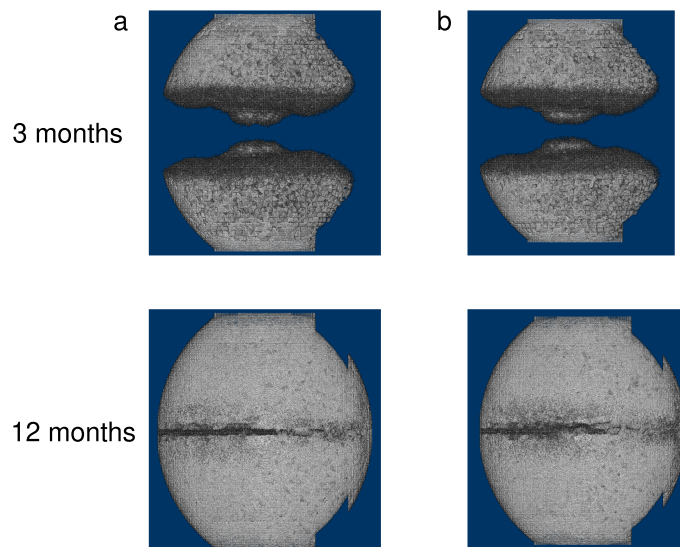
Figure A.8 – PCL scaffold material groups – µCT predictions: baseline predictions 3 and 12 months post-surgery for (a) the model implementing material pools; (b) the model implementing a full description of the callus FE material properties.

in all quantification data except for the inner duct 12 months post-surgery (18.4%) (Table A.2). The conclusions made using the material pool model were therefore considered reliable. This reduced the simulation time from 10.5 days to 0.7 day.

Time point	ROI	Full material description	Material pools
3 months	Total	5758	5885
3 months	Inner duct	757	760
3 months	Scaffold	1959	1966
12 months	Total	15819	15752
12 months	Inner duct	1615	1318
12 months	Scaffold	3344	3290

Table A.2 – PCL scaffold material groups – quantification: bone volumes are given in mm^3

B

Optimisation preliminary studies

B.1   Surrogate model evaluation

Different surrogate modelling techniques were assessed using two independent data-sets of graded cubic scaffolds (80 scaffold geometries for each, obtained with the Latin hypercube sampling technique). For each technique, a first model ("model A") was built using data-set A and tested on data-set B; and a second model ("model B") was built using data-set B and tested on data-set A. To assess the predictive capability of the surrogate model, the root mean square error (RMSE) of the predictions on the testing set was computed. The only surrogate modelling technique that achieved less than 5% error for both data-sets was Kriging, and MARS showed nearly as good results (slightly above 5%) (Figure B.1). All other modelling techniques led to errors ranging from 6 to 9% and were therefore not considered suitable for the surrogate optimisation framework.

B.2   Symmetric cylindrical scaffold half model evaluation

To reduce the optimisation computational time, the symmetry of the cylindrical scaffold set-up used for optimisation was exploited to simulate only half of it in the FEA and the ABM. To ensure the validity of this approach, one specific scaffold design defined by $x_1 = x_2 = x_3 = 2mm$ was studied: mechanics was evaluated in the post-implantation situation and bone regeneration was simulated according to the simulation set-up validated for the titanium scaffold. Initial strain distribution (considering the full callus as granulation tissue) were similar between full and half models (Figure B.2 a, b). In addition, the bone regeneration simulation led to a similar 24-week histology prediction (Figure B.2 c, d), that showed, however, a reduced amount of regenerated bone along the plate (more resorption stimulus) in the half model compared to the full one. These differences led to 80% regenerated bone in the scaffold pores for the half model compared to 90% for the full model; they were considered small enough to use the half model for the cylindrical scaffold optimisation studies.
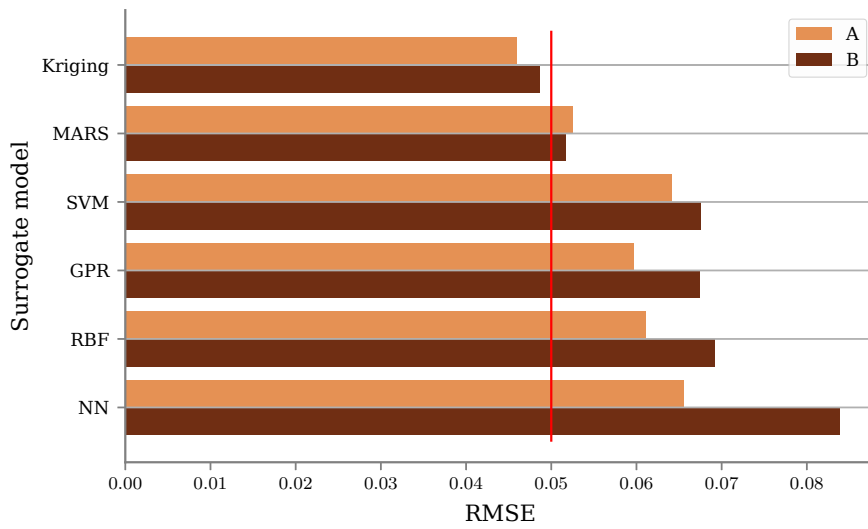
Figure B.1 – **Surrogate model evaluation**: RMSE obtained for models A and B using different surrogate modelling techniques; the red line depicts the 5%-error limit; MARS, SVM, GPR, RBF and NN denote multivariate adaptive regression splines, support vector machines, Gaussian process regression, radial basis functions and neural networks, respectively.
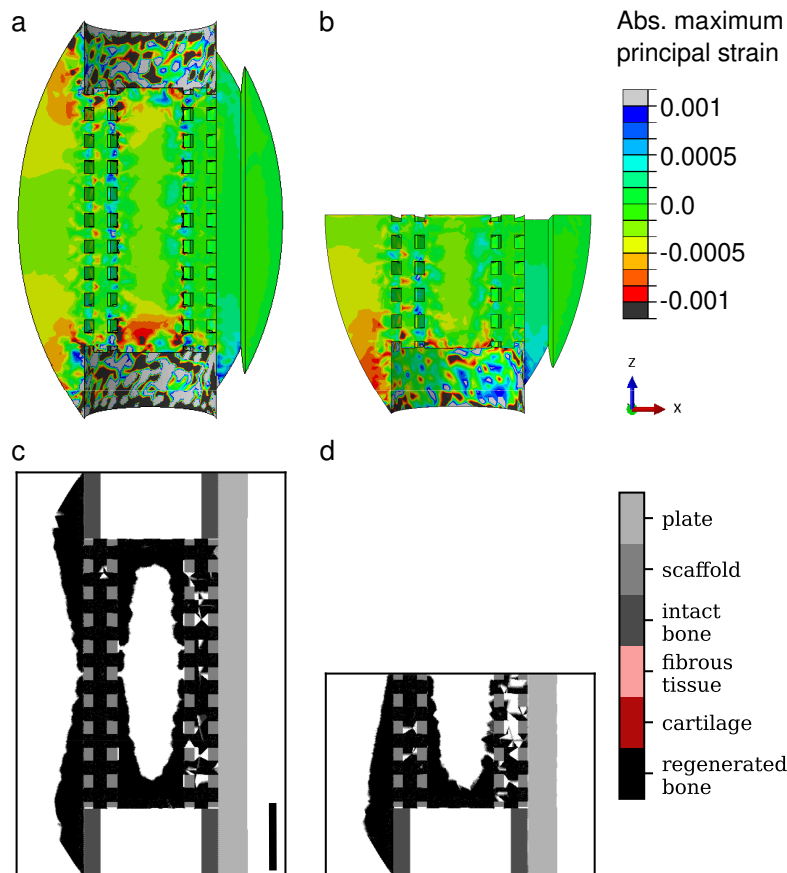
Figure B.2 – **Half model symmetry evaluation**: (a, b) post-implantation strain distribution in the callus mid-sagittal plane; (c, d) histology predictions in the mid-sagittal plane 24 weeks post-implantation for (a, c) full and (b, d) half models. Colour scales are described on the right. The scale bar represents 10 mm.

114